Graz University of Technology
Faculty of Civil Engineering
Institute of Hydraulic Engineering and Water Resources Management

Numerical Studies on Bulb Turbine Intakes

Tino KOSTIĆ

Vorgelegt zur Erlangung des
akademischen Grades eines Master
der Studienrichtung Bauingenieurwesen

Graz, in April 2016

Supervisor:

Univ.-Prof. Dipl.-Ing. Dr.techn. Gerald ZENZ

.....

Assistant:

Shervin Shahriari, M.Sc

.....

Eid (Ehrenwörtliche Erklärung)

Ich erkläre an Eides Statt, dass ich die vorliegende Arbeit selbstständig und ohne fremde Hilfe verfasst, andere als die angegebenen Quellen nicht benutzt und die den benutzten Quellen wörtlich und inhaltlich entnommenen Stellen als solche kenntlich gemacht habe.

Ich versichere, dass ich dieses Diplomarbeitsthema bisher weder im In- noch im Ausland (einer Beurteilerin oder einem Beurteiler) in irgendeiner Form als Prüfungsarbeit vorgelegt habe.

Graz, in April 2016 .....

Abstract

This master thesis is about performing numerical simulations of a series of hydraulic laboratory tests on bulb turbine intakes. These laboratory tests are presented in a paper entitled “Hydraulic Model Studies on Bulb Turbine Intakes” which was carried out by the U.S. Department of the Interior in 1983. The purpose of the study was to investigate possible simplifications in design of the intake flow passages for bulb turbines, and to determine head losses associated with these simplifications. Four intakes with different shapes were investigated in order to determine fluid flow behaviour in bulb turbine intake regions. Numerical simulations were conducted with the ANSYS CFX software, a commercial computational fluid dynamics (shorter CFD) software. The objective of this thesis is to compare and cross-validate results gained through the numerical analysis with the results from the original physical model study. It is of great interest to represent the velocity distribution and head losses for each intake individually. At first, the 3D geometries were created using Auto CAD 3D, afterwards the start of numerical modelling follow. Numerical modelling includes geometry establishment, grid generation, boundary condition assessment and solution of fluid flow equations. The grid generation process was performed using the ANSYS Meshing. In CFX–Pre, boundary conditions and fluid properties were selected in order to solve the system of partially differential equations with the CFX–Solver. In order to save computing time and memory a model simplification was introduced. Numerical model results show similar velocity distributions as laboratory results for all four intakes. It is also visible that intake 4, the shortest intake with the greatest opening curves on the top and sides continued with straight planes, has least head losses and a desirable velocity distribution.

Kurzfassung

Diese Masterarbeit beschäftigt sich mit dem Durchfuhren numerischer Simulationen einer Reihe von hydraulischen Laborversuchen über Einläufe von Rohrturbinen. Diese Laborversuche sind zusammengefaßt in der wissenschaftlichen Publikation „Hydraulic Model Studies on Bulb Turbine Intakes“ welche vom U.S. Department of the Interior im Jahre 1983 durchgeführt wurden. Der Zweck dieser Forschung war, mögliche Vereinfachungen in dem Einlaufbereich bei Rohrturbinen zu ermitteln und die dadurch verursachten lokalen Verluste zu bestimmen. Vier verschiedene Einlaufgeometrien wurden in diesen Laborversuchen geprüft. Numerische Simulationen wurden mit ANSYS CFX, einer kommerziellen Computational Fluid Dynamics (oder kürzer CFD) Software durchgeführt. Die Zielsetzung dieser Masterarbeit, ist numerische und physikalische Ergebnisse zu prüfen und miteinander zu vergleichen. Es ist von großem Interesse, die Geschwindigkeitsverteilungen und lokalen Verluste für jede Einlaufsgeometrie einzeln darzustellen. Erstmal wurden die Geometrien mit Hilfe von Auto CAD 3D erstellt, nachdem der Prozess der numerischen Modellierung begonnen werden konnte. Numerische Modellierung beinhaltet die Erstellung der Geometrie, Netzerstellung, Einfügung von Randbedingungen, und Lösung von den Strömungsgleichungen. Die Netzerstellung erfolgte durch Nutzung von ANSYS Meshing, Randbedingungen und Fluideigenschaften wurden in CFX-Pre gewählt und das System der differentiellen und partiellen Gleichungen wurde danach in CFX-Post gelöst. Um Rechenzeit und Speicherplatz zu sparen, wurde eine Modelvereinfachung eingeführt. Numerische Simulationen zeigen gleiche Ergebnisse wie die Laborversuche. Durch den Ergebnisvergleich ist es eindeutig, dass Einlauf 4, der kürzeste Einlauf mit dem größten Eingangskrümmungen, die geringste lokalen Verluste aufweist und vorzügliche Geschwindigkeitsverteilungen ergibt.

Table of Contents

1. Introduction

1.1 Introduction

This master's thesis is about performing numerical simulations of a series of hydraulic laboratory tests on bulb turbine intakes. These laboratory tests are presented in a paper entitled "Hydraulic Model Studies on Bulb Turbine Intakes" [1] which was carried out by the U.S. Department of the Interior in 1983. The purpose of the study was to investigate possible simplifications in design of the intake flow passages for bulb turbines, and to determine head losses associated with these simplifications. Four intakes with different shapes were investigated in order to determine fluid flow behaviour in bulb turbine intake regions. In this current study, geometries from the original model study will be used to generate numerical models. Furthermore, the physical and numerical results will be compared and cross-validated. Numerical simulations were conducted with the ANSYS CFX [7] software, a commercial computational fluid dynamics software.

1.2 Overview

For better understanding of the reasons behind the numerical modelling performed in this master's thesis, it is important to analyse the development of the original hydraulic laboratory model. Second chapter "The Physical Model Study", introduces these laboratory test. To comprehend the concept of numerical fluid flow modelling, it is necessary to review numerical methods and mathematical tools required for fluid flow simulations. Afterwards, fundamentals of the numerical method used in this thesis will be introduced. The fourth chapter provides the insight into numerical modelling including geometry establishment, grid generation, boundary condition assessment and solution to fluid flow equations. Numerical model geometry was developed through the use of AutoCAD 3D [8] with the goal of rebuilding the physical model's geometry. The rebuilt geometry was imported in the ANSYS Design Modeller [7], and the grid generation process was performed on the geometry using the ANSYS Meshing [7]. In CFX–Pre, boundary conditions and fluid properties were determined in order to solve the system of partially differential equations with the CFX–Solver.

In the fifth chapter, the results were presented and discussed. The final chapter provides the conclusions.

1.3 Objective

The objective of this research is to compare and cross-validate results obtained through the numerical analysis with the results from the original physical model study. It is of great interest to obtain the velocity distribution and head losses for each intake individually. The flow and velocity distributions obtained through validated results, can later be used to optimise the intake geometries of bulb turbines. It is also of interest to assume simplifications regarding the numerical modelling in order to save time, cost and ease the future investigations on similar topics.

An example of bulb turbine usage in run-of-river power plants is “Kraftwerk Melk” in Lower Austria. The figure below shoves a schematic representation of this power plant.

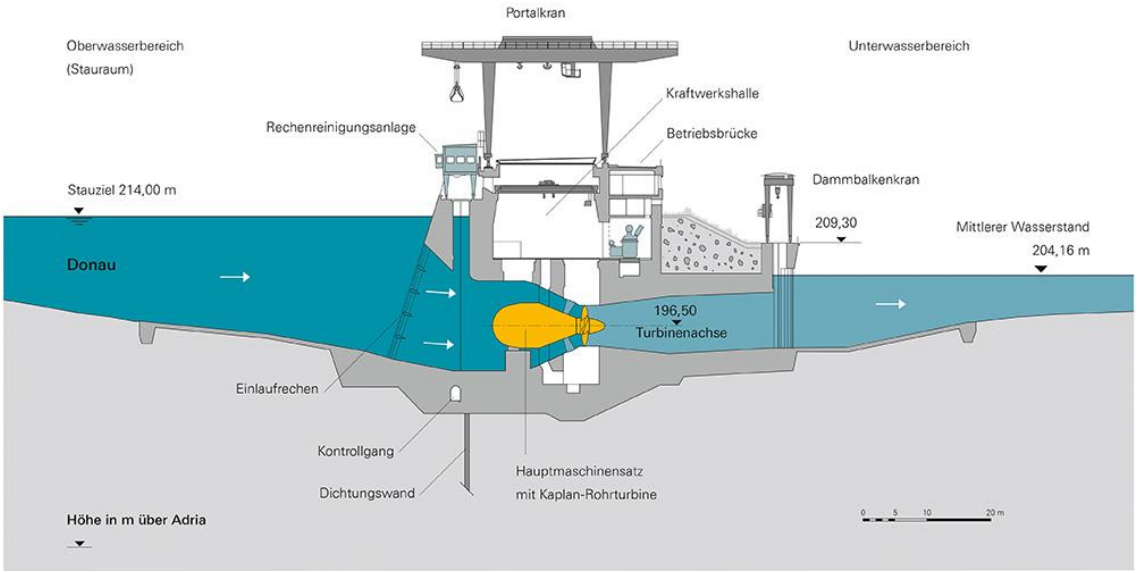

Figure 1: Example of bulb turbine usage; schematic representation of Power Plant Melk [9]

2. The Physical Model Study

2.1 Introduction

Hydraulic model study on bulb turbine intakes research was performed by the U.S. Department of the Interior, in Bureau of Reclamation's Engineering and Research Center's hydraulic laboratory in 1983. Figure below shows some images from the physical model paper: overall view of the test apparatus (left insert), draft tube and velocity measurements (right insert) and intake 1 with piezometer taps (middle insert). The Model itself, intake geometries, measured results and the study purpose will be shown later in this chapter.

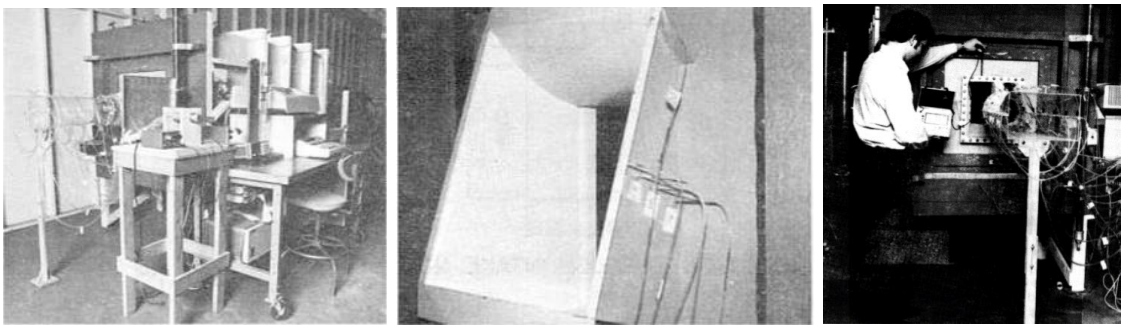

Figure 2: Physical model study from 1983 [1]

2.2 The Model

An air model was used in the original study. Air model can be used to study hydraulic problems in which the flow is governed by inertia and viscosity effects. The criterion of similarity for this type of flow is the well-known Reynolds Model Law (equation 2.1).

$$Reynold\ number = R = \frac{v \cdot D}{\nu} \tag{2.1}$$

Where:

v = velocity [m/s]

D = a characteristic length [m]

ν = kinematic viscosity [m^2/s]

Air models have several advantages over water models, such as:

- Flexible and easy model construction.
- Minor leakage problems.
- The ability to conduct rapid measurements.

Disadvantage of air modelling is that it required delicate measurement apparatus. Another disadvantage is the difficulty of transferring obtained model results to natural size prototype results. This is due to the fact that the kinematic viscosity for air is 10 to 20 times greater than the kinematic viscosity for water, meaning that the air model velocities need to be 10 to 20 times greater than the prototype water velocities in order to obtain the Reynolds Model Law similarity. In this hydraulic model study air velocity is limited to less than 50 m/s to avoid compressibility effects. Therefore, for obtaining the same Reynolds number for the same size model with water, velocity has to be between 2.5 m/s and 5 m/s. This velocity is acceptable, however, problems occur by downscaling air models in relation to real size water prototypes. For example, an air model reduced 5 times, demands model velocities 50 to 100 times greater than prototype velocities in order to obtain the Reynolds Model Law similarity. This, and the fact that the air velocity has to be limited to avoid compressibility effects, makes air models unsuitable for scaling the physical model test results to the prototype. However, the goal of the physical model test was not to analyze hydraulic models and similarity laws, but to compare different intake geometries and not to scale the air model results to real-size prototypes. This means that the use of air, instead of water in the physical model is justified, however, water is used as the fluid in the numerical analysis. Using water as the governing fluid in the numerical modelling makes future investigations regarding this topic easier and it simplifies scaling numerical results to real size prototypes results. In order to compare the velocities from physical model tests to numerical results, all the velocities were represented by the velocity coefficient (local velocity divided by mean velocity) for all intakes.

The test apparatus consist of an air supply pipe, including blower and orifice for discharge measurement, a stilling chamber and the intake models. Figure 3 shows the schematic diagram of the test apparatus.

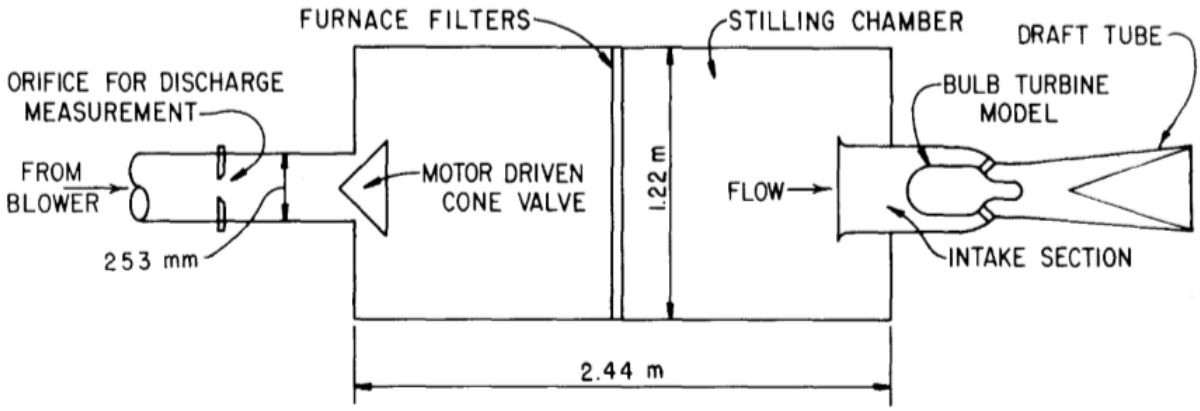

Figure 3: Schematic diagram of the test apparatus [1]

2.3 Purpose of the Study

The purpose for the original study was to reduce cost of low-head hydropower plants without introducing additional head losses.

Intakes for bulb and rim generator turbines are very large in relation to their runner diameters. Savings could be achieved by replacing curved surfaces with flat surfaces and by shortening intake lengths. Reducing the intake size would result in additional savings in trash racks, bulkheads, entrances, gates, and the associated operating equipment [6].

A desirable property of turbine intakes is that the velocities in the intake section should be evenly distributed throughout the whole intake surface. Irregular flow and flow separation in the intake section leads to uneven flow distribution on guide vanes and runner blades. Comparing the velocity distribution of the various intakes is also one of the purposes of the original study.

2.4 Intake Models

A model of a typical bulb turbine installation was built with using dimensions that correspond to standard flow passage dimensions used by a major manufacturer. [1]

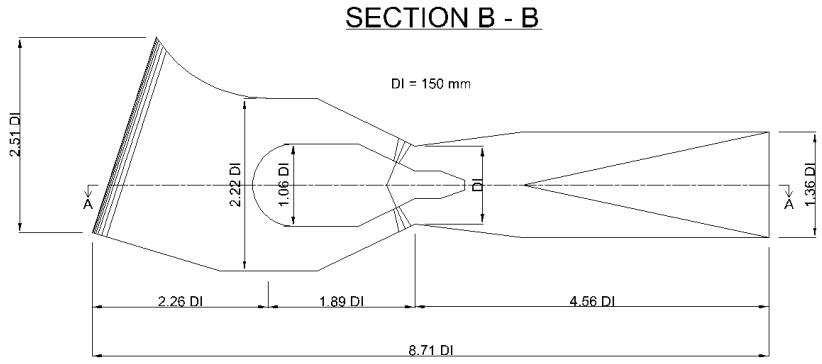

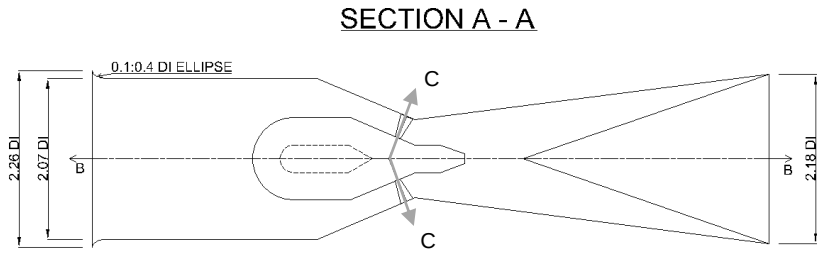

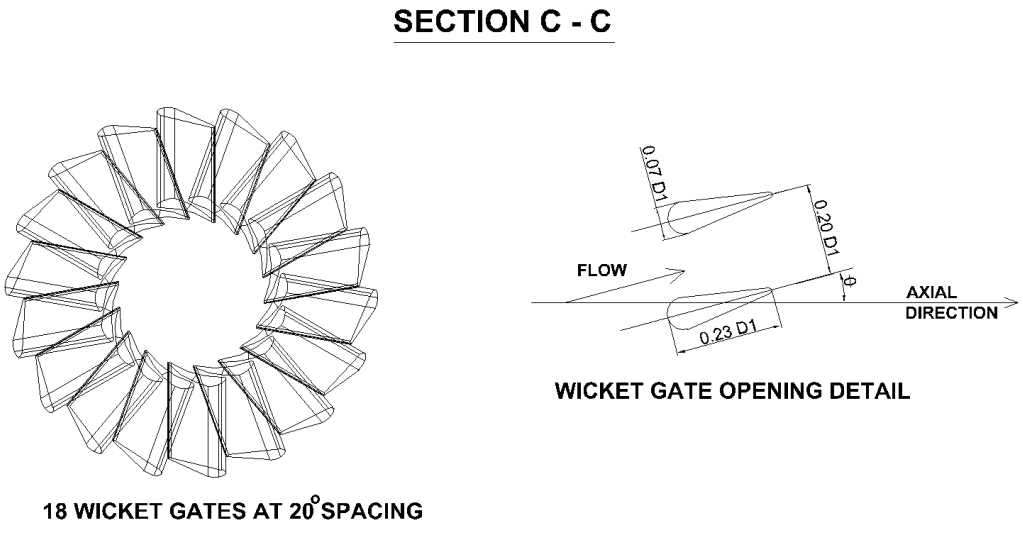

Figure 4: Bulb turbine geometry (with intake 1 shown)

All dimensions are given in terms of the runner diameter, D1. Figure 4 shows the bulb turbine flow passage with intake 1, where section A–A represent a horizontal, and section B–B a vertical cross-section.

The model contains four different intake sections (figures 5 – 8), the flow passage downstream from the intake section including the draft tube, bulb, piers supporting the bulb and the wicked gates. Runner blades were not included in the model because the focus of the study was the effect of changes on the intake flow passage geometry. The wicket gates opening angle θ was made adjustable from 0^0 to 60^0, with 0^0 being fully open.

Intake 1 (figure 5) is the traditional intake with a smooth bellmouth-type top curve. Intake 2 (figure 6) is slightly shorter than intake 1, and the top curve is replaced with two straight planes. Intake 3 (figure 7) has the simplest geometry shape, including only straight planes with no curvature. Intake 4 (figure 8) is the shortest intake, with an entrance curvature continued with straight planes.

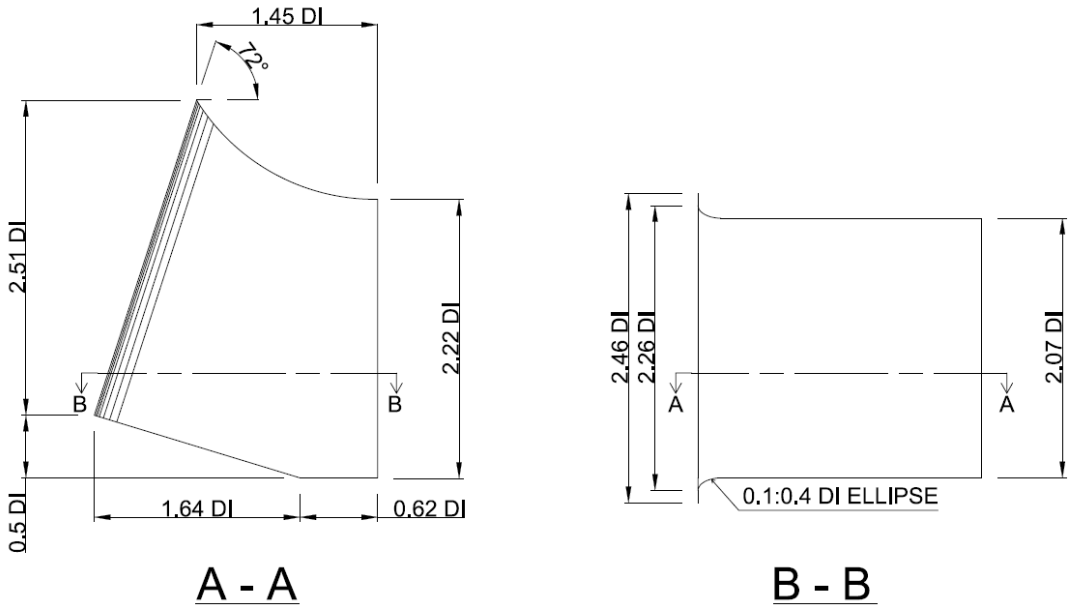

Figure 5: Geometry of intake 1

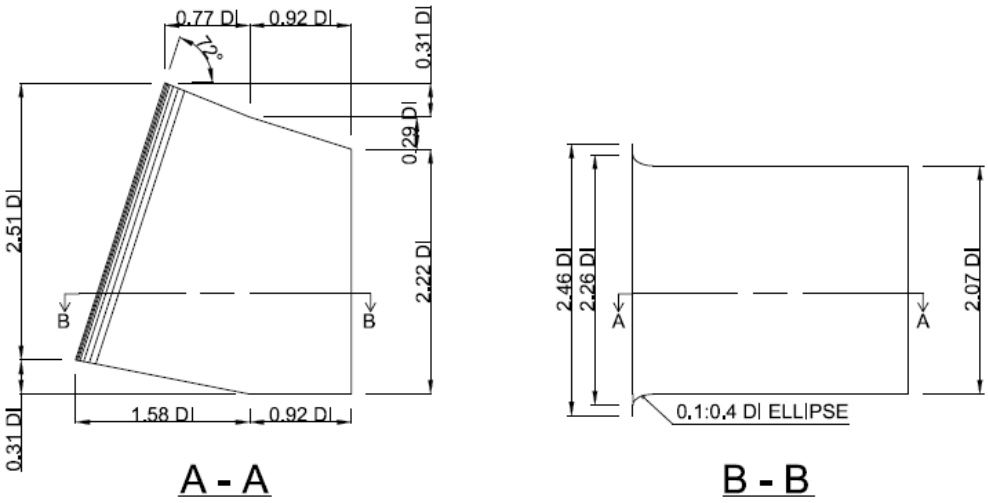

Figure 6: Geometry of intake 2

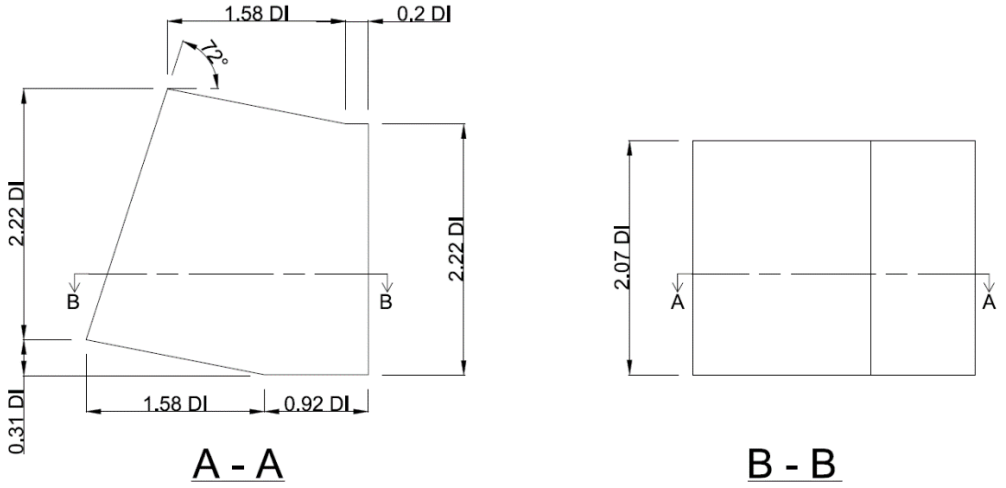

Figure 7: Geometry of intake 3

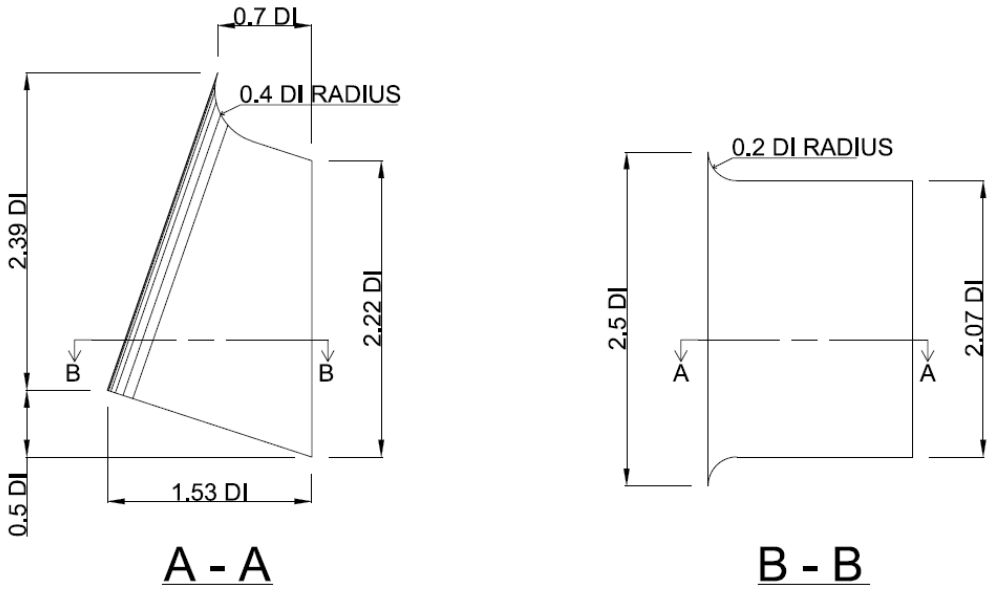

Figure 8: Geometry of intake 4

2.5 Results

The hydraulic mode study points out, that for wicket gate angles less than 45^0, the velocity distributions for a given intake design were very similar, and for 45^0 and 60^0 wicket gates angles, the profiles were very erratic and unsymmetrical. The study also points out that velocity distribution is very similar for different velocities.

Physical model results include velocity distributions and head losses measurement for each intake. Velocity measurements were conducted in a vertical plane upstream from the bulb (in figure 4 and 43).

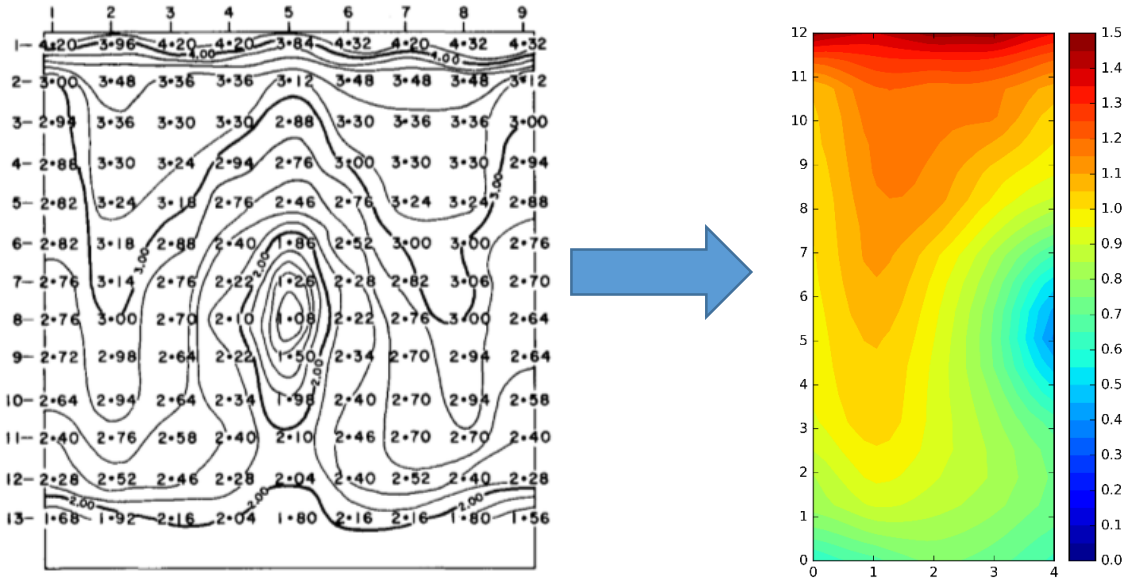

Figure 9: Representation of velocity measurement results for intake 1: original results represented with local velocities [m/s] (left) and modified results in PYTHON represented with the velocity coefficient [-] (right)

The representation of the measured velocity distribution for intake 1 is shown in figure 9 (left side). The original laboratory results were rearranged using the PYTHON programming language in order to make them look more similar to the numerical results from ANSYS CFX [7]. The measured velocities (figure 8, left) were divided by the mean velocity for each intake, so that all the velocities are represented by a velocity coefficient (local velocity divided with mean velocity) $v/\bar{v}$. Values between the measured velocities were interpolated. The results were imported into PYTHON from only one half of the velocity distribution diagram, because the results were estimated to be symmetrical. A colour scale

similar to the one used in ANSYS CFX [7] was imported into PYTHON. In figure 9 (right), the modified velocity results for intake 1 are shown.

In the physical model study, head losses were represented with the Euler number. The Euler number is a dimensionless ratio which relates inertia forces to pressure forces (equation 2.2).

$$Euler\ number = E = \frac{\rho \cdot v^2}{\Delta p} \tag{2.2}$$

Where:

ρ = fluid density [kg/m^3]

Δp = pressure drop [m]

v = velocity measured at the runners [m/s]

In incompressible fluids and in absence of other forces (such as viscosity and gravity), the Euler number is exclusively a function of the geometry of the flow boundaries. [1]

The Reynolds number in the laboratory test were about 10^4 to 10^5. At these Reynolds number, viscosity has little effect and the Euler number could be considered as a constant.

3. Introduction to Computational Fluid Dynamics

3.1 Introduction

Computational Fluid Dynamics (CFD) is a computer-based tool for simulating the behaviour of systems involving fluid flow, heat transfer, and other related physical processes. CFD operates by solving the equations of fluid flow (in a special form) over a region of interest, with specified (known) conditions on the boundary of that region. Commercial CFD packages (including ANSYS CFX) use highly developed user interfaces to input problem parameters and to obtain results. All CFD codes consist of three main elements: pre-processor, solver and post-processor.

3.1.1 Pre-processor

With the pre-processor operations the user is able to input flow and geometry problems to a CFD program. The operations at the pre-processing stage include:

- Geometry definition of the region of interest (the computational domain).
- Grid generation – the sub-division of the domain into a number of smaller, non-overlapping sub-domains.
- Selection of the physical phenomena that need to be modelled.
- Definition of fluid properties.
- Specification of appropriate boundary conditions at cells which coincide with or touch the domain boundary.

The input data are later subsequently transformed into a form suitable for use by the solver. The solution to a flow problem (velocity, pressure etc.) is defined at nodes inside each cell. In general, the larger the number of cells the better the solution accuracy. The accuracy of a solution and its cost in terms of necessary computer hardware and calculation time are both dependent on the fineness of the grid. Optional meshes are often non-uniform: finer in areas where larger

variations occur from point to point and coarser in regions with relatively little change (see chapter 4.2.3).

3.1.2 Solver

Numerical methods are used in CFD for solutions of fluid flow problems rather than analytical methods. Numerical analysis uses techniques that give approximate but accurate solutions of mathematical models. All numerical methods that form the basis of the solver perform the following steps:

- Approximations of the unknown flow variables by means of simple functions.
- Discretization by substitution of the approximations into the governing flow equations and subsequent mathematical manipulations.
- Solution of the algebraic equations.

There are several methods of discretization used in CFD such as: finite element method, spectral element method, finite difference method**,** finite volume method etc. Finite volume method (FVM) is a special type of the finite difference formulation. FVM has an advantage in memory usage and solution speed, especially for large problems, high Reynolds number and turbulent flows. In the finite volume method, the governing equations of fluid flow are expressed in a conservative form, and then solved over discrete control volumes. This discretization guarantees the conservation of fluxes through a particular control volume. The FVM is central to most of the main commercial available CFD codes (including CFX), hence this master thesis will be solely concerned with this discretization method.

3.1.3 Post-processor

With the post-processor the user is able to see the visualized results from the previous steps. These include:

- Domain, geometry and grid display.
- Vector plots.
- Streamline plots.
- Particle tracking.
- Plots of variables such as velocity, pressure etc.

For good understanding of the numerical solution algorithm, there are mathematical concepts used to determine the success of these algorithms: convergence, consistency and stability.

- **Convergence** is the property of a numerical method to produce a solution which approach the exact solution as the grid spacing, control volume size or element size is reduces to zero. [2]
- **Consistent** numerical schemes produce system of algebraic equations which can be demonstrated to be equivalent to the original governing equation as the grid spacing tends to zero. [2]
- **Stability** is associated with damping of errors as the numerical method proceeds. If a technique is not stable even round off errors in the initial data can cause wild oscillations or divergence. [2]

3.2 Conservation Laws of Fluid Motion

3.2.1 Governing equations of fluid flow

The basic principles that govern the implementation of CFD are the governing equation of fluid flow. Those principles represent mathematical statements of the conservation laws of physics which are: (1) mass conservation and (2) momentum equation.

(1) Mass conservation in three dimensions

This law of physics states that the mass of a fluid is conserved. It says that the rate of increase of mass in a fluid element is equal to the net rate of flow of mass into the fluid element

.

The rate of increase of mass in the fluid element for an incompressible fluid (with constant density) is:

$$\mathrm{div}(\mathbf{u}) = 0 \tag{3.1}$$

or in longhand notation:

$$\frac{\partial u}{\partial x} + \frac{\partial v}{\partial y} + \frac{\partial w}{\partial z} = 0 \tag{3.2}$$

Equation (3.1) is the steady, three-dimensional mass conservation or continuity equation at a point in an incompressible fluid. The term on the left side describe the net flow of mass out of the element across its boundaries and is called the convective term.

(2) Momentum equations in three dimensions

Newton's second law states that the rate of increase of momentum of a fluid particle equals the sum of force done on a fluid particle. We distinguish two types of forces on a fluid particle: surface forces (pressure and viscous forces) and body forces (gravity, centrifugal, Coriolis and electromagnetic forces). Usually, the surface forces are represented as separate terms in the momentum equation and the body forces are introduced as source terms.

The rate of increase of x -, y -, z - component of momentum equation (momentum per unit volume of a fluid particle) are given by:

$$\rho \frac{Du}{Dt} = \frac{\partial(-P+\tau_{xx})}{\partial x} + \frac{\partial \tau_{yx}}{\partial y} + \frac{\partial \tau_{zx}}{\partial z} + S_{Mx} \tag{3.3a}$$

$$\rho \frac{Dv}{Dt} = \frac{\partial \tau_{xy}}{\partial x} + \frac{\partial(-P+\tau_{yy})}{\partial y} + \frac{\partial \tau_{zy}}{\partial z} + S_{My} \tag{3.3b}$$

$$\rho \frac{Dw}{Dt} = \frac{\partial \tau_{xz}}{\partial x} + \frac{\partial \tau_{yz}}{\partial y} + \frac{\partial(-P+\tau_{zz})}{\partial z} + S_{Mz} \tag{3.3c}$$

On the left side of equations (3.3a-c) is the rate of increase of x-, y-, or z-momentum per unit volume of a fluid particle. The right hand side of this equations describes total forces in x-, y- or z- direction on the element due to surface

stresses (pressure and shear stresses) plus rate of increase of momentum due to sources. The convention of the pressure term is opposite to that associated with the normal viscous stress, because tensile stresses are usually considered to be positive normal stresses, so the pressure, which is by definition a compressive normal stress, has a minus sign. The source terms S_{Mx}, S_{My} and S_{Mz} include contribution due to body forces only (for example, for gravity: S_{Mx} = 0, S_{My} = 0, $S_{Mz} = -\rho \cdot g$).

3.2.2 Navier-Stokes equations

Under the assumption of a Newtonian fluid (which is valid for almost all gases and most liquids), the components of a shear stress tensor τ are linear dependent on the deformation of the fluid. The three-dimensional form of Newton's law of viscosity for incompressible flows involves two constants of proportionality: the (first) dynamic viscosity, μ, to relate stresses to linear deformations, and the (second) kinematic viscosity, ν, to relate stresses to volumetric deformation. The system of equations describing the motion of fluids (the continuity equation and the three momentum equations) is referred to as the Navier-Stokes equations in CFD applications. The Navier-Stokes equations can be written in the most useful form for the development of the finite volume method:

$$\rho \frac{Du}{Dt} = -\frac{\partial p}{\partial x} + \mathrm{div}(\mu\ \mathrm{grad\ u}) + S_{Mx} \tag{3.4a}$$

$$\rho \frac{Dv}{Dt} = -\frac{\partial p}{\partial y} + \mathrm{div}(\mu\ \mathrm{grad\ v}) + S_{My} \tag{3.4b}$$

$$\rho \frac{Dw}{Dt} = -\frac{\partial p}{\partial z} + \mathrm{div}(\mu\ \mathrm{grad\ w}) + S_{Mz} \tag{3.4c}$$

3.2.3 Conservative form of the governing equations of fluid flow

To summarize, the conservative or divergence form of the system of equations which governs the three-dimensional steady state fluid flow of a incompressible Newtonian fluid are given below:

Mass: $$\mathrm{div}(\mathrm{u}) = 0 \tag{3.1}$$

x- momentum: $$\mathrm{div}(\mathrm{u}\mathbf{u}) = -\frac{1}{\rho}\frac{\partial P}{\partial x} + \mathrm{div}(\nu\,\mathrm{grad}\,\mathrm{u}) + S_{Mx} \tag{3.5a}$$

y- momentum: $$\mathrm{div}(\mathrm{v}\mathbf{u}) = -\frac{1}{\rho}\frac{\partial P}{\partial y} + \mathrm{div}(\nu\,\mathrm{grad}\,\mathrm{v}) + S_{My} \tag{3.5b}$$

y- momentum: $$\mathrm{div}(\mathrm{w}\mathbf{u}) = -\frac{1}{\rho}\frac{\partial P}{\partial z} + \mathrm{div}(\nu\,\mathrm{grad}\,\mathrm{w}) + S_{Mz} \tag{3.5c}$$

The terms of the momentum equations (3.5a-c) represent: convection acceleration on the left hand side; and pressure gradient, viscosity and the source term respectively on the right hand side.

3.2.4 Classification of physical behaviour and fluid flow equations

There are two principal categories of physical behaviour: equilibrium problems and marching problems.

Transient heat transfer, all unsteady flows and wave phenomena are examples of the marching or propagation problems. These problems are governed by parabolic or hyperbolic equations. This type of physical behaviour will not be analysed further in the text, because it is irrelevant for the development of this master thesis.

Equilibrium problems are steady state situations (like the problem in this research), these are governed by elliptic equations. The prototype elliptic equation is Laplace‘s equation which describe the irrotational flow of an incompressible fluid and steady state conductive heat transfer. In two dimensions we have:

$$\frac{\partial^2 \emptyset}{\partial x^2} + \frac{\partial^2 \emptyset}{\partial y^2} = 0 \tag{3.6}$$

An important feature of elliptic problems is that a disturbance in the interior of the domain changes the solution everywhere else, causing solutions to physical problems described by elliptic equations to always be smooth even if the

boundary conditions are discontinuous. To guarantee that informations propagate in all directions, the numerical methods for elliptic problems must allow variables at each point to be effected by all its neighbour's. Elliptic problems are boundary-value problems, while parabolic and hyperbolic problems are initial-boundary-value problems. Solution domain of equilibrium problems is a closed domain (in contrary to marching problems, where the domain is open), and the solution of this problems is always smooth.

3.3 Turbulence Modelling

The Navier-Stokes equations are applicable for both laminar and turbulent flows because there are gained through setting up the instantaneous balance of forces on a differential fluid element. In laminar flows, significant simplifications are possible, while the turbulent flows are always three-dimensional and unsteady even in very simple geometries. Because of this, the N-S equations have to be adjusted in order to be used on turbulent flows. In order to simplify the mathematic description of turbulent flow, the fluid properties and flow characteristics (for example, the velocity u'(t)) can be decomposed into a steady mean value (U) and a fluctuating value (u'(t)) where u(t) = U + u'(t). The fluctuating values are consider as random values and are analysed with statistic methods.

With the statistic approach of turbulent flow problems, the forces on a fluid element are also considered with respect to a time interval and with the mean fluid flow value. The set of adjusted N-S equations are called time-averaged or Reynolds-averaged-Navier-Stokes equations (RANS):

$$\mathrm{div}(\mathrm{U}\mathbf{U}) = -\frac{1}{\rho}\frac{\partial P}{\partial x} + \nu\,\mathrm{div\,grad\,U} + \left[-\frac{\partial \overline{u'^2}}{\partial x} - \frac{\partial \overline{u'v'}}{\partial y} - \frac{\partial \overline{u'w'}}{\partial z}\right] \quad (3.7a)$$

$$\mathrm{div}(\mathrm{V}\mathbf{U}) = -\frac{1}{\rho}\frac{\partial P}{\partial y} + \nu\,\mathrm{div\,grad\,V} + \left[-\frac{\partial \overline{u'v'}}{\partial x} - \frac{\partial \overline{v'^2}}{\partial y} - \frac{\partial \overline{v'w'}}{\partial z}\right] \quad (3.7b)$$

$$\mathrm{div}(\mathrm{W}\mathbf{U}) = -\frac{1}{\rho}\frac{\partial P}{\partial z} + \nu\,\mathrm{div\,grad\,W} + \left[-\frac{\partial \overline{u'w'}}{\partial x} - \frac{\partial \overline{v'w'}}{\partial y} - \frac{\partial \overline{w'^2}}{\partial z}\right]$$

(3.7c)

The RANS equations can be solved numerically with the FVM. The set of equations (3.7a-c) has more unknowns than equations, so it is necessary to introduce additional equations – the turbulence model equations, which generally give equations for Reynold stresses in equations (3.7a-c). There are different turbulence models used in CFD.

For a turbulence model to be useful in general purpose CFD code it must have wide applicability, be accurate, simple and economical to run. The most common turbulence models are:

Classical models: Based on (time-averaged) Reynolds equations:

1. Zero equation model – mixing length model
2. Two-equation model – k-ε model
3. Reynolds stress equation model
4. Algebraic stress model

Large eddy simulation: Based on space-filtered equation [2]

Large eddy simulation are turbulence models where the time-dependent flow equation are solved for the mean flow and the largest eddies and where the effects of smaller eddies are modelled. The mixing length model is cheap, easy to implement but completely incapable of describing flows with separation and recirculation, so it won't be mentioned further in this text. The most widely represented turbulence model in CFD is the k- ε model so the focus of this chapter will be on it.

3.3.1 The k- ε model

Two transport (partial differential) equations are solved in the k- ε model: one for the turbulent kinetic energy k, and the other for rate of dissipation of turbulent kinetic energy ε. The k- ε model is sophisticated and general, but also more costly (than, for example the mixing length model). The model allows describing the effect of transport of turbulence properties by the mean flow and diffusion, also for the production and destruction of turbulence.

The underlying assumption of this model is that the turbulent viscosity μ_t is isotropic, in other words, that the ratio between Reynolds stress and mean rate of deformation is the same in all directions (this assumption fails in many categories of flow). [2]

The k-ε model focusses on the mechanisms that affect the turbulent kinetic energy. Some preliminary definitions are required first. The instantaneous kinetic energy k(t) of turbulent flow is the sum of the mean kinetic energy $K = \frac{1}{2}(U^2 + V^2 + W^2)$ and the turbulent kinetic energy $k = \frac{1}{2}(\overline{u'^2} + \overline{v'^2} + \overline{w'^2})$; $k(t) = K + k$. The governing equation for mean flow kinetic energy K is:

$$\mathrm{div}(K\mathbf{U}) = \mathrm{div}\left(-P\mathbf{U} + 2\nu\mathbf{U}E_{ij} - \mathbf{U}\overline{u'_\iota u'_J}\right) - 2\nu U E_{ij} \cdot E_{ij} + \overline{u'_\iota u'_J} \cdot E_{ij} \quad (3.8)$$

in words for the mean kinetic energy K we have:

Transport of K by convection	=	Transport of K by pressure, viscous stresses and Reynolds stresses	-	Rate of dissipation of K	+	Turbolence production

The governing equation for turbulent kinetic energy k is:

$$\mathrm{div}(k\mathbf{U}) = \mathrm{div}\left(-\overline{p'\boldsymbol{u}'} + 2\nu\overline{\boldsymbol{u}'e'_{\iota J}} - \frac{1}{2}\overline{u'_\iota \cdot u'_\iota u'_J}\right) - 2\nu\overline{e'_{\iota J} \cdot e'_{\iota J}} - \overline{u'_\iota u'_J} \cdot E_{ij} \quad (3.9)$$

in words we have:

Transport of k by convection	=	Transport of k by pressure, viscous stresses and Reynolds stresses	-	Rate of dissipation of k	+	Turbolence production

In equation (3.8) and (3.9) the rate of deformation of a fluid element in a turbulent flow $e_{ij}(t)$ is decomposed into a mean and fluctuating component, $e_{ij}(t) = E_{ij} + e'_{ij}$. In the standard k-$\varepsilon$ model k and ε are used to define velocity scale ϑ and length scale l representative of the large scale turbulence as follows: $\vartheta = k^{1/2}$ and $l = \frac{k^{3/2}}{\varepsilon}$.

The standard model uses the following transport equation for k and ε:

$$\mathrm{div}\,(\mathrm{k}\mathbf{U}) = \mathrm{div}\left[\frac{\mu_t}{\sigma_k}\, grad\ k\right] + 2\mu_t E_{ij} \cdot E_{ij} - \rho\varepsilon \qquad (3.10)$$

$$\mathrm{div}\,(\varepsilon\mathbf{U}) = \mathrm{div}\left[\frac{\mu_t}{\sigma_\varepsilon}\, grad\ \varepsilon\right] + C_{1\varepsilon}\frac{\varepsilon}{k}2\mu_t E_{ij}E_{ij} - C_{2\varepsilon}\rho\frac{\varepsilon^2}{k} \qquad (3.11)$$

In words the equations are:

Transport of k or ε by convection	=	Transport of k or ε by diffusion	+	Rate of dissipation of k or ε	-	Rate of destruction of k or ε

where the eddy viscosity is: $\mu_t = \mathrm{C} \cdot \rho \cdot \theta \cdot l = \rho \cdot C_\mu \cdot \frac{k^2}{\varepsilon}$

The equations (3.10) and (3.11) contain five adjustable constants: C_μ, σ_k, σ_ϵ, $C_{1\varepsilon}$ and $C_{2\varepsilon}$. The standard values for those constants for a wide range of turbulent flows are:

C_μ = 0.09, σ_k = 1.00, σ_ϵ = 1.30, $C_{1\varepsilon}$ = 1.44, $C_{2\varepsilon}$ = 1.92.

Generally, there are advantages and disadvantages of the k-ε model, some of them will be listed below:

- Advantages:
  - Simplest turbulence model for which only initial and/or boundary condition need to be supplied.
  - Excellent performance for many industrial relevant flows.

  - Well established: the most widely validated turbulence model
- Disadvantages:
  - More expensive to implement than mixing length model (two additional PDEs).
  - Poor performance in a variety of important cases such as: some unconfined flows, flows with large extra strains, rotating flows, fully developed flows in in non-circular ducts.

Some other turbulence models which will be shortly discussed in this text are the Reynolds stress equation model (RSM) and the algebraic stress equation model (ASM). The RSM model (ore the second order closure model) is the most complex classical turbulent model. RSM is potential the most general of all classical turbulent models, very accurate calculation of mean flow properties and all Reynolds stresses can be performed with this turbulence model. Disadvantages of the RSM are that the computing cost is very large (seven extra PDEs), this model is not as widely validated as the mixing length and k-ε models and the performance of this model in some flows is poor as of the k-ε. The ASM solves the anisotropy of Reynolds stresses without going to the full length of solving the Reynolds stress transport equations. This is a more economical method than RSM, but the ASM is not widely validated as the mixing length and k-ε models.

3.3.2 Near Wall Modelling

All walls from the numerical model are considered smooth and as no slip walls (see chapter 4.3 Boundary Conditions).

Near a no-slip wall, there are strong gradients in the dependent variables. In addition, viscous effects on the transport processes are large. The representation of these processes within a numerical simulation raises the following problems:

- How to account for viscous effects at the wall.
- How to resolve the rapid variation of flow variables that occurs within the boundary layer region. [3]

The near-wall region can be subdivided into two layers. The so-called viscous sublayer next to the wall, where the flow is almost laminar-like, and where the (molecular) viscosity plays a dominant role. Further away from the wall, in the logarithmic layer, turbulence dominates the mixing process. Between the viscous sublayer and the logarithmic layer, there is a so-called buffer layer, where the effects of molecular viscosity and turbulence are of equal importance. The figure below illustrates these subdivisions of the near-wall region.

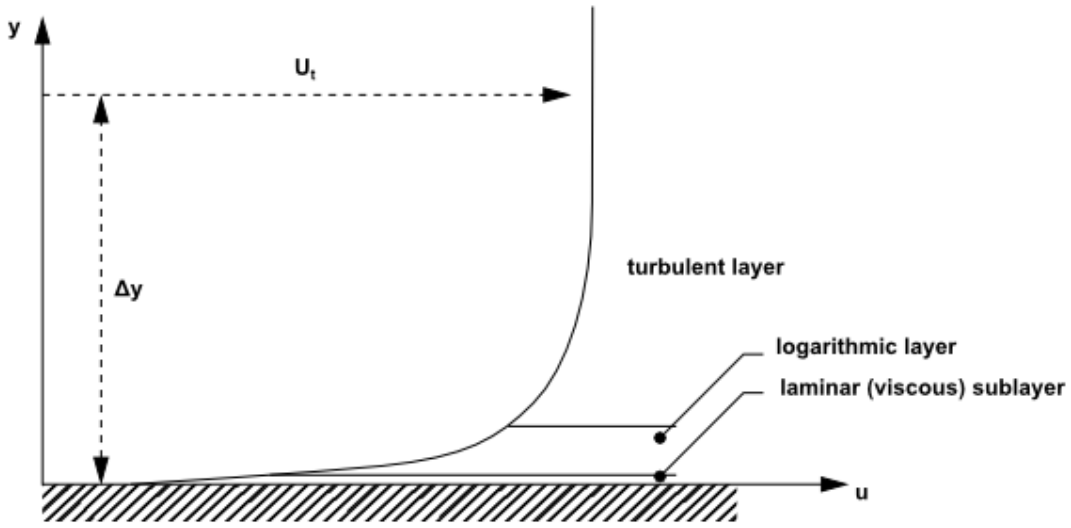

Figure 10: Subdivisions of the near-wall region [3]

The logarithmic velocity distribution near the wall provides a means to numerically compute the fluid shear stress as a function of the velocity at a given distance from the wall, which is known as a 'wall function'. The logarithmic nature of the near wall fluid behaviour yields the well- known 'log law of the wall.' The wall function method is one approache to model flow in the near-wall region. It uses empirical formulas that force suitable conditions near the wall without resolving the boundary layer. The major advantages of the wall function approach is that the high gradient shear layers near walls can be modeled with relatively coarse meshes, leading to savings in CPU time and storage. In CFX, scalable wall functions is used for the k-ε turbulence model. Advantage of scalable wall functions is that they can be applied on arbitrarily fine meshes.

One of the most essential problems for the optimal performance of turbulence models is the proper resolution of the boundary layer. Criteria for judging the quality of a mesh is the minimum spacing between nodes in the boundary layer,

which is the required near wall mesh spacing, Δy, expressed in terms of Reynolds number, running length, L, and a Δy^+ target value. This target value depends on the flow type and the turbulence model in use (that is, on the near-wall treatment in use). Yplus (y^+) is the dimensionless distance from the wall. It is used to check the location of the first node away from a wall. The formula for calculating Δy is prescribed in the ANSYS Modeling Guide [3] and given in the equation (3.12):

$$\Delta y = L \cdot \Delta y^+ \sqrt{74} Re_L^{-13/14} \tag{3.12}$$

This equation allows us to set the target Δy^+ value at a given x location and obtain the mesh spacing, Δy for nodes in the boundary layer.

3.4 Methodology of the Finite Volume Method

The finite volume method is a special form of the finite difference method (FDM), as said before. The approach of the FDM is to discretize the region of interest whit a grid and with nods connecting the grid elements. The values at every nod are calculated by substitution of fluid flow approximations in the integral equations. The fault of this kind of approach is that the mass inflow must not be equal to the mass outflow, therefore the law of mass conservation is not obtained. In the FVM, the region of interest is also divided with a grid and nods, but in contrary to the FDM, an entire section is added around each point where the flux of a fluid flow property is calculate. This approach is very good at conservation of mass in the whole region of interest. The numerical algorithm of FVM consists of three main steps:

- Formal integration of the governing equations of fluid flow over all the (finite) control volumes of the solution domain.
- Discretization involves the substitution of a variety of finite-difference-type approximations for the terms in the integrated equation representing flow processes such as convection, diffusion and sources. This converts the integral equations into a system of algebraic equations.
- Solution of the algebraic equations by an iterative method.

The first step, the control volume integration, express the (exact) conservation of relevant properties for each finite size cell. This distinguishes the FVM from all other CFD techniques. The conservation of a general flow variable ∅, for example a velocity component, within a finite control volume can be expressed as a balance between the various processes tending to increase or decrease it. In words we have:

Rate of change of ∅ in the control volume with respect to time	=	Net flux of ∅ due to convection into the control volume	+	Net flux of ∅ due to diffusion into the control volume	+	Net rate of creation of ∅ inside the control volume

While solving physical phenomena occurring in CFD, an iterative approach is necessary due to nonlinear and complex nature of the equations. For each iteration an error, or residual is reported as a measure of the overall conservation of the flow properties. For further insight of the FVM methodology refer to Appendix A where an example of solving convection-diffusion problem of a general flow variable ∅ is shown.

3.5 Discretisation Schemes in Finite Volume Method

Discretization schemes are generally divided in central differencing scheme, upwind differencing scheme, downwind differencing scheme and hybrid differencing scheme (combination between the central and upwind differencing schemes). These schemes can also be first or higher order.

Numerical solutions may be indistinguishable from the exact solution of the transport equation when the number of computational cells is infinitely large irrespective of the differencing method used. However, in practical calculations we can only use a finite-sometimes quite small-number of cells and our numerical results will only be physically realistic when the discretization schemes has certain properties. [2]

The most important ones are: (1) Conservativeness, (2) Boundedness and (3) Transportiveness.

(1) To ensure conservation of ∅ for the whole solution domain, the flux of ∅ leaving the adjacent control volume through the face must be equal to the flux of ∅ entering the adjacent control volume through the same face. To accomplish this, the flux trough a common face must be represented by one and the same expression in adjacent control volumes.

(2) Boundedness states that in the absence of source the internal nodal values of the property ∅ should be bounded by its boundary values. For example, in a steady state conduction problem without sources and with boundary temperatures of 500^0 C and 200^0 C all interior values of T should be less than 500^0 C and greater than 200^0 C. A desirable feature for satisfying the boundedness criterion is the diagonal dominance of the matrix of “coefficients of the discretized equations” (net deviation of every equation in the set of algebraic equations that needs to be solved at each nodal point).
Another essential requirement for boundedness is that all coefficients of the discretized equations should have the same sign (usually all positive). Physically this implies that an increase in the variable ∅ at one node should result in an increase in ∅ at neighbouring nodes.

(3) Transportiveness can be described as the directionality of influencing of a property ∅ in dependence of the Peclet number Pe (measure of relative strengths of convection and diffusion; for Pe = 0 no convection and pure diffusion, for Pe = ∞ no diffusion and pure convection).

3.5.1 The Advection Term

There are several discretisation schemes included in ANSYS CFX [7]. Which one is used in the numerical simulation is dependent on the advection term. The advection term requires the integration point values of ∅ to be approximated in terms of the nodal values of ∅. The advection schemes have the general form:

$$\emptyset_{ip} = \emptyset_{up} + \beta \, \mathrm{div}(\emptyset) \cdot \Delta\vec{r} \tag{3.13}$$

where $\emptyset_{up}$ is the value at the upwind node, and $\vec{r}$ is the vector from the upwind node to the *ip*. Particular choices for β and $\mathrm{div}(\emptyset)$ yield different schemes as described below.

A value of $\beta = 0$ yields the first order upwind scheme. This scheme is a very popular, simple and robust used mostly in steady fluid flow. With the central difference scheme, β is set to 1 and $\mathrm{div}(\emptyset)$ is set to the local element gradient. The first order upwind differencing scheme, unlike central differencing, is able to identify flow direction. The value of property ∅ at a west cell face is always influenced by both $\emptyset_P$ and $\emptyset_W$ in central differencing, which is unsuitable because the west cell face should receive much stronger influencing from node W than from node P. In the upwind or “donor cell” differencing scheme takes that the convected value of ∅ at a cell face is taken to be equal to the value at the upstream node. The upwind differencing scheme has the properties of conservativeness, boundedness and transportiveness which makes this scheme very popular. A major drawback of the first order upwind discretisation scheme is that it produces erroneous results when the flow is not aligned with the grid lines (figure 11). The scheme causes the distributions of the transported properties to become smeared in such problems as shown below.

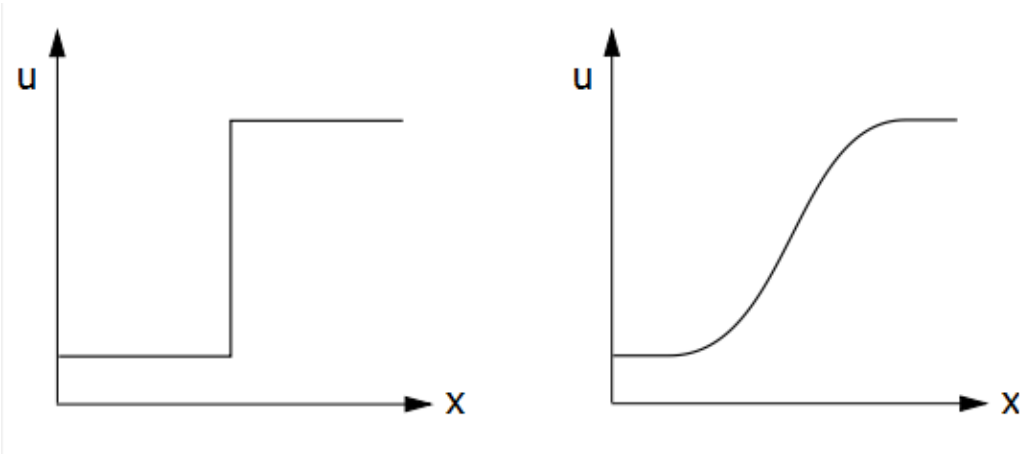

Figure 11: Discretization errors of the first upwind scheme that tend to smear steep spatial gradients [3]

ANSYS CFX [7] uses high resolution schemes by default, which is the case in the simulations done in this research. This means that a special nonlinear term β is used at each node, which is computed to be as close to 1 as possible. The advective flux is then evaluated using the values of β and $\mathrm{div}(\emptyset)$ from the upwind node. The recipe for β is based on the boundedness principles used by Barth and Jesperson [5]. At first, values of $\emptyset_{min}$ and $\emptyset_{max}$ are computed at each node using a matrix involving adjacent nodes (including the node itself). Next, for each integration point around the node, the equation (3.13) is solved for β to ensure that it does not undershoot $\emptyset_{min}$ or overshoot $\emptyset_{max}$.

3.6 Solution of the Discretised Equations

There are two families of solution techniques for linear algebraic equations: direct methods and indirect or iterative methods. Example of direct methods are Cramer's rule matrix inversion and Gaussian elimination. Iterative methods are based on large number of repetitions of simple algorithms leading to eventual convergence. Well-known examples are the Jacoby and Gauss-Seidel point-by-point iteration methods. Iterative methods are generally much more economical than direct methods.

If we focus on solving the Navier-Stokes equations (3.1) and (3.5a-c) we will find that this set of equations presents us with two problems:

- Non-linearity contained in the momentum equations
- Every velocity component appears in each equation (in all momentum equations as well as in the continuity equation) causing all the equations to be coupled together. The most complex problem to resolve is Pressure. It appears in all momentum equations, but there is no (transport or other) equation for pressure.

Both the problems associated with the non-linearity in the equation set and the pressure-velocity linkage can be solved by adopting an iterative solution strategy.

3.6.1 Solution strategy – the coupled solver

The coupled solver solution strategy solves the momentum equations first by using a guessed pressure and an equation for pressure corrections. Because of the 'guess-and-correct' nature of the linear system, a large number of iterations are typically required.

ANSYS CFX [7] uses a coupled solver, which solves the hydrodynamic equations (for u, v, w, p) as a single system. This solution approach uses a fully implicit discretization of the equations at any given time step. For steady-state problems, the time-step behaves like an 'acceleration parameter', to guide the approximate solutions in a physically based manner to a steady-state solution. This reduces the number of iterations required for convergence to a steady-state, or to calculate the solution for each time step in a time-dependent analysis. [3]

The flow chart shown below illustrates the general field solution process used in the CFX-Solver. The solution of each set of field equations consist of two numerical operations for each time step:

1. Coefficient Generation: The nonlinear equations are linearized and assembled into the solution matrix.
2. Equation Solution: The linear equations are solved using an Algebraic Multigrid method. [3]

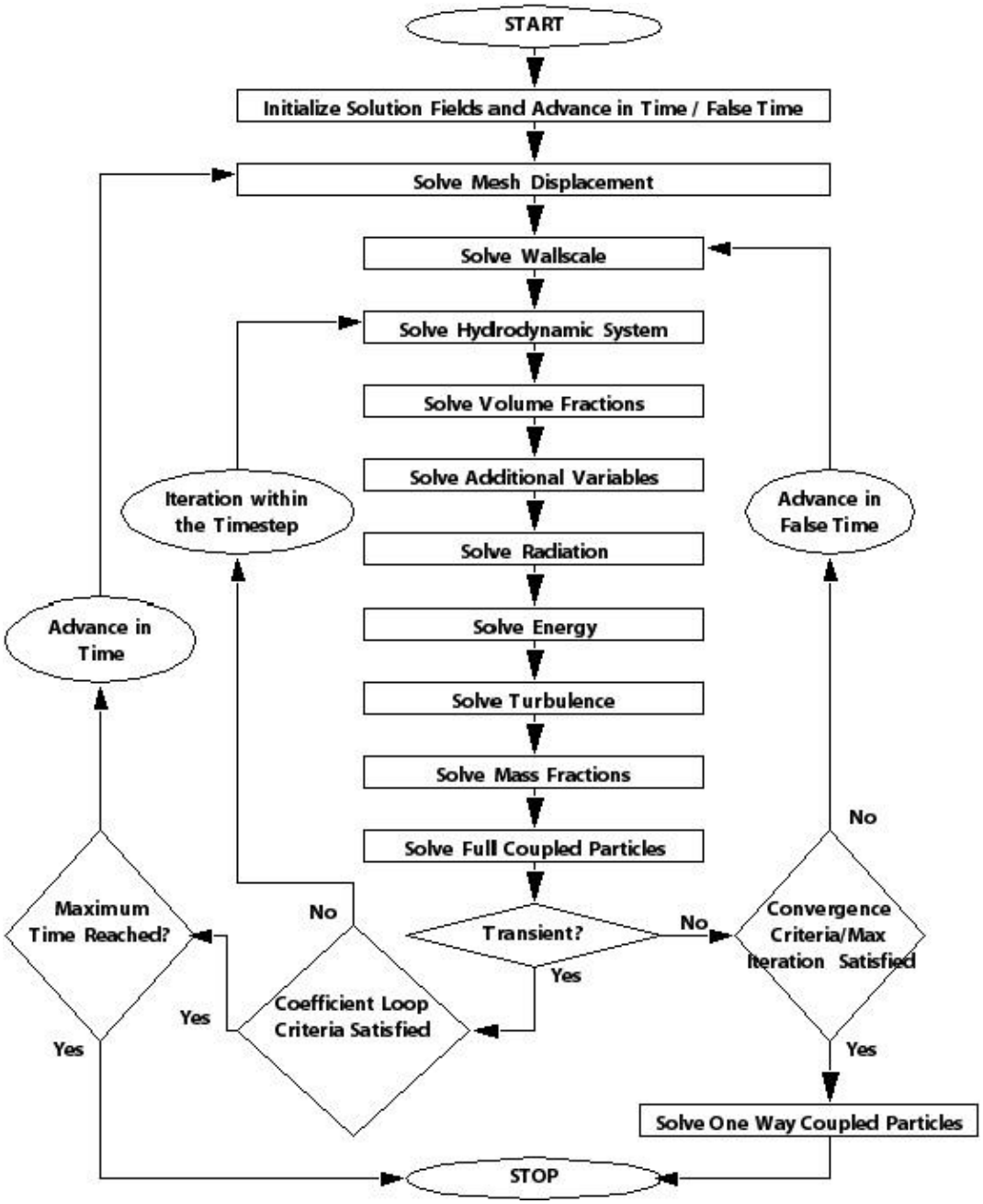

Figure 12: General solution process used in the CFX- Solver [3]

3.6.2 Linear equation solution

The process of linear equations solution can be improved by the use of a technique called Multigrid (MG). The multigrid process performs early iterations on a fine mesh and subsequently increase the mesh size with later iterations. The results are then transferred back from the coarsest mesh to the original fine mesh.

ANSYS CFX [7] uses a Multigrid accelerated Incomplete Lower Upper (ILU) factorization technique for solving the discrete system of linearized equations. It is an iterative solver whereby the exact solution of the equations is approached during the course of several iterations. [3]

The linearized system of discrete equations can be written in the general matrix form:

$$[A][\varphi] = [b] \tag{3.14}$$

Where $[A]$ is the coefficient matrix, $[\varphi]$ the solution vector and $[b]$ is the right hand side.

The above equation can be solved iteratively by approximating the starting solution, φ^n, that has to be improved by a correction, φ' ,to obtain a better solution, φ^{n+1}, which is: $\varphi^{n+1} = \varphi^n + \varphi'$; where the correction φ' is a solution of: $A \cdot \varphi' = r^n$; and r^n is the residual (error), obtained from: $r^n = b - A \cdot \varphi^n$. By repeating this algorithm, solution of desired accuracy can be acquired.

The performance of Iterative solvers such as ILU tend to rapidly decrease as the number of mesh elements increases. Performance also slowes down if there are large element aspect ratios present.

3.6.3 Implementation of Boundary Conditions

Only by implementation of boundary conditions the system of algebraic equation can be solved. Boundary conditions enter the system of equation by cutting of the link to the boundary side and changing the source terms. The appropriate coefficient of the discretised equation is set to zero and the boundary side flux is introduced trough source terms. It is the boundary conditions that produce different solutions for a given geometry and set of physical models, therefore, it is important to set boundary conditions that accurately reflect the real situation to enable you to obtain accurate results.

Types of boundaries available in ANSYS CFX [7] are:

- Inlet
- Outlet
- Opening
- Wall
- Symmetry Plane

The boundary condition should be suitable configured so that the fluid flow problem is neither over-specified nor under-specified. The most robust configuration is to place mass flow or velocity condition at an inlet and static pressure at an outlet. The inlet total pressure is then an implicit result of the prediction. Placing total pressure at an inlet and mass flow/velocity at an outlet is also robust enough, but all other options (such as pressure at inlet and outlet) should be avoided in boundary condition implementation.

In the numerical simulations that were conducted for this master thesis normal speed is chosen as a condition at the inlet. The magnitude of the inlet velocity is specified and the direction is taken to be normal to the boundary. The direction constraint requires that the flow direction, is parallel to the boundary surface normal, which is calculated at each element face on the inlet boundary.

4. Numerical Modelling

This chapter provides insight in the procedures of numerical modelling. In chapter 3.1 it was said that every CFD code consist of three main elements: pre-processing, solver and post-processing. This chapter describes the first two steeps, the pre-processing and solver, while the post-processing is described in the fifth chapter. The pre-processing consist from geometry modelling, grid generation, boundary condition and fluid properties determination. Geometry modelling is described in the chapter 4.1, grid generation (meshing) in the chapter 4.2 and boundary condition including fluid properties determination in chapter 4.3. The solver is described in the chapter 4.4 CFX–Solver.

4.1 Geometry

The geometries generated in this master's thesis were modelled in AutoCAD Mechanical 2015 [8] using the geometries and dimensions from the physical model study (figure below).

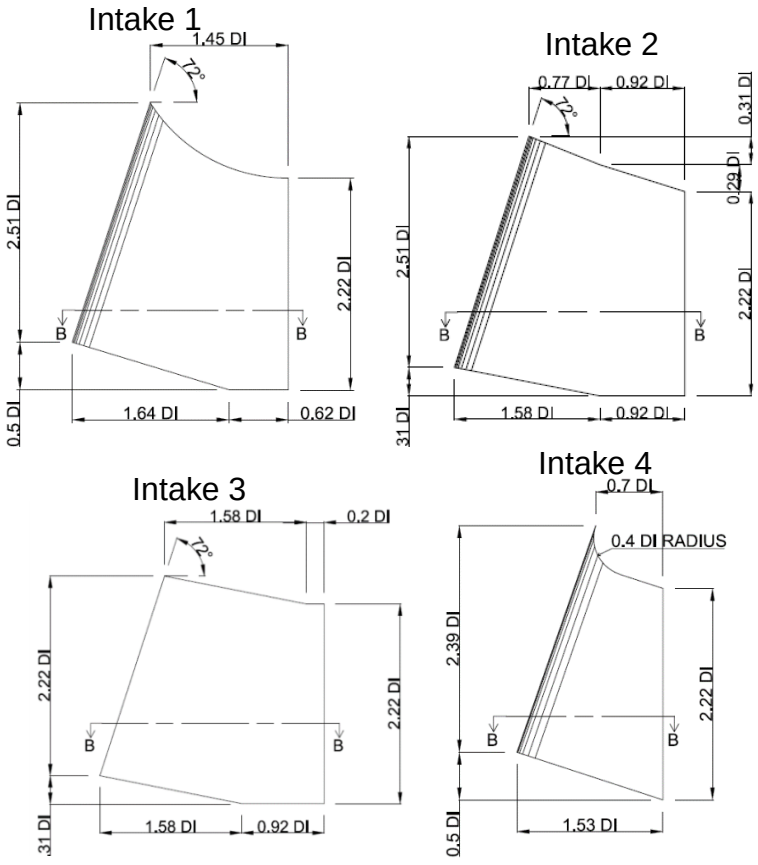

Figure 13: Geometries of the four intakes

4.1.1 3D Geometry

3D geometry of the bulb turbine model was generated by recreating figure 3 in AutoCAD 3D [8]. Figure 14 shows: a 3D view (left insert), a side view (right insert, top) and view from top (right insert bottom). Red areas represent the solid domains of the model: the bulb, wicket gates and the bulb supporting piers, while the remaining areas represent fluid domains. The solid regions from figure 14 were segregated from the 3D geometry before their import into ANSYS CFX [7], because only the fluid region (where water can flow) is required for the numerical procedure.

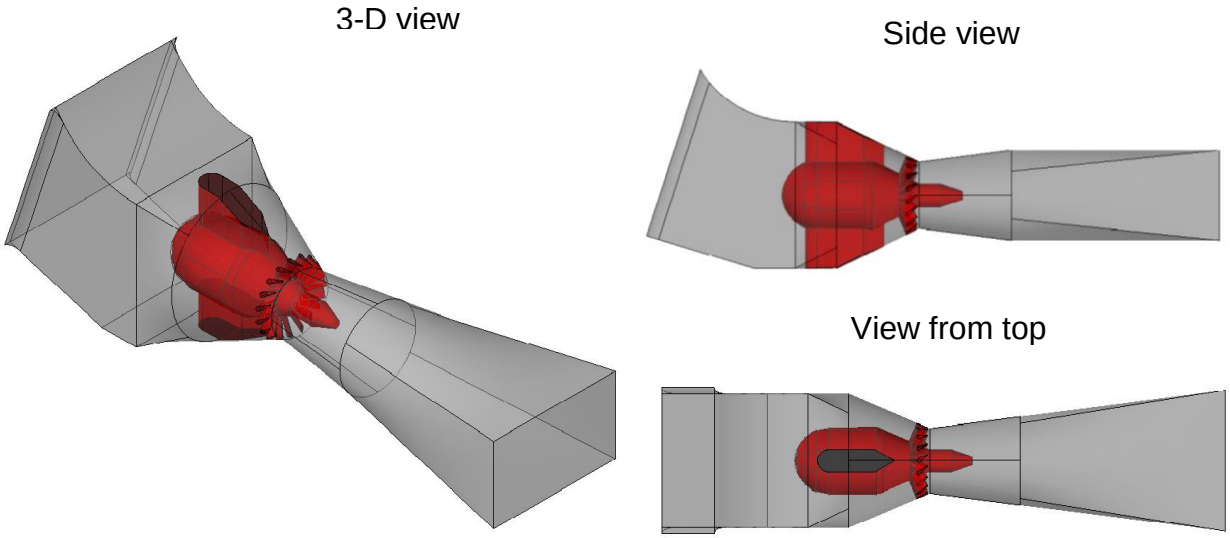

Figure 14: Geometry of bulb turbine model, with intake 1 shown and wicket gates opening angle of 30^0

4.1.2 Intake Models

The four intake models were also created in AutoCAD 3D [8], using the geometry and dimensions from figures 5 – 8. The models are visible in figures 15 – 18.

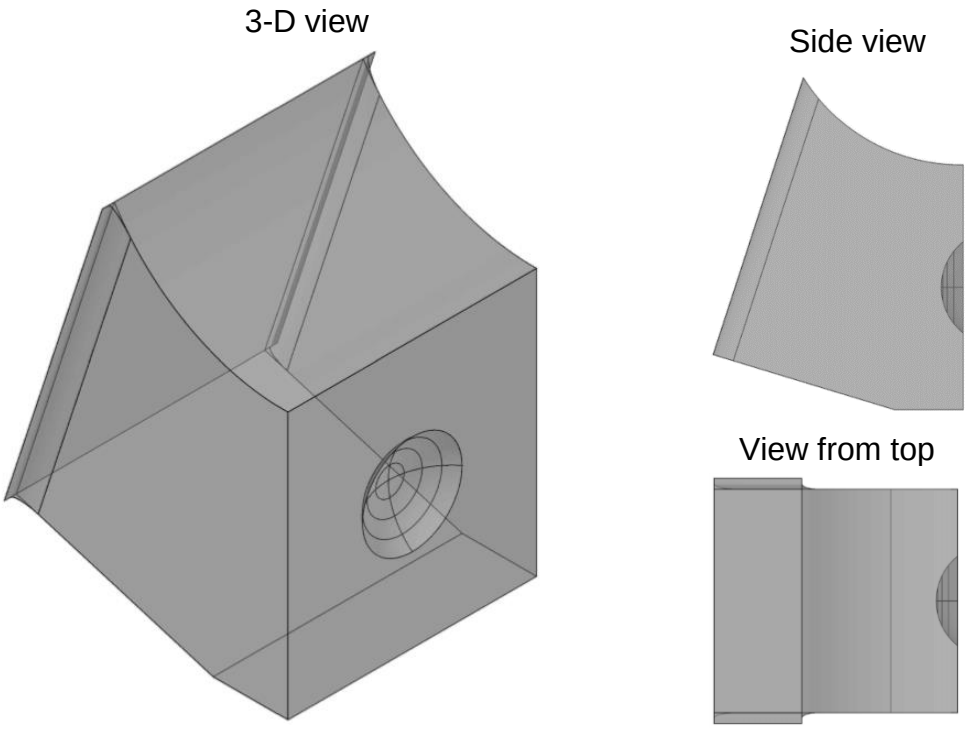

Figure 15: Geometry model for intake 1

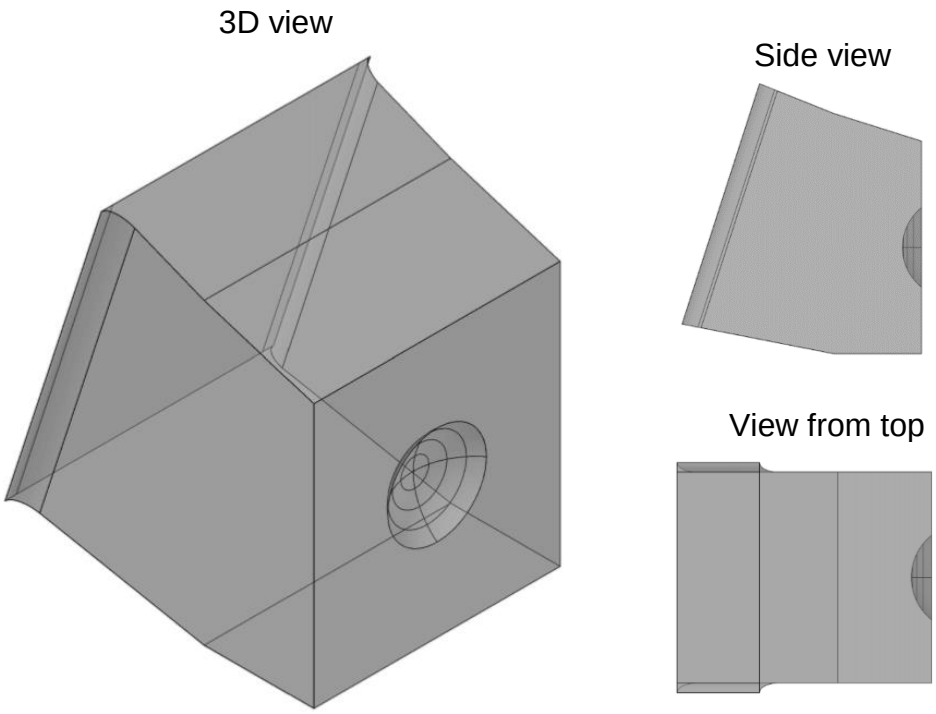

Figure 16: Geometry model for intake 2

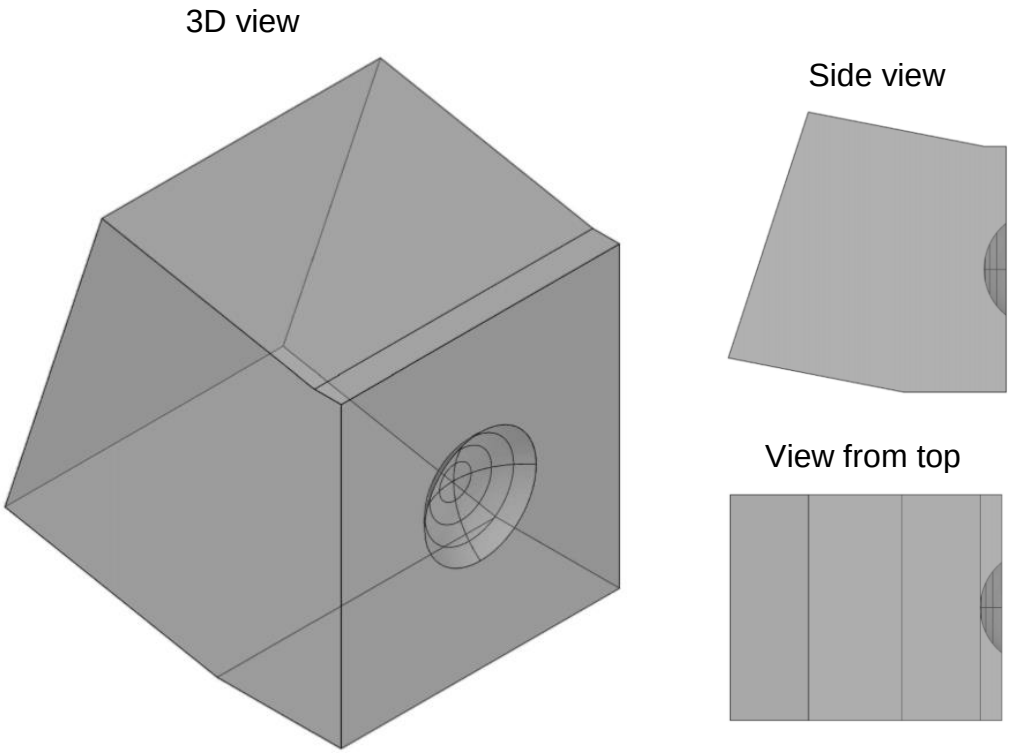

Figure 17: Geometry model for intake 3

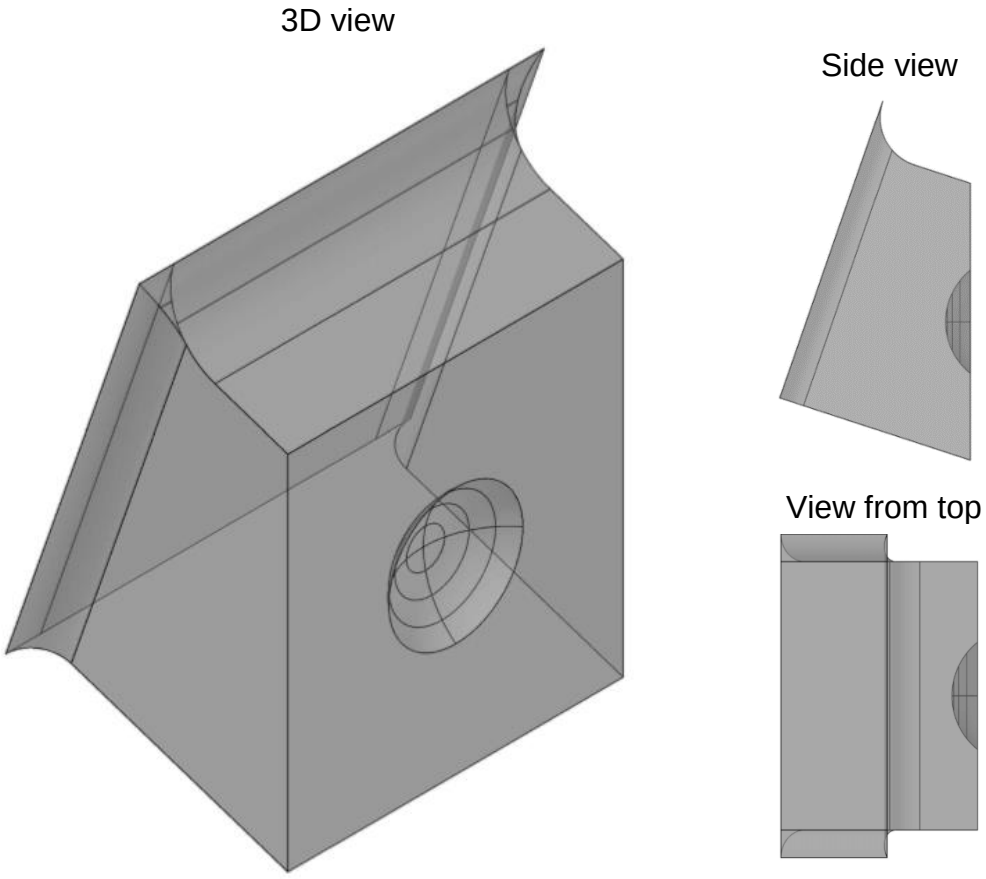

Figure 18: Geometry model for intake 4

4.1.3 Stilling Chamber

Figure 3 shows the schematic diagram of the test apparatus. In the numerical model, there is no need for stilling and measuring apparatus because the velocity of the fluid flowing into the model can be introduced as a boundary condition in ANSYS CFX [7] software. However, for simulating the laboratory conditions as best as possible, it is necessary to create a chamber from which the fluid can flow into the bulb turbine model. The solution is to create a boxlike stilling chamber attached with the turbine model. The first vertical plane of the stilling chamber will be used as inlet boundary condition of the numerical model, which allows assigning desirable velocities to it.

Figure 3 is the only figure of the stilling chamber from the physical model paper and it shows uncertainties regarding its geometry. For instance, the high and depth of the stilling chamber, and the gap between intake models and vertical planes are unclear. Further investigations were made to estimate the stilling chamber geometry. These investigations are more detail described in the sensitivity analysis in chapter 4.2.4. Figures 19, 20 and 21 show the stilling chamber approximation.

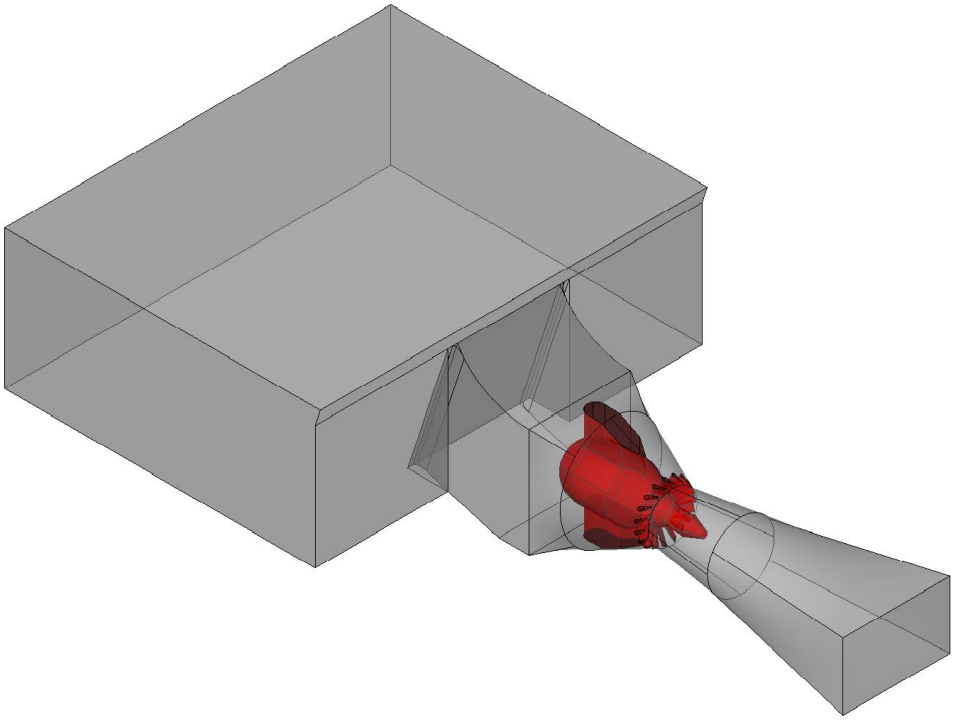

Figure 19: 3D view of the whole model including the stilling chamber with intake 1 shown

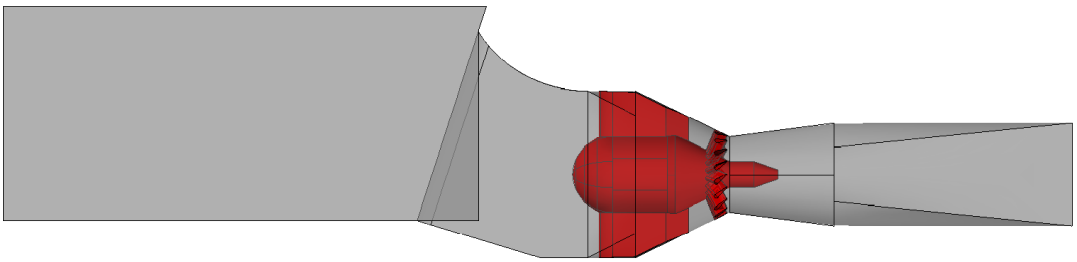

Figure 20: Side view of the whole model including the stilling chamber with intake 1 shown

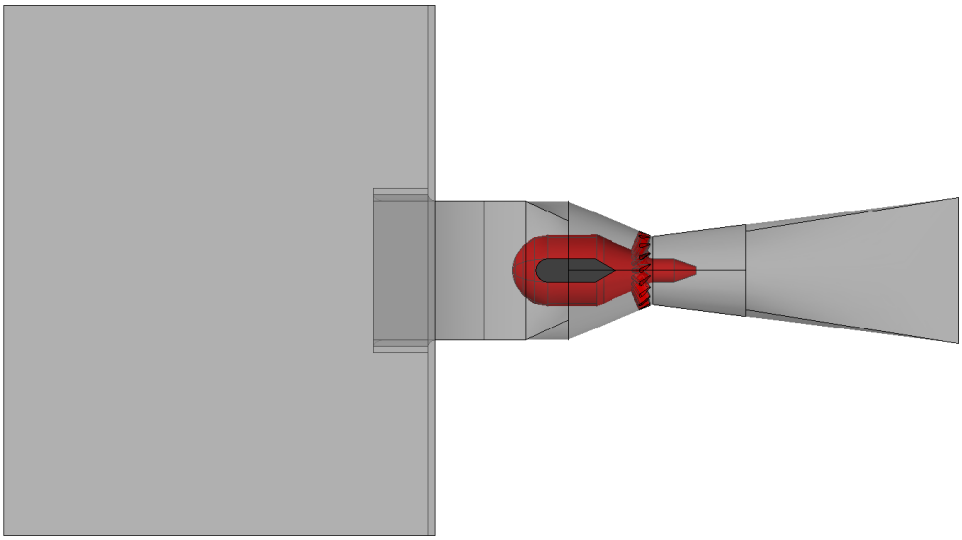

Figure 21: View from top of the whole model including the stilling chamber with intake 1 shown

The 3D geometry from Auto CAD [8] was later exported as a STEP file, and imported in ANSYS Design Modeller [7] where further geometry adaption are possible. Figure below shows the 3D geometry opened with ANSYS Design Modeller [7].

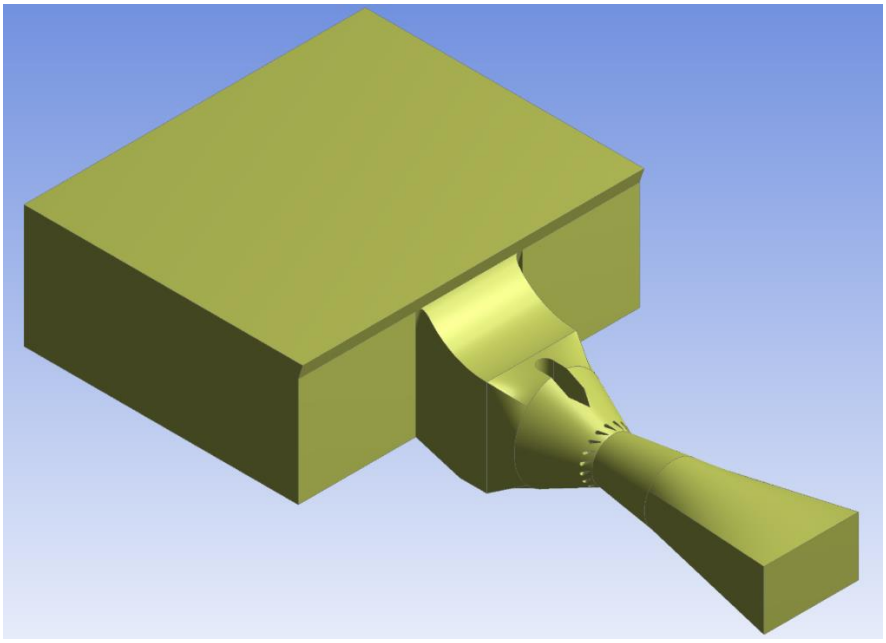

Figure 22: 3D Geometry imported in ANSYS Design Modeller

4.2 Grid Generation

The next step in the numerical modelling process is grid generation. Before continuing with the meshing process, it is desirable to adjust some geometry faults in the Design Modeller in order to improve the meshing quality. For example: merging surfaces and repairing hard edges. Figure 23 shows an example of merging surfaces on the top curve of intake 1, and figure 24 shows an example of hard edges repairing.

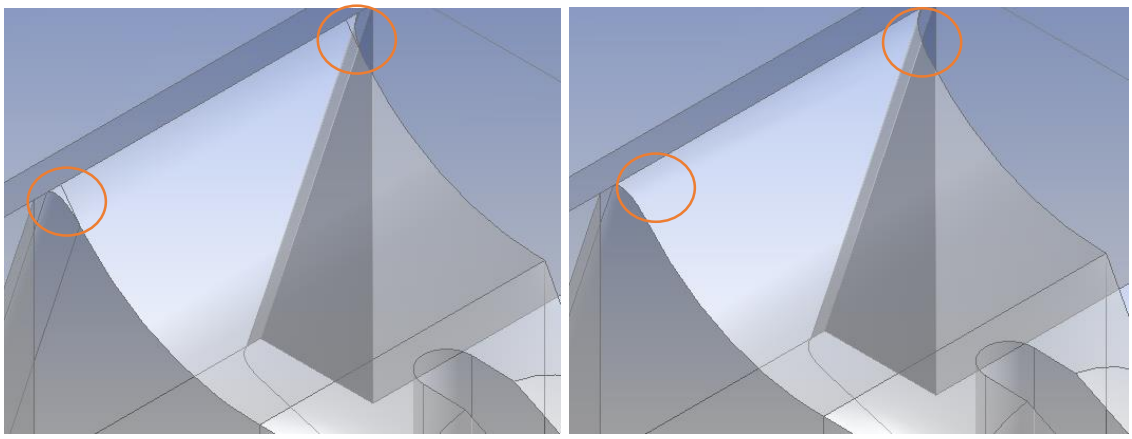

Figure 23: Example of surface merging; before merging (left) and after merging (right)

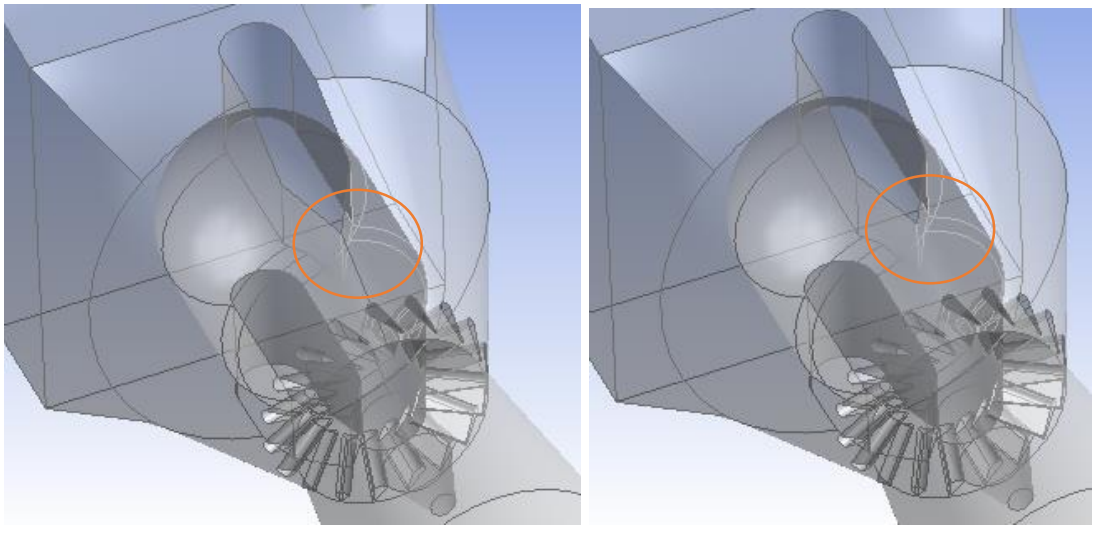

Figure 24: Example of hard edges repairing; before repairing (left) and after repairing (right)

4.2.1 Meshing Process

Meshing for the earlier described geometry is done in ANSYS Meshing [7]. In figure below, the meshed geometry with intake 1 and wicket gates opening of 30^0 is shown. It is visible that the mesh around the wicket gates is finer than in other regions due to small openings and gaps in this area. Using a model with wicket gates in the numerical procedure causes increase of element numbers and nodes. It is of interest to reduce the element numbers, and with it the computing time, so a model simplification is introduced.

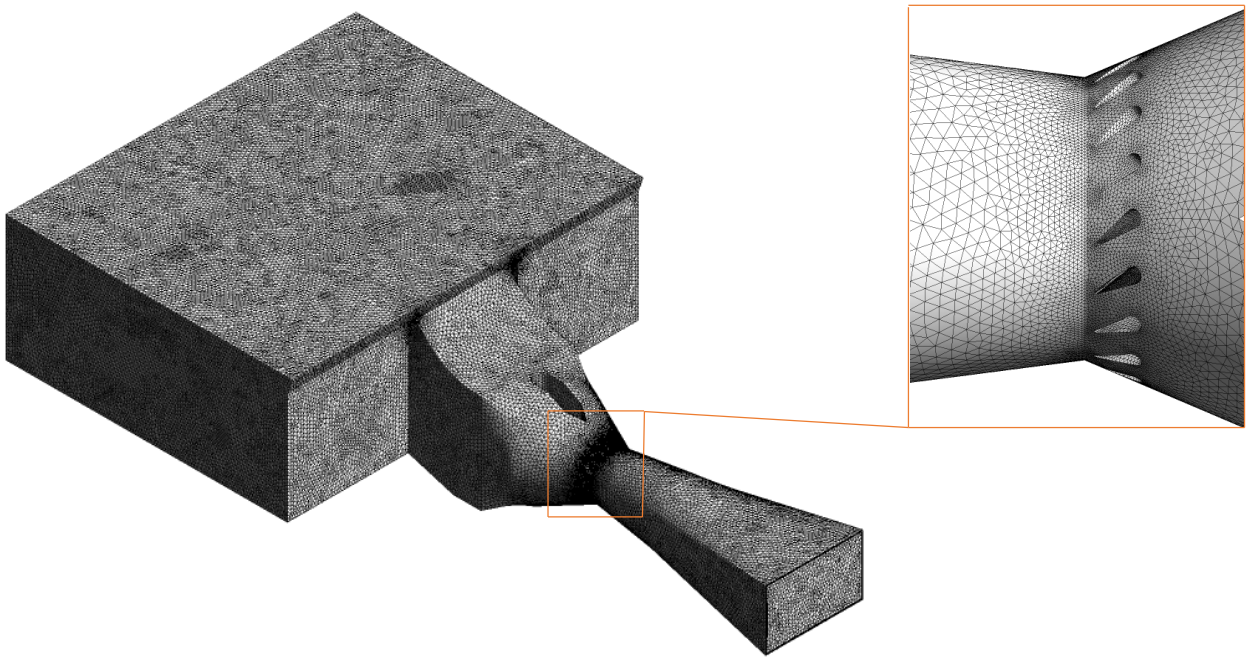

Figure 25: Meshed geometry for intake 1 (left) and mesh around the wicket gates (right)

4.2.2 Model Simplification

In the simplified model geometry, the wicket gates and draft tube are left out and the model is cut in half in flow direction with applying a symmetry plane (figure 26). This simplification is justified because the focus of this thesis is on bulb turbine intake structures and not the flow around the runner blades. Figure 28 shows that the velocity distribution for the full model and the simplified model are almost the same. The number of elements and nodes are reduced with introduction of the simplification. Number of elements drop from 6.6 Mio to 2.7

Mio and number of nodes drop from 1.4 Mio to 581 thousand, which reduces the computing time of the numerical simulations nearly four times for using the same PC with the same number of CPU-s.

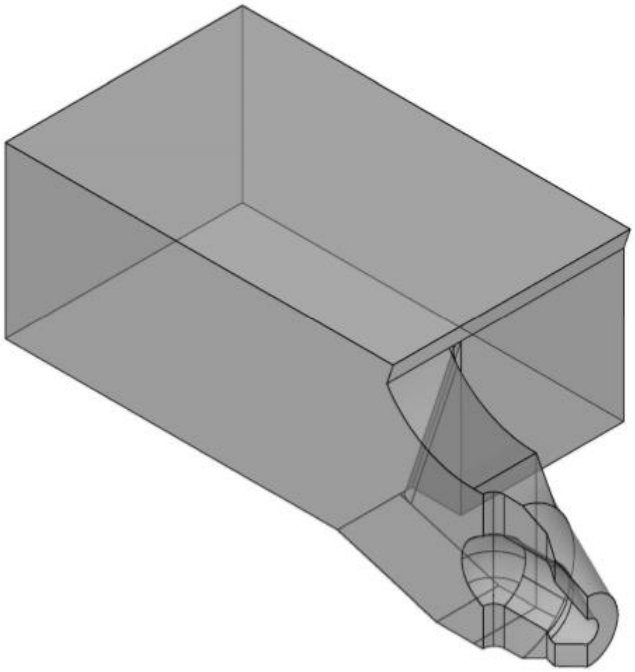

Figure 26: Simplified geometry model for intake 1

Table 1: Comparison between the simple and full model with intake 1

	Full Model	Simple Model
Model Description	Whole model, with wicket gates and draft tube	Model cut in flow direction, no wicket gates, no draft tube
Nr. of Elements	6.6 Mio	2.7 Mio
Nr. of Nodes	1.4 Mio	580 K
Total computing Time	3 h	35 min

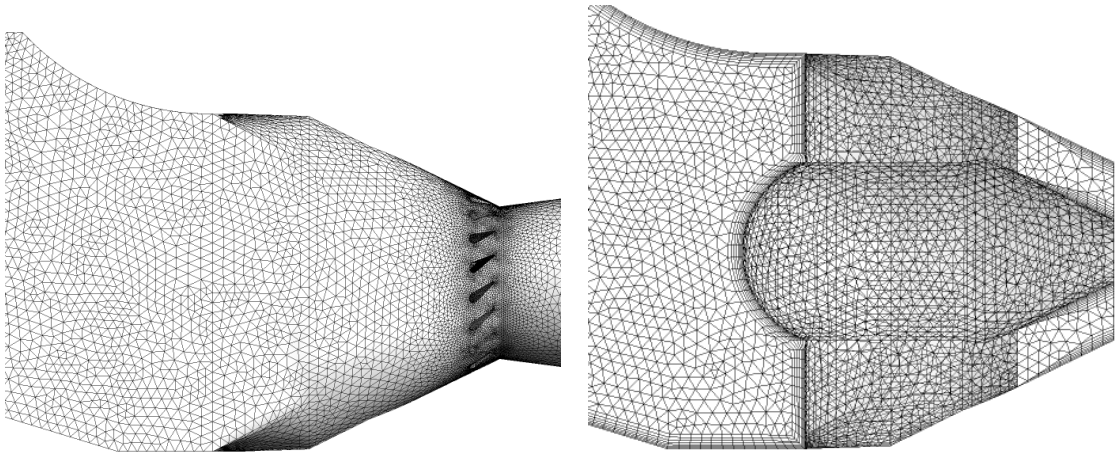

Figure 27: Mesh representation of the full (left) and simplified model (right) around the bulb

Figure below represent the comparison of velocity distributions for simplified and original geometry. Velocities for both models were measured on a vertical plane upstream from the bulb (see figure 43), and the same global mesh size of 0.01 meters was used for both of them. Velocities were presented by means of the velocity coefficient (local velocity divided with mean velocity) $v/\bar{v}$. The two velocity distributions shown in figure below are almost identical. Difference is that for the full model, the velocities are not completely symmetrical, due to the rotational flow caused by the wicket gates. The differences are so small that they can be neglected, and the simplified model can be used in further investigations.

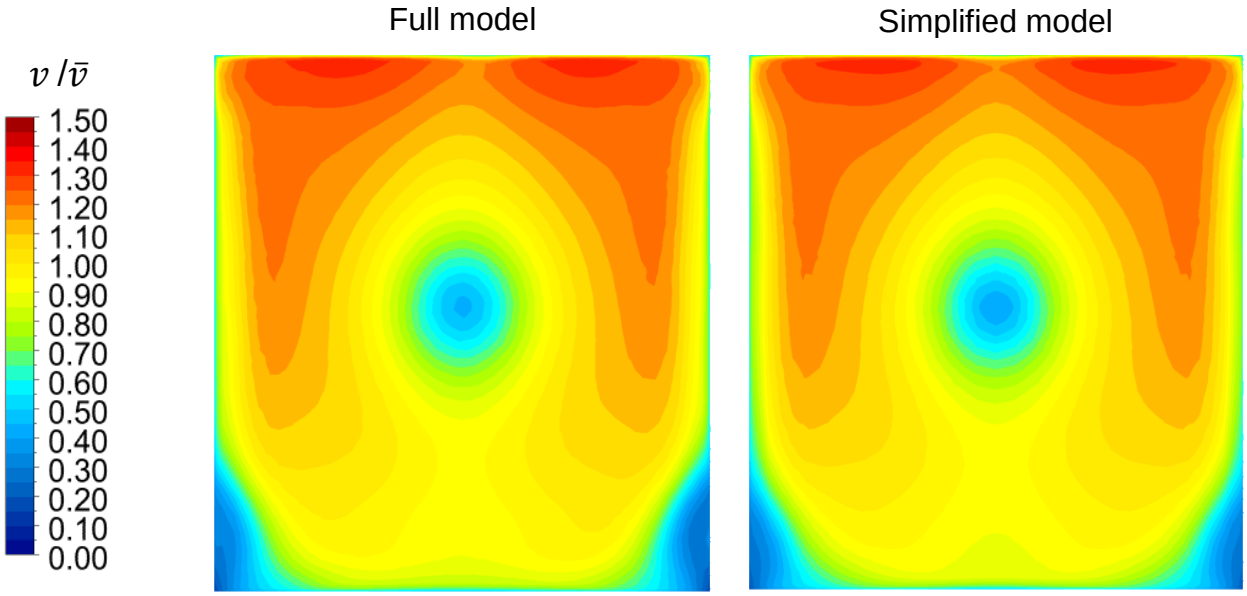

Figure 28: Velocity distribution for the full model (left) and simplified model (right)

4.2.3 Meshing Details

Mesh for the 3D bulb turbine model consist of tetrahedrons, the only way to discretise an irregular geometry like the one used for this research. The global mesh size for the model is set to maximal 0.01 meters and the mesh growth rate is 1.1. ANSYS Meshing [7] defines finer mesh around corners, geometry changes and curvatures automatically. In figure below, change of mesh size on the simplified geometry for global mesh size of 0.02 m is shown. The figure shows the geometry for mesh size 0.02 and not 0.01 meters, because the mesh change on curvature is hardly visible on the finer mesh.

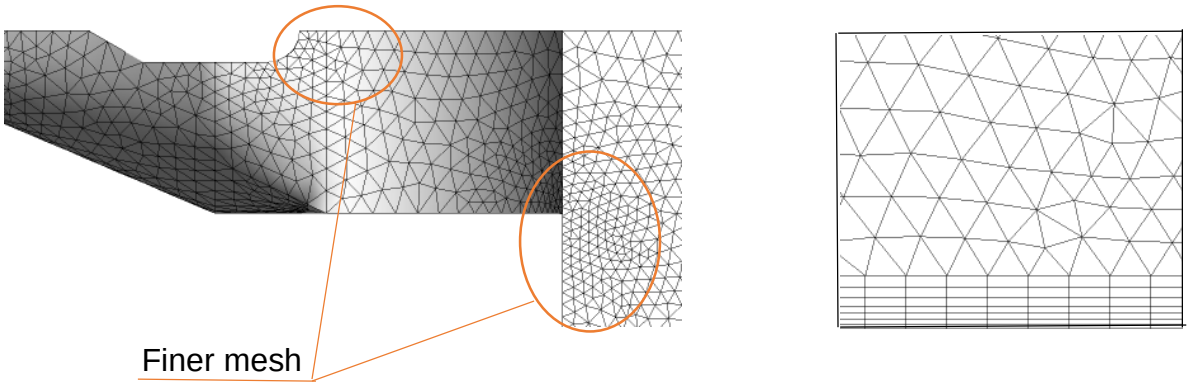

Figure 29: Mesh details (left) and inflation layers (right) for the simplified geometry

Right side of figure 29 show inflation layers near the wall. Inflation layers are added to record near-wall fluid flow. These layers should be adapted so that the difference between the last inflation layer and the layer next to it is not significant. Inflation is added on all surfaces except the inlet, outlet and symmetry surfaces. The inflation method is the “first layer thickness”, with seven inflation layers, the first layer high of 0.001 meters and growth rate of 1.2. For the whole model, 4 inflation layers were used instead of seven in order to prevail overcrossing of the inflation layers in the small gaps between the wicket gates elements.

4.2.4 Sensitivity Analysis

It was mentioned before that the dimensions of some geometry parameters from the original study were unclear. Figure below displays the unknown geometry values shown on the simplified numerical model. The unknown values are model height, model depth and offset between the intakes and the vertical wall. Tests with different geometry values were made to estimate the unknown parameters.

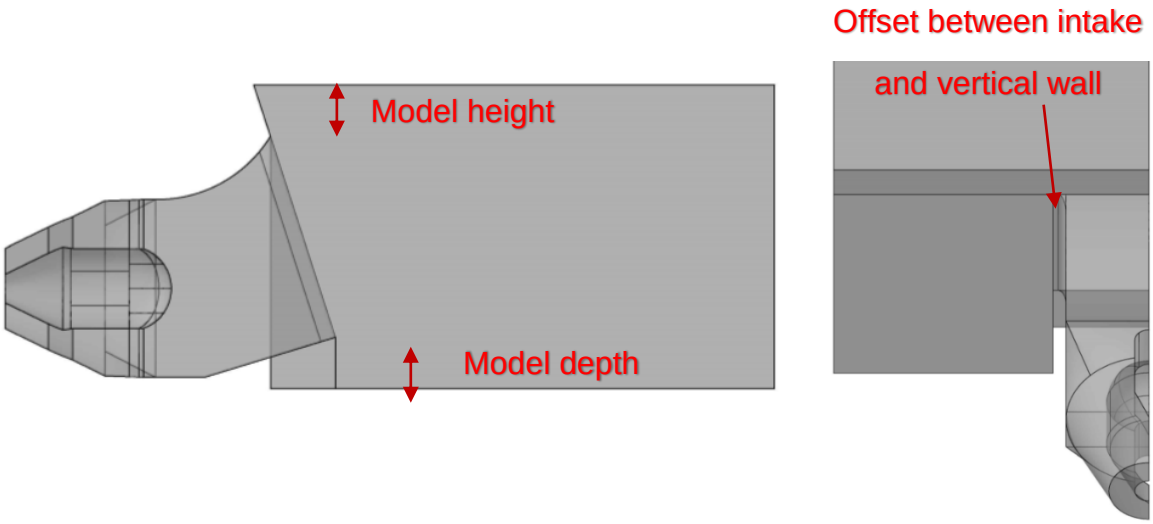

Figure 30: Geometry uncertainties shown on the simplified numerical model

Velocity distributions were compared for every test, and the geometry with results closest to the physical model results were chosen for further investigations.

Velocity distribution for every test were shown in the vertical plane upstream from the bulb (figure 43). The velocities are represented with means of the velocity coefficient (local velocity divided with mean velocity) $v/\bar{v}$. All tests were conducted on intake 1, but the resulting model geometry parameters were applied for other three intakes as well as for the first one.

Figure 31 shows two examples of sensitivity tests with change of model depth. It is visible that lower and middle region of the measurement plane are influenced by the change of model depth. Velocities in the lower region are reducing, and in the middle region increasing for greater bottom depth. After a series of test, it is chosen to leave the bottom depth at 0 m (figure 26).

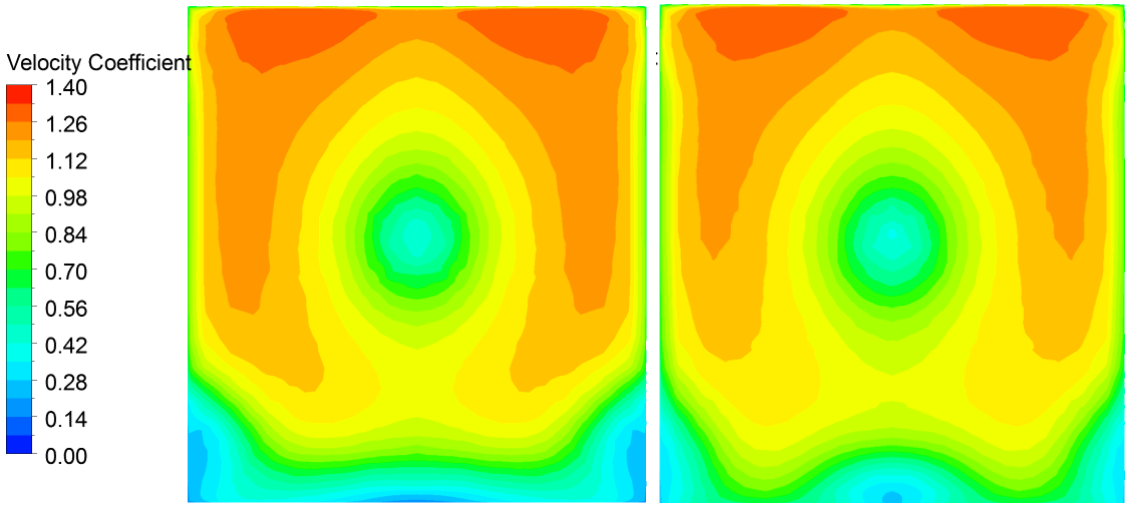

Figure 31: Examples of sensitivity analysis test: bottom depth 10 mm (left) and bottom depth 3 mm (right)

Figure 32 shows tests for addition of extra model height. The upper region of the velocity measurement plane are most affected by increase of model height. It is visible that, with increase of the model height, the velocities in the top region decrease. The highest velocities in the top region are achieved with no extra model height (figure 30 right). Velocity distribution for the geometry without extra model height is the one most closest to the physical model results, but it is not realistic to cut the model just above the intake, so an additional model height of 5 mm is chosen in further investigations (figure 26).

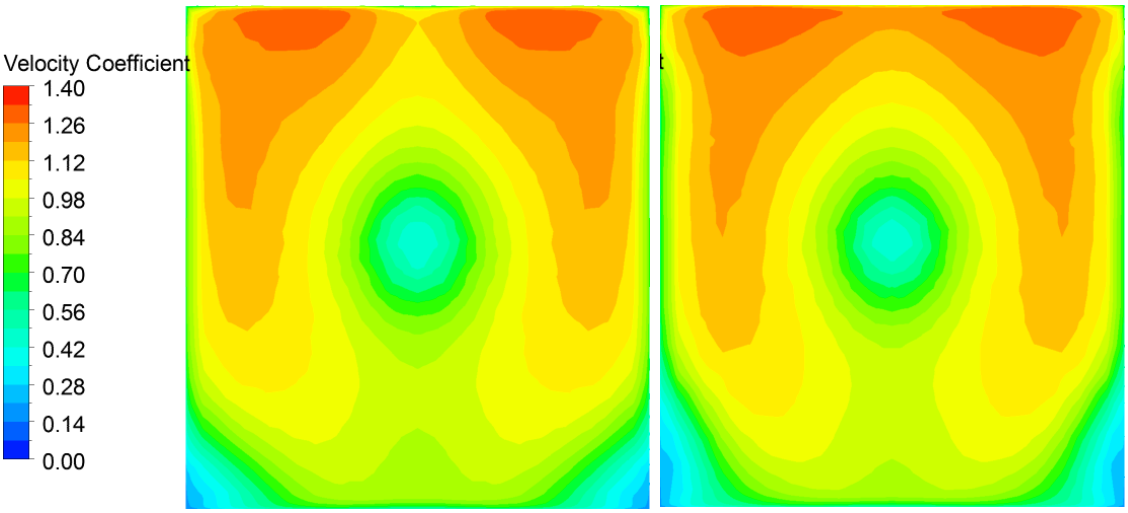

Figure 32: Examples of sensitivity analysis test: model height 10 mm (left) and no extra model high (right)

The figure below shows velocity distributions for change of the offset between intake and vertical plane (figure 30 right). The velocities in the side region are more shifted towards the middle with addition of wall offset, and closer to the wall through decreasing it. The offset between the intake and wall is chosen to be 15 mm (figure 26).

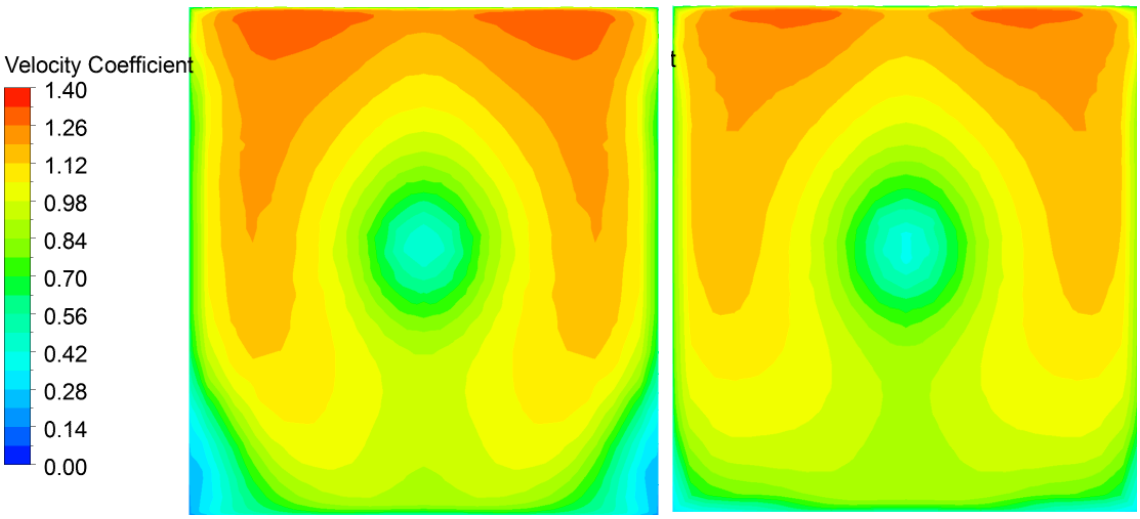

Figure 33: Examples of sensitivity analysis test: wall offset 25 mm (left) and no wall offset (right)

After determining the unknown geometry parameters, the global mesh size has to be estimated in order to continue the numerical modelling process. Test with the same geometry (simplified with intake 1) and different global mesh size for each test were made. Head losses (Δh) were Calculated and compared for each test. Head losses were determined in terms of the total pressure loss (see chapter 5.5). Table 2 shows calculated head losses for geometries with different global mesh size. The coarsest global mesh size analysed is 0.08 m, and the finest one is 0.0075 m. Figure 34 show the convergence of the head losses with change of mesh size. It is visible that the loss does not change much for the mesh size of 0.02, 0.01 and 0.0075, so the global mesh size of 0.01 m is chosen for further analysis. This global mesh size is representative for all four geometry intakes.

Figure 35 shows two geometries with different global mesh size, 0.06 on the left and 0.01 on the right.

Table 2: Head losses for different global mesh size on simplified geometry with intake 1

Global Mesh Size [m]	Dh [m]
0.08	0.42
0.06	0.41
0.04	0.36
0.02	0.34
0.01	0.32
0.0075	0.32

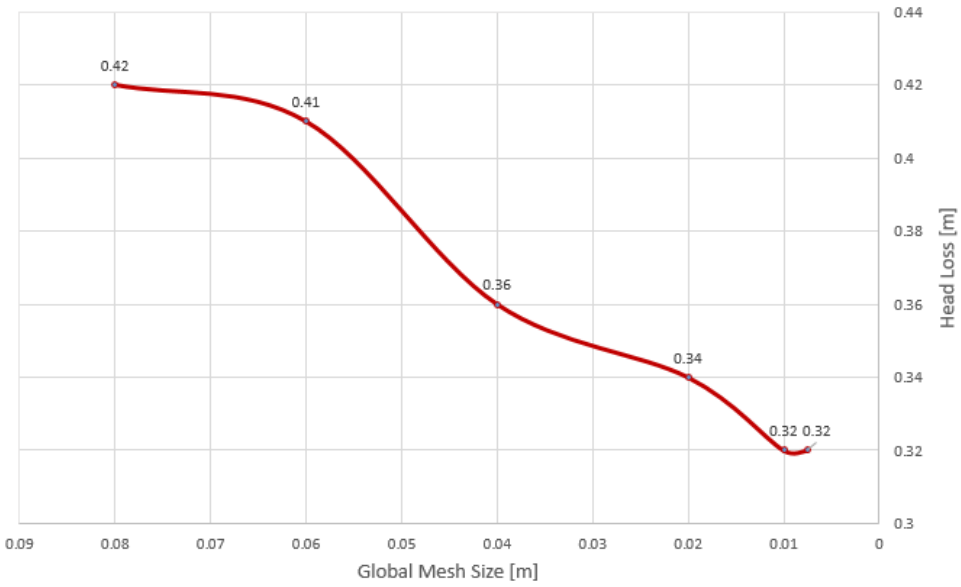

Figure 34: Convergence of head losses with decrease of global mesh size

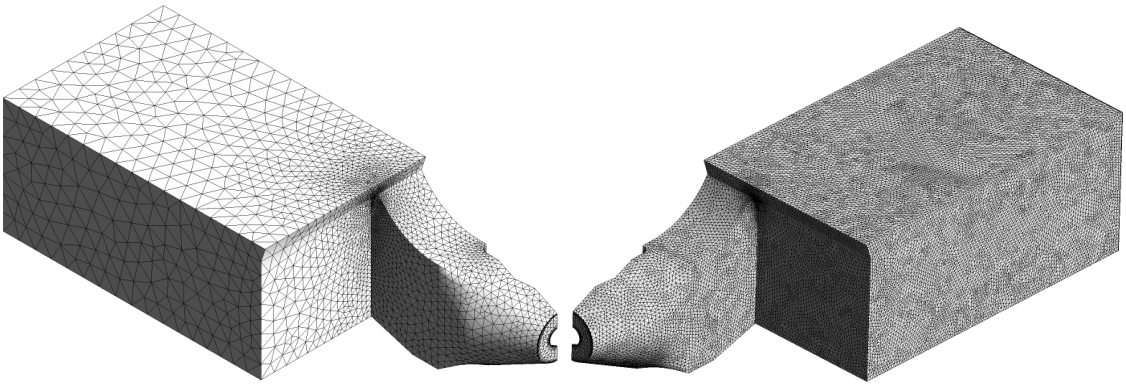

Figure 35: Simplified geometry with intake 1: global mesh size 0.06 (left), global mesh size 0.01 (right)

4.3 Boundary Conditions

The last steps of the pre-process are generated in CFX–Pre where the boundary conditions and fluid flow properties are determined. In Analysis Type, steady state is chosen as the fluid flow regime. In Default Domain, water is chosen as the only domain fluid (it is a single phase simulation), heat transfer is excluded from fluid models, k-epsilon model is chosen as the turbulence model and the wall function is chosen to be scalable. With excluding the heat transfer, the solution equation system is smaller for two PDE's (the energy equation and the equation of state) and therefore the computing time is shorter. The chosen k-epsilon turbulence model is described in chapter 3.3.1.

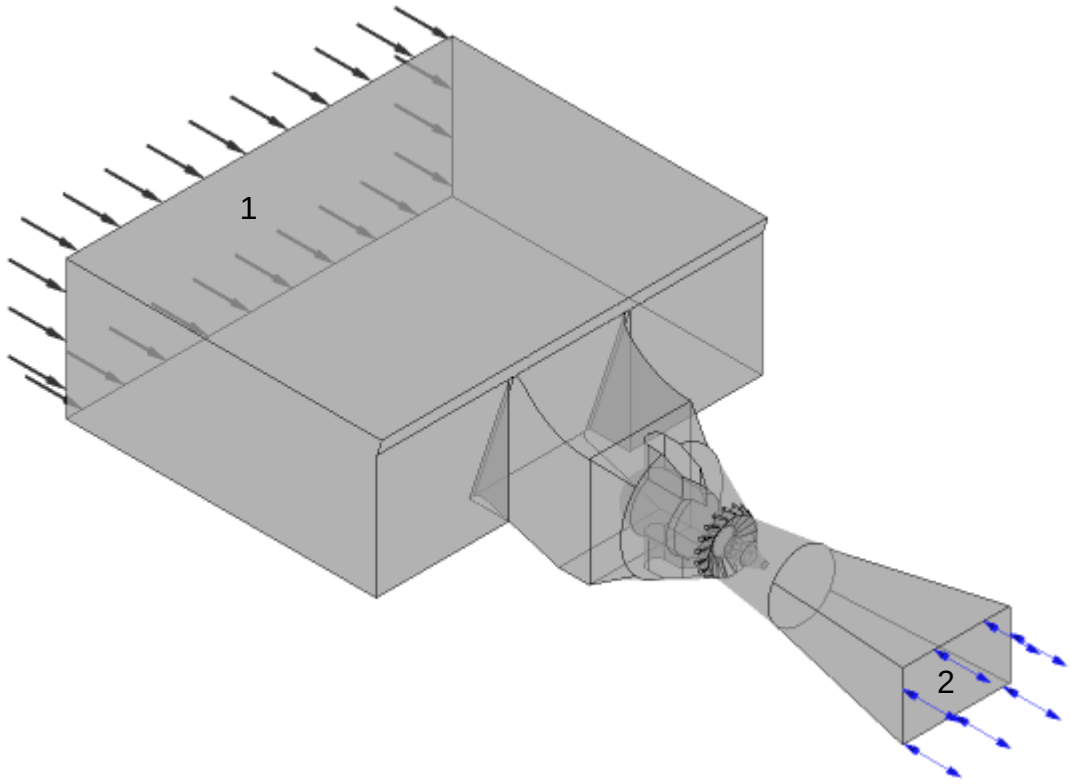

Figure 36: Boundary conditions for the whole model with intake 1 and wicket gates opening of 30^0

The boundary conditions chosen for the full model with intake 1 and wicket gates opening of 30^0 are displayed in figure 36. The boundary condition configuration in this model is placed velocity condition at the inlet and relative pressure at the outlet. The inlet of the fluid domain is set at the vertical plane 1 (with the black arrows pointing the flow direction), where the fluid enters the domain with a normal speed of 0.5 m/s. It was mentioned before that velocity distribution is very

similar for different velocities, so the 0.5 m/s inlet velocity is chosen in order to gain velocities of nearly 1 m/s in the intake regions. The inlet flow regime is set to be subsonic and the turbulence intensity is adjust to medium (= 5 %). The outlet of the fluid domain is set at the vertical plane 2. Boundary type at the outlet is chosen to be an opening condition, which means that the fluid can flow in an out through this boundary. Relative pressure at the outlet is set to be 0 Pa. At first, the boundary type at the outlet of the full model was chosen as outlet boundary condition, but there was backflow registered in the draft tube, just before the plane 2. The CFX solver reported this problem (figure 37), so the outlet boundary condition was changed to opening. All the other surfaces from figure 36 were set as walls. The walls are defined as smooth and no-slip walls. Smooth walls means that the wall friction is neglected and no-slip walls means that the velocity of fluid particles on the border with the wall have a velocity of zero m/s. The boundary conditions for the simplified geometry with intake 1 is shown in figure 38. The vertical plane 3 represent the symmetry plane.

```
+--------------------------------------------------------------------+
|                     ****** Notice ******                           |
|  A wall has been placed at portion(s) of an OUTLET                 |
|  boundary condition (at   3.6% of the faces,   0.8% of the area)   |
|  to prevent fluid from flowing into the domain.                    |
|  The boundary condition name is: outlet.                           |
|  The fluid name is: Fluid 1.                                       |
|  If this situation persists, consider switching                    |
|  to an Opening type boundary condition instead.                    |
+--------------------------------------------------------------------+
```

Figure 37: Report from CFX – Solver to suggest replacing outlet boundary condition with an opening

The outlet boundary condition for the simplified model is set to outlet with static pressure of 0 Pa, not opening, because the simplification does not include the draft tube where the backflow occurs, so CFX solver does not report any problems. It is important to remark that the boundary conditions are the same for all four intakes, meaning that the normal speed at the inlet is always 0.5 m/s and the static pressure at the outlet is 0 Pa.

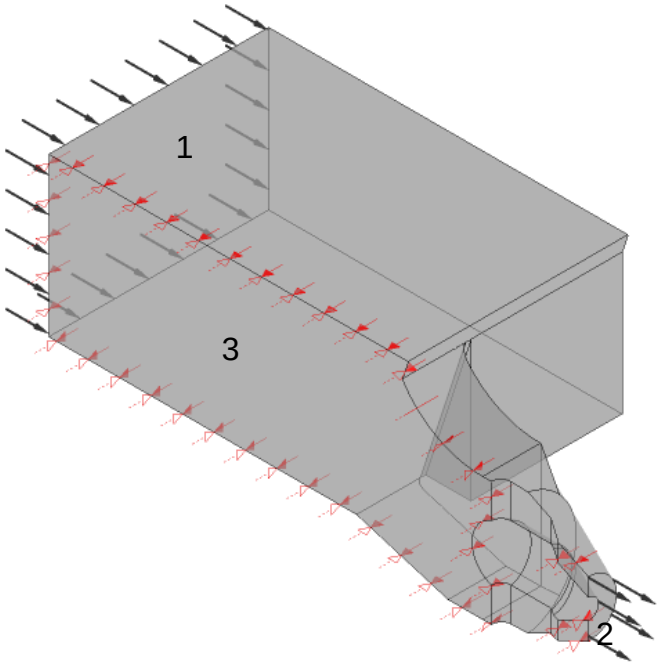

Figure 38: Boundary conditions for the simplified model with intake 1

4.4 CFX-Solver

This chapter describes solution of discretised equation in ANSYS CFX [7]. Solution strategy used in CFX–Solver are described in chapter 3.6., so it will not be explained in this chapter.

A measure of how well the solution is converged can be obtained by plotting the residuals for each equation at the end of each timestep. A reasonably converged solution requires a maximum residual level, in this case it is 0.00001. Typically, the RMS (Root Mean Square) residual will be an order of magnitude lower than this. The RMS residual is obtained by taking all of the residuals throughout the domain, squaring them, taking the mean, and then taking the square root of the mean. This should present an idea of a typical magnitude of the residuals. The Maximum Residuals and/or the RMS Residuals can be displayed in the convergence history plots by selecting a specific monitor in Monitor Setting [3].

Figure 39 describes the convergence of RMS mass and momentum equations for the simplified version of intake 1. The next figure show the maximum values of the same equations. Figure 41 displays the convergence of turbulence

equations, and figure 42 shows the convergence of pressure and velocity at some random points in the fuid domain.

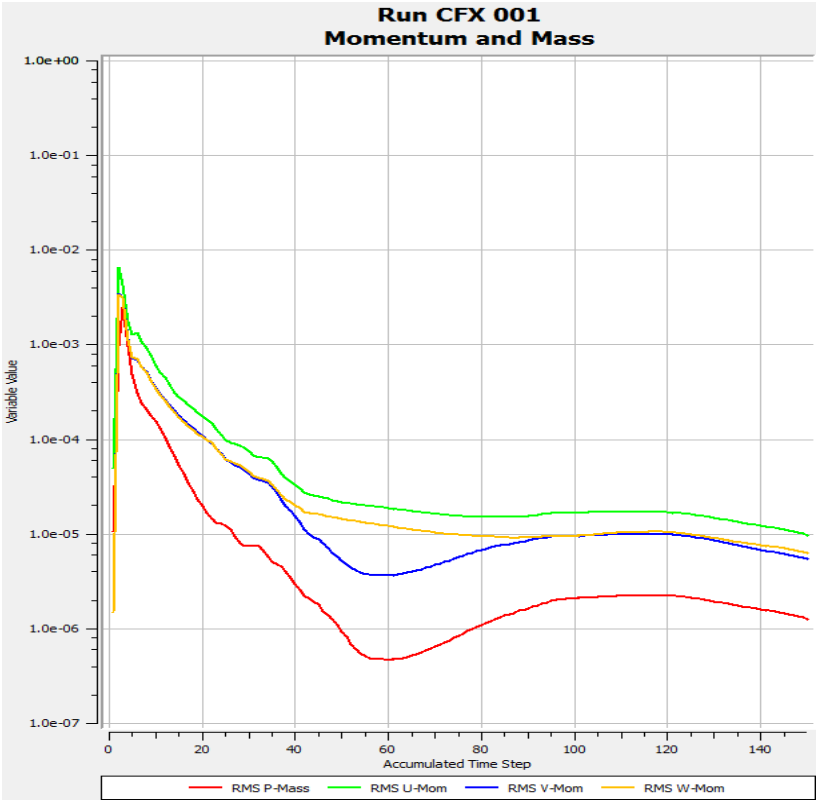

Figure 39: Convergence of RMS values of mass and momentum equations for intake 1

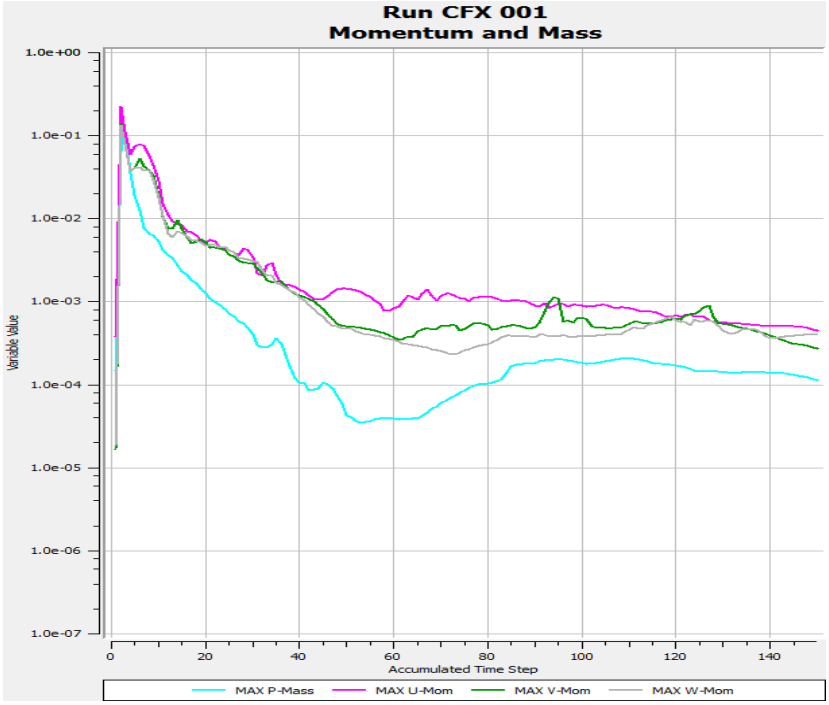

Figure 40: Convergence of maximum values of mass and momentum equations for intake 1

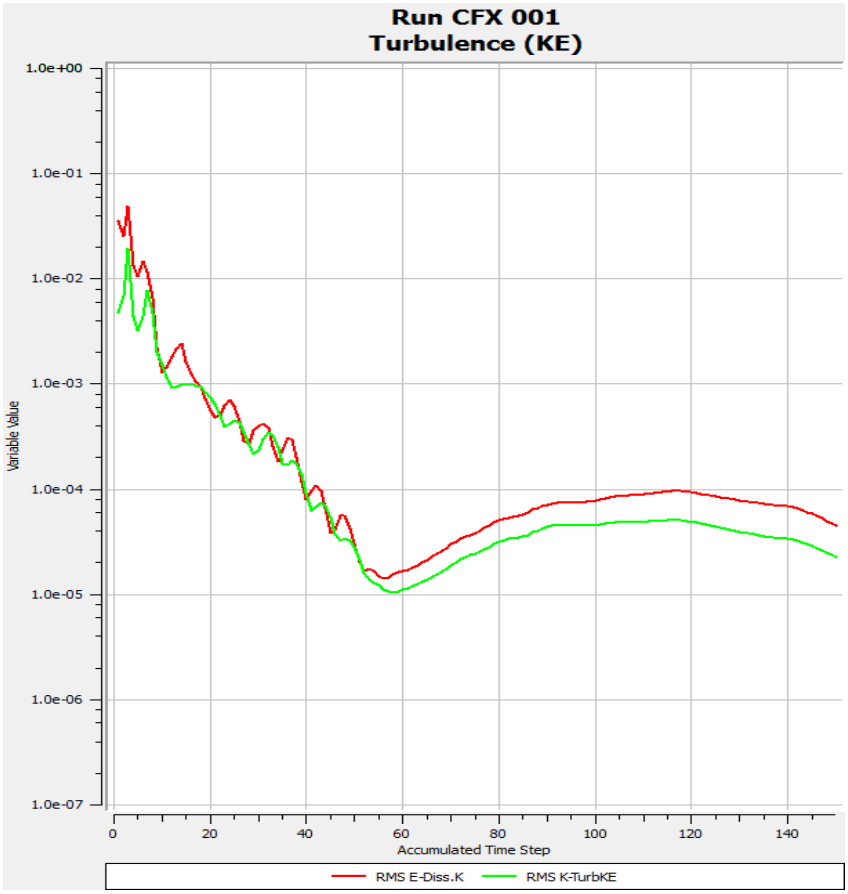

Figure 41: Convergence of RMS values for turbulence equations (k and epsilon) for intake 1

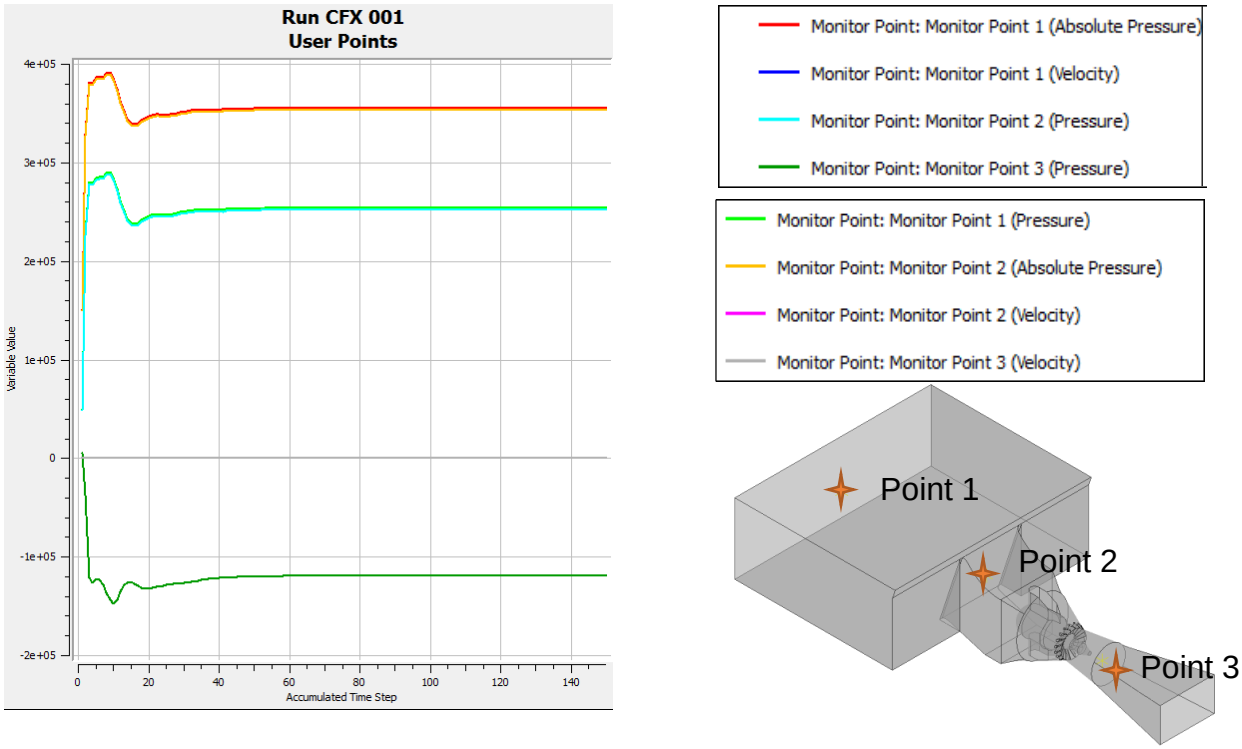

Figure 42: Convergence of velocity and pressure of three monitor points shown on the right side of the figure

5. Results

In this chapter, the post-processing on the bulb turbine model is done. This is the last step of the numerical modelling procedure, where the 3D models, boundary condition etc. from the previous chapter are used to gain results in terms of velocity distributions and pressure losses. All velocity measurements were conducted on a vertical plane (showed in red in figures 43) for the physical as well as for the numerical models for all intakes. The offset of this plane from the bulb is uncertain and not mentioned in the physical study paper, however, for the numerical model this offset is chosen to be 12.85 mm. This particular offset value has proven to give numerical results closest to the physical model results.

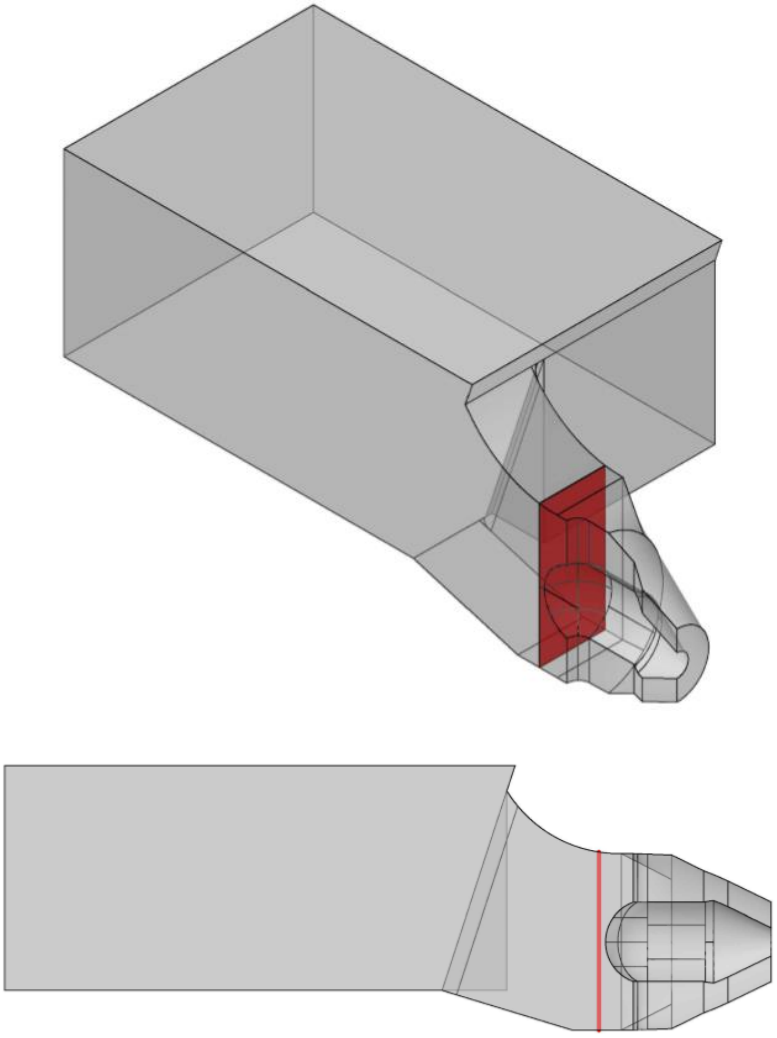

Figure 43: Velocity measurement plane; 3D view (top) and side view (bottom) for intake 1

The numerical results visible in this chapters are made for the simplified versions of the four intakes and compared with the physical model results for the wicket gates opening of 30^0.

The average velocity, $\bar{v}$ was different for each intake; however, flow distribution is not affected by the actual values of velocity [1].

It is obvious from comparing the velocity contours that the intake shape has a significant effect on velocity distribution (see figures 4 – 7 for intake shapes). The velocity distributions for all intakes show the flow stagnation in front of the bulb and flowing around it to the sides. Figure 44 show the streamlines for whole and simplified models.

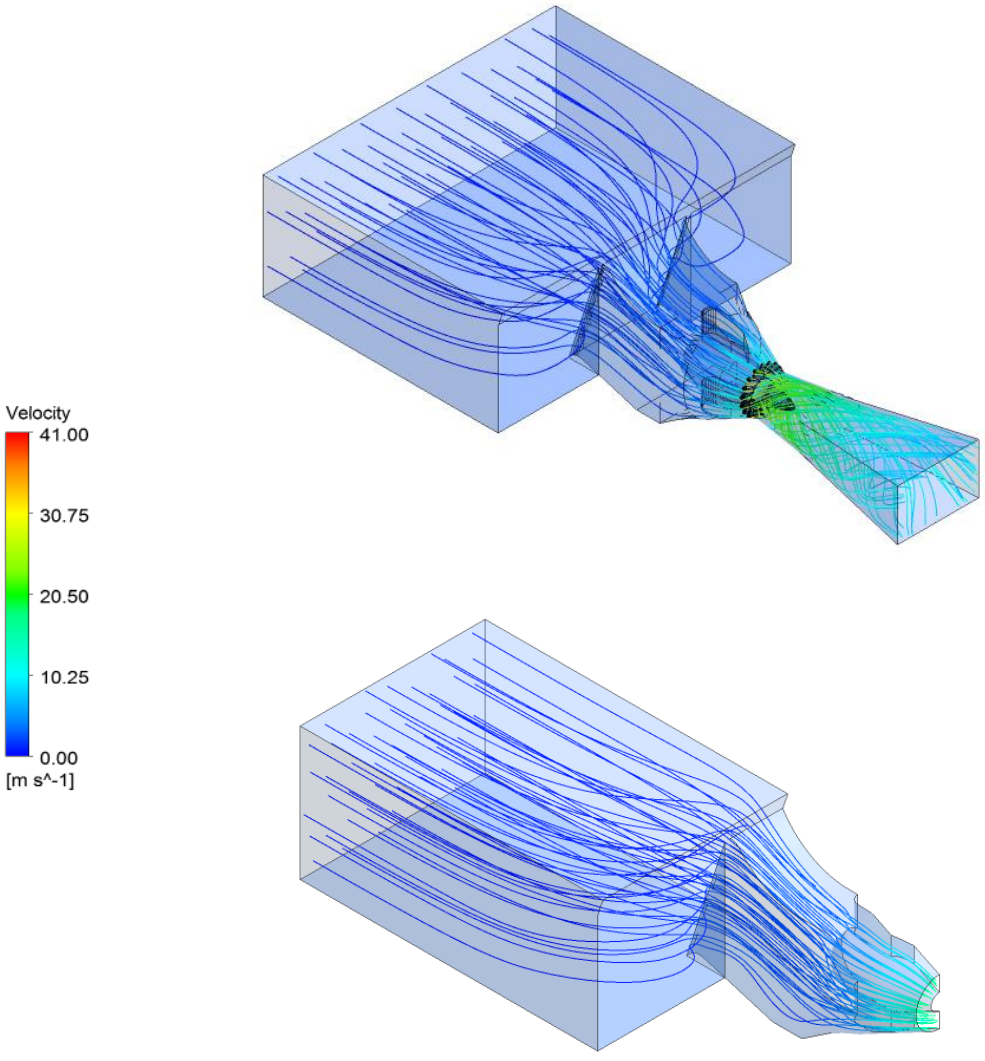

Figure 44: 3D views of streamlines for the whole (top) and simplified model (bottom) for intake 1

5.1 Intake 1

In intake 1, the velocities are high around the top, due to the smooth, bellmouth-type top curve, and low near the bottom, with a steep transition from top to bottom. Figure 45 shows the comparison between the numerical and measured velocity results. The numerical results (left) are gained with ANSYS CFX [7], while the measured results (right) are accessible through the hydraulic study model paper and modified with PYTHON. The velocities are represented with the velocity coefficient $v/\bar{v}$.

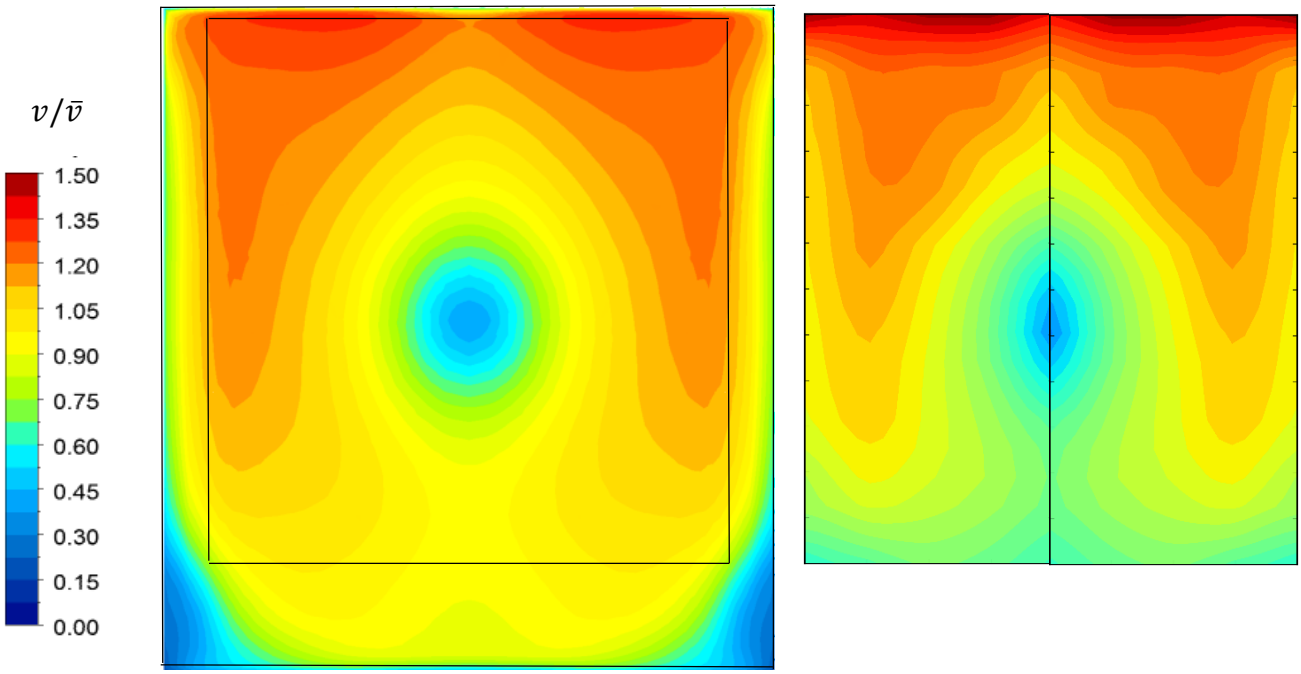

Figure 45: Velocity distribution of the numerical model (left) and physical model (right) for intake 1

Figure 46 show the velocity distribution over the second column (left side of the figure) for the numerical and physical model. The following figures show velocity vectors, velocity distribution over 2 quadrants of the intake and a vertical and horizontal section through the intake model including the stilling chamber.

In the vector distribution, it can be seen how the velocities decrease before the bulb and increase on the side of it. In the horizontal section b–b on the cross section of the bulb and stilling chamber, a slight flow separation is visible.

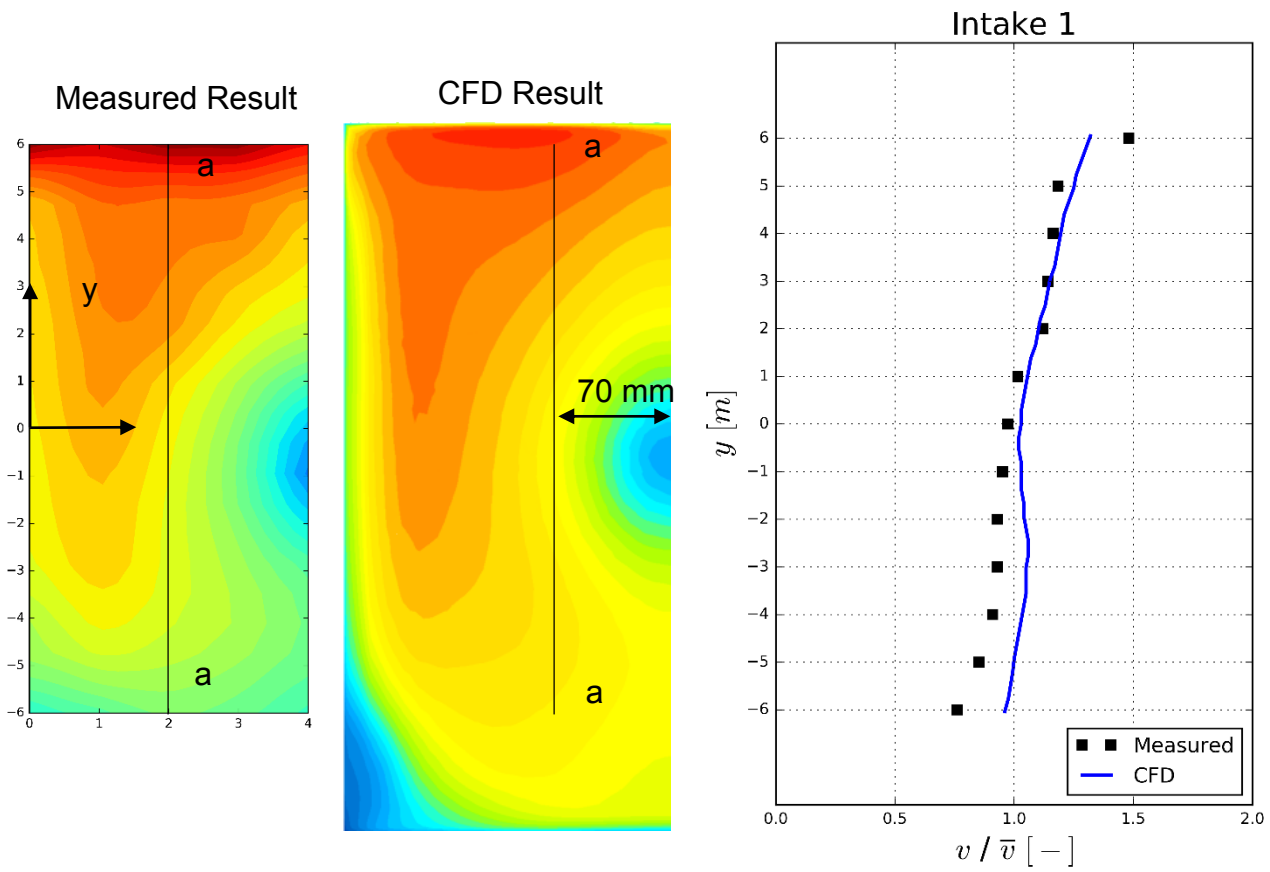

Figure 46: Velocity distribution in line a–a (column 2) for CFD and measured results

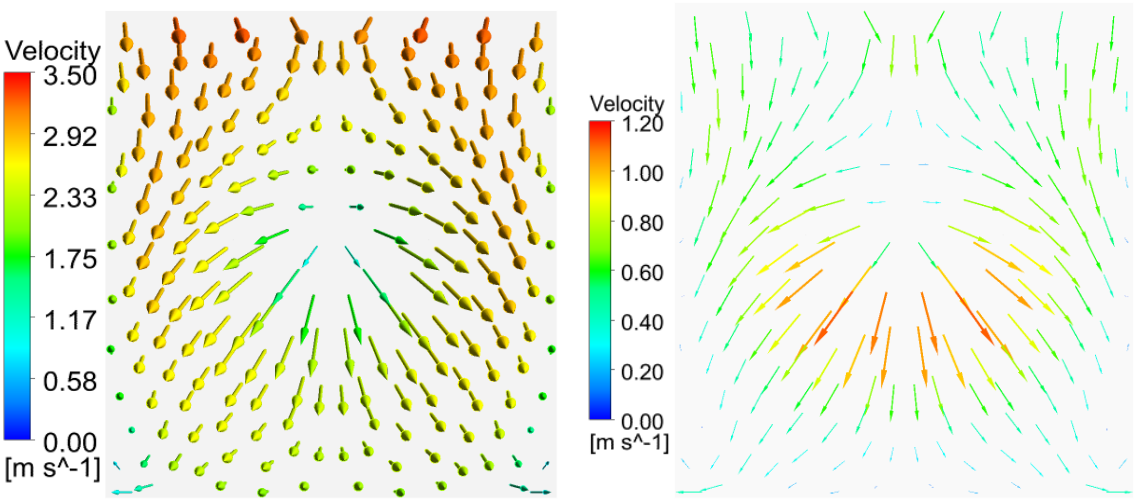

Figure 47: Velocity vector distribution for Intake 1 (left), and tangential projection of the vectors (right)

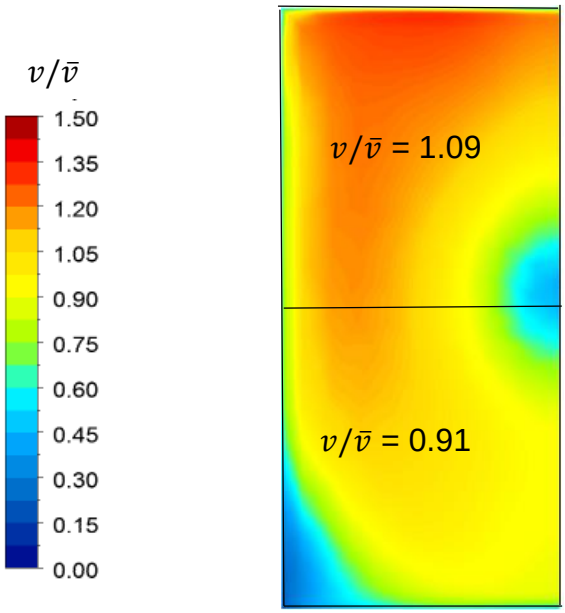

Figure 48: Velocities for two quadrants of intake 1 (the other two are considered to be symmetrical)

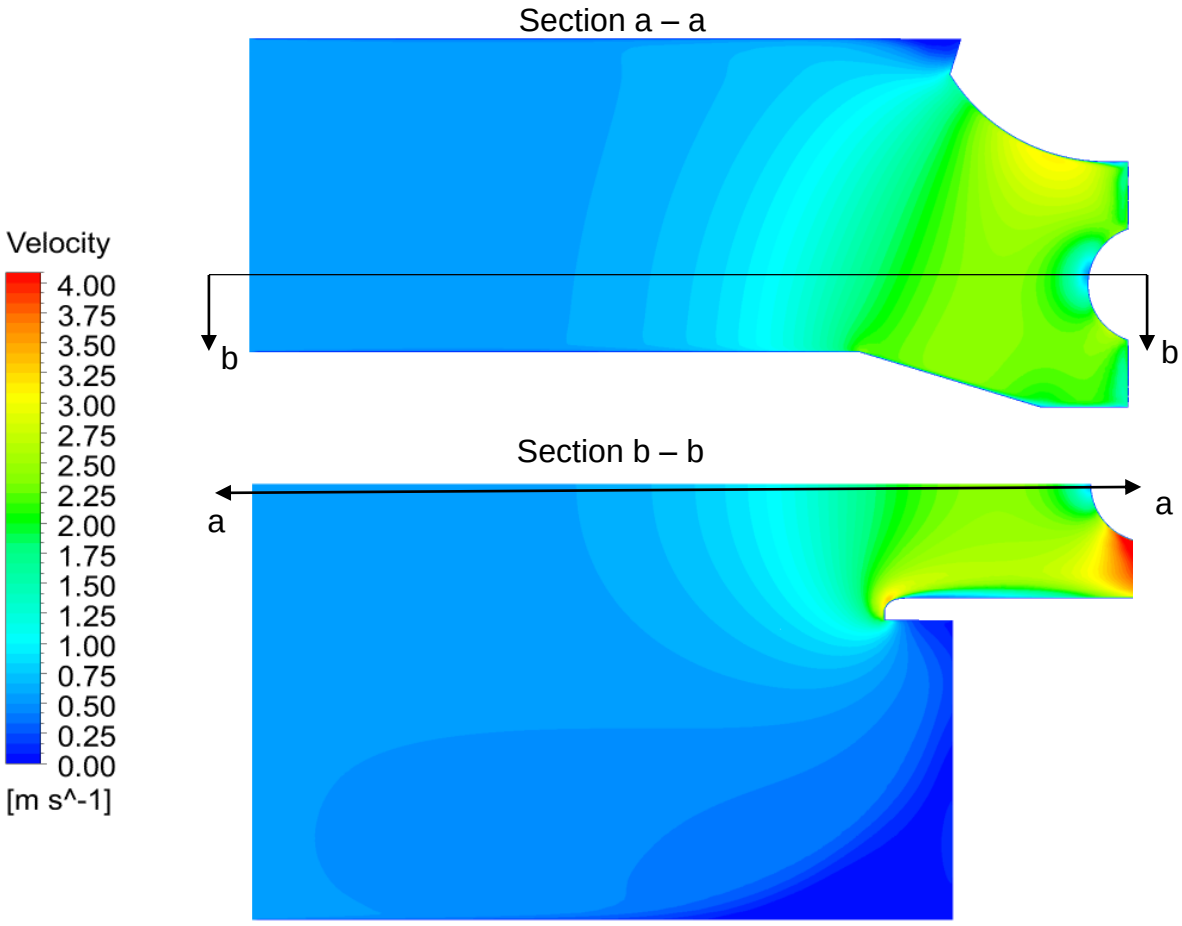

Figure 49: Vertical and horizontal section through intake 1 including the stilling chamber

5.2 Intake 2

In intake 2, the velocities were fairly uniform over the whole profile, and the local velocities did not vary greatly from the average velocity. Figure 50 shows the comparison between the numerical and measured velocity results. The numerical results (left) are gained with ANSYS CFX [7], while the measured results (right) are accessible through the hydraulic study model paper and modified with PYTHON. The velocities are represented with the velocity coefficient $v/\bar{v}$.

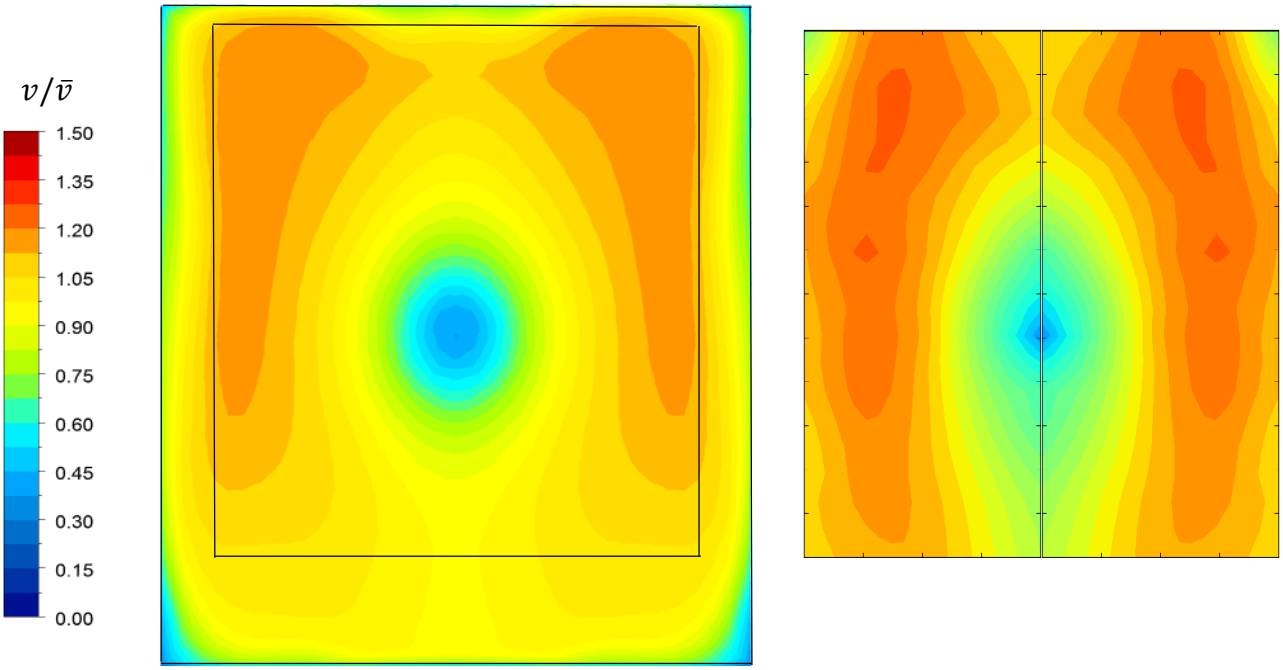

Figure 50: Velocity distribution of the numerical model (left) and physical model (right) for intake 2

Figure 51 show the velocity distribution over the second column (left side of the figure) for the numerical and physical model. The following figures show velocity vectors, velocity distribution over 2 quadrants of the intake and a vertical and horizontal section through the intake model including the stilling chamber.

The vector distribution show that the vectors are directed more central than in intake 1. In the horizontal section b–b of the cross section of the bulb and stilling chamber, a flow separation something bigger than in intake 1 is visible, and in vertical section a–a an slight flow separation is visible.

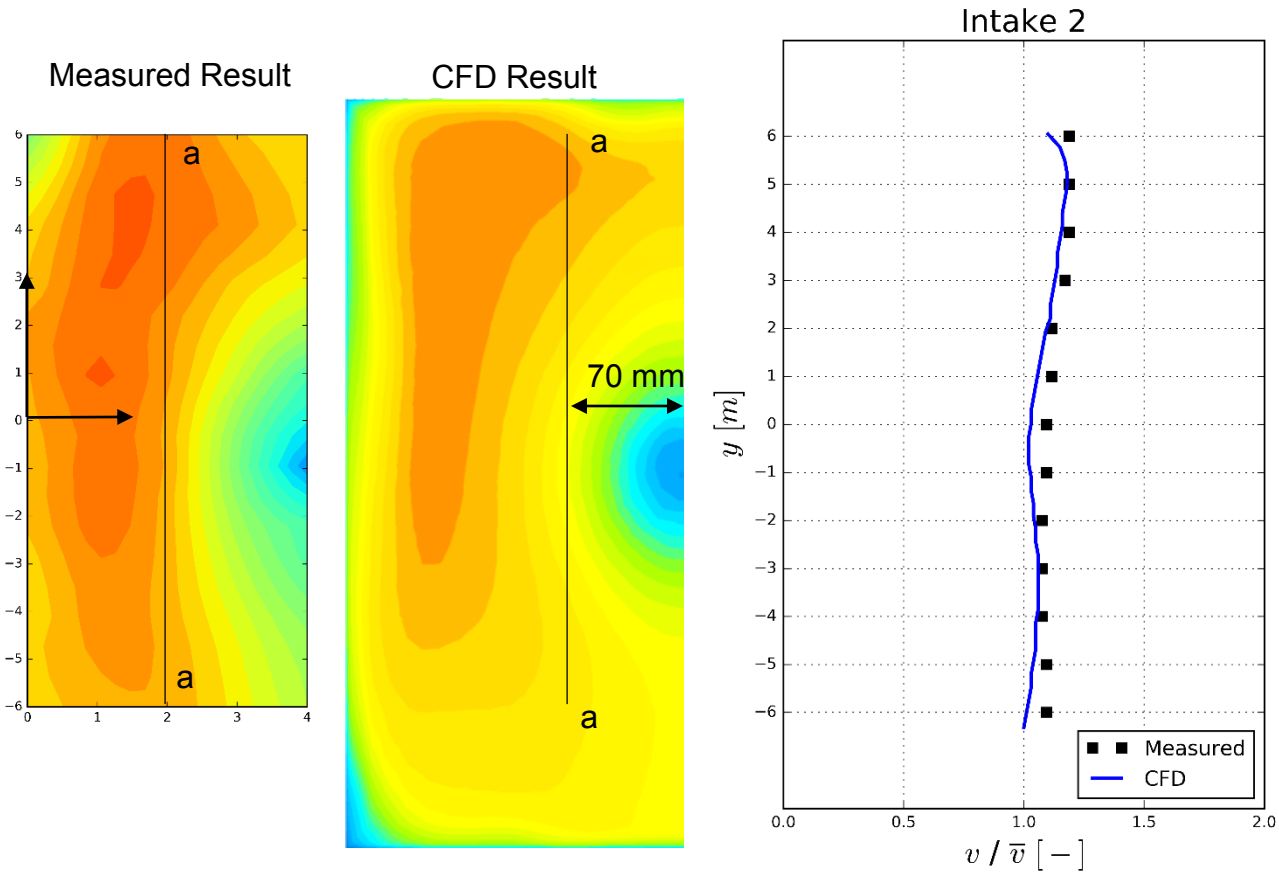

Figure 51: Velocity distribution in line a–a (column 2) for CFD and measured results

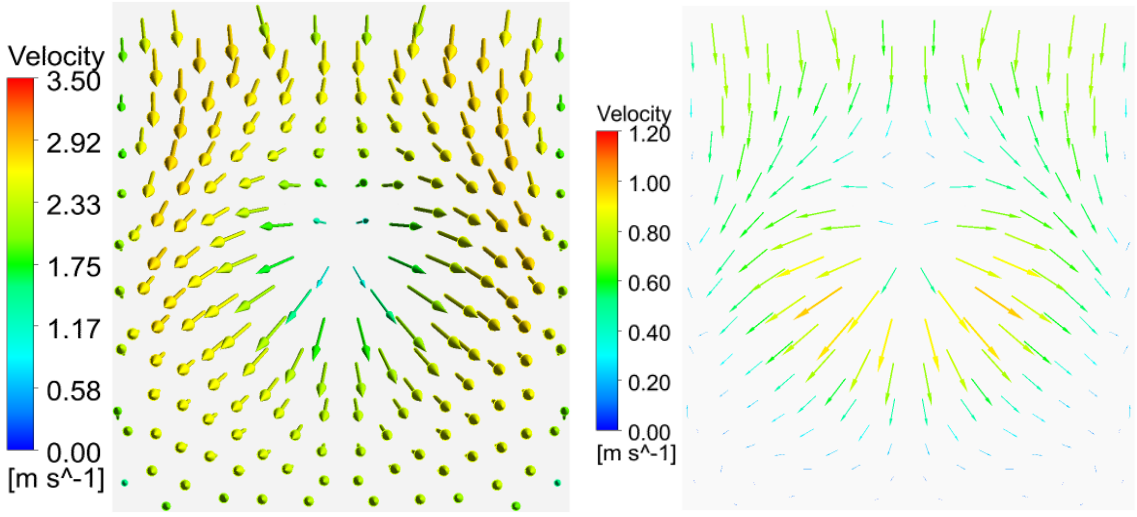

Figure 52: Velocity vector distribution for Intake 2 (left), and tangential projection of the vectors (right)

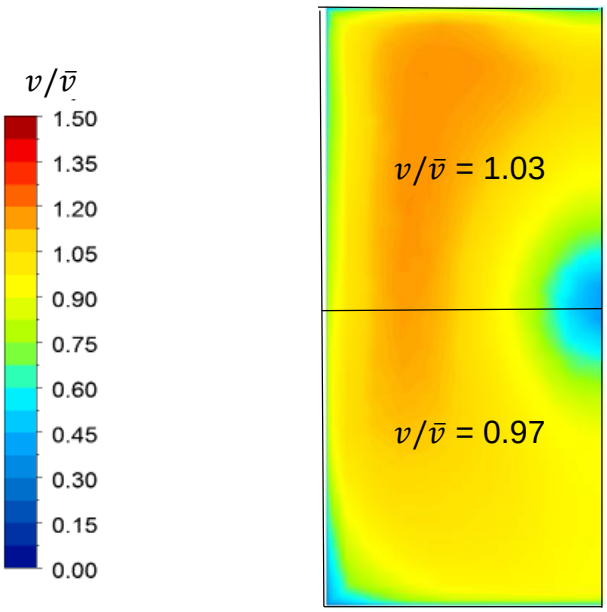

Figure 53: Velocities for two quadrants of intake 2 (the other two are considered to be symmetrical)

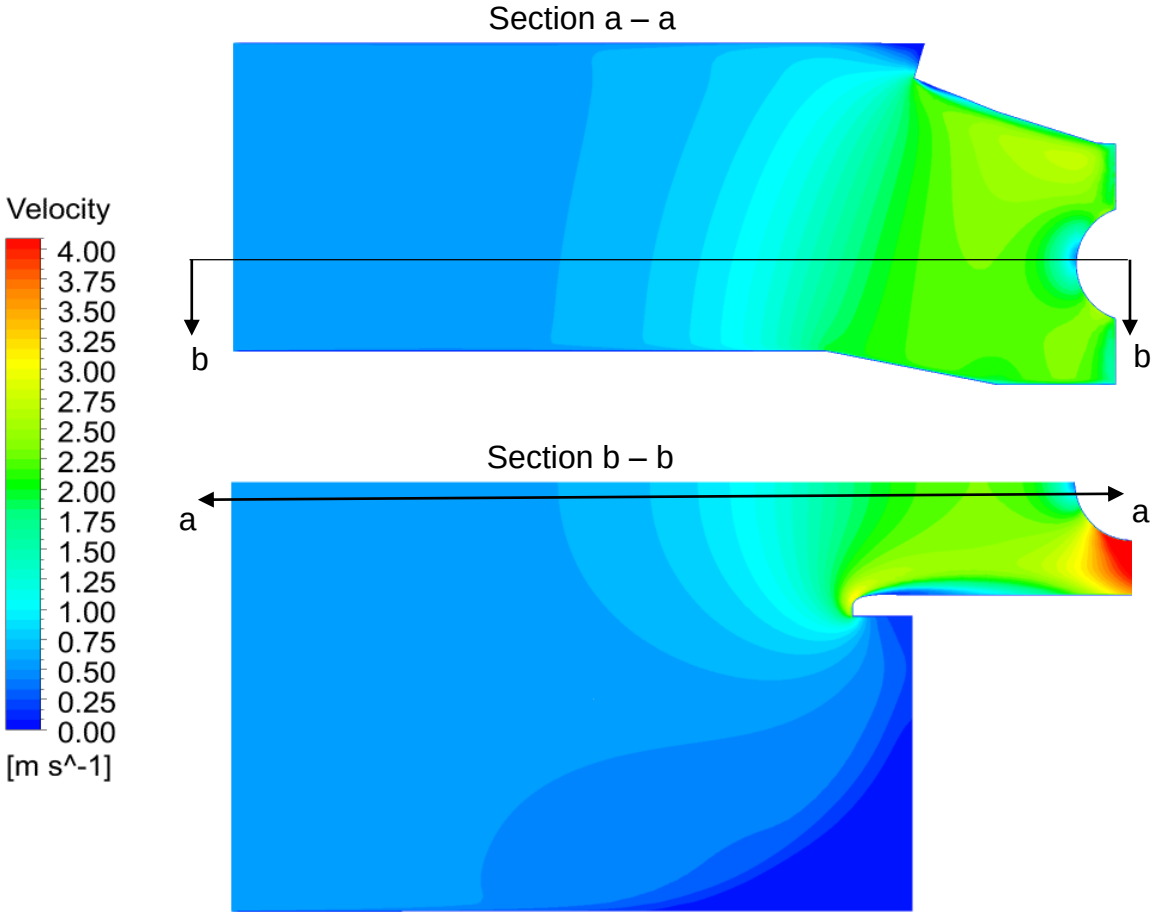

Figure 54: Vertical and horizontal section through intake 2 including the stilling chamber

5.3 Intake 3

Intake 3 has no entrance curves and the corners are squares. The effect of the square corners is visible in the velocity profiles. The velocities are high through the centre and very low at the edges and corners of the intake. Figure 55 shows the comparison between the numerical and measured velocity results. The numerical results (left) are gained with ANSYS CFX [7], while the measured results (right) are accessible through the hydraulic study model paper and modified with PYTHON. The velocities are represented with the velocity coefficient $v/\bar{v}$.

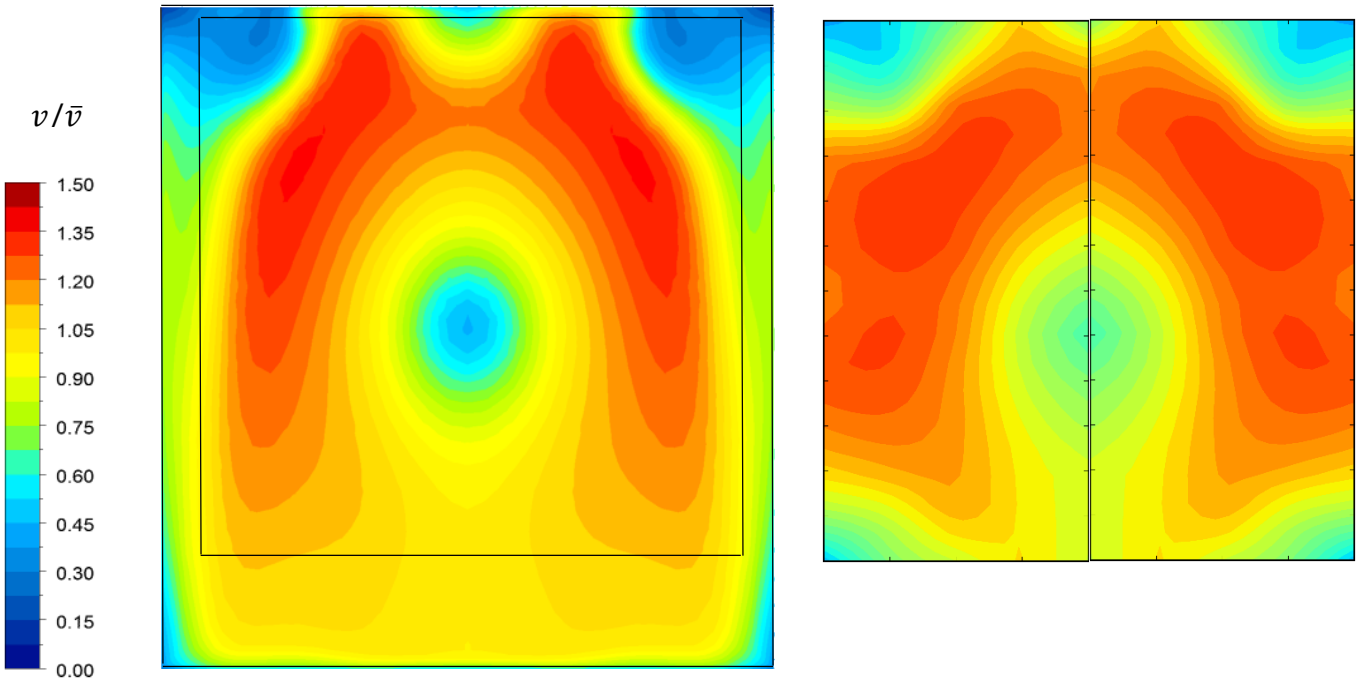

Figure 55: Velocity distribution of the numerical model (left) and physical model (right) for intake 3

Figure 56 show the velocity distribution over the second column (left side of the figure) for the numerical and physical model. The following figures show velocity vectors, velocity distribution over 2 quadrants of the intake and a vertical and horizontal section through the intake model including the stilling chamber.

The vector distribution show rotating flow in the upper corners and different vector angles on the vertical edges. In the horizontal section b–b of the cross section of the bulb and stilling chamber, a great flow separation is visible, and in vertical section a–a another flow separation and flow stagnations are visible.

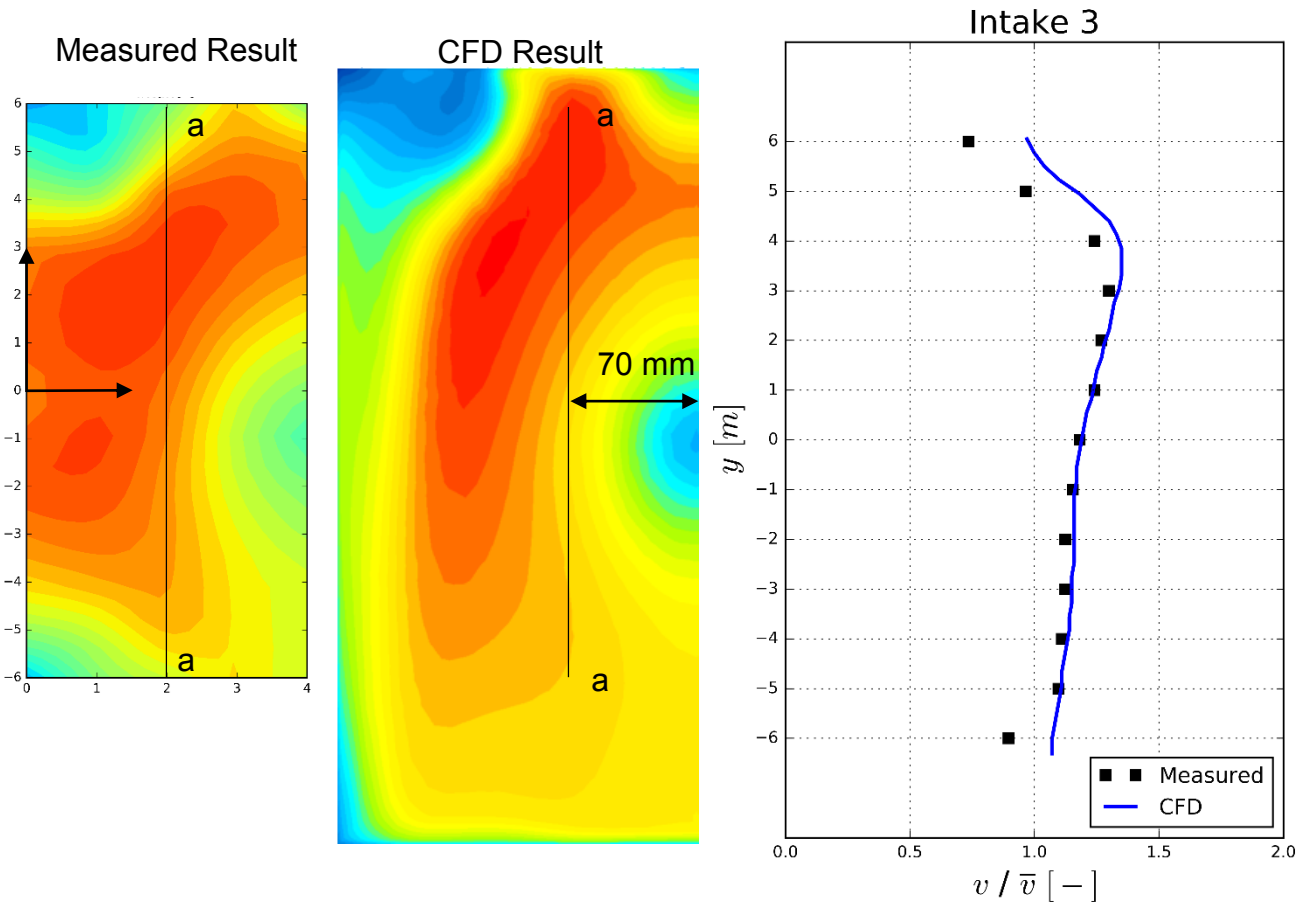

Figure 56: Velocity distribution in line a–a (column 2) for CFD and measured results

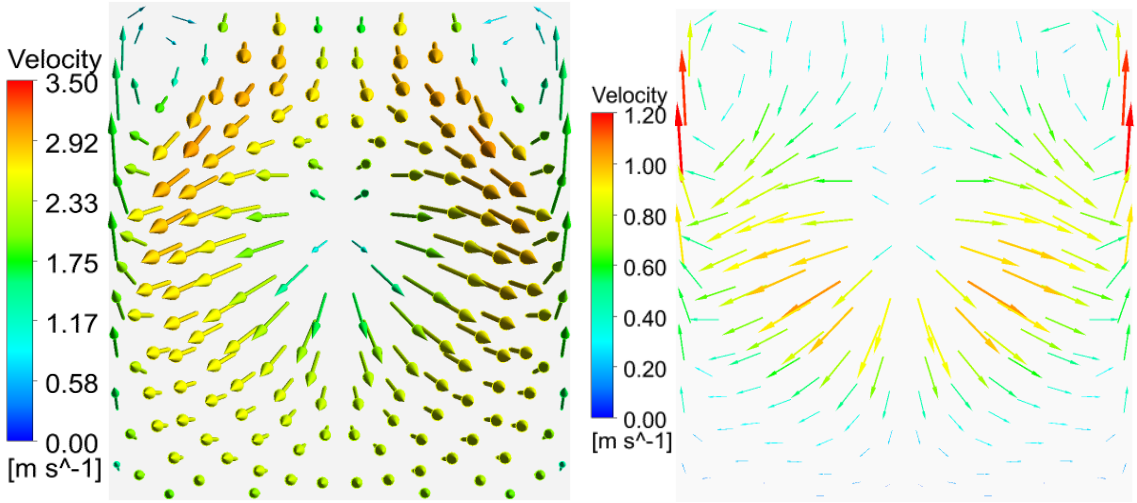

Figure 57: Velocity vector distribution for Intake 3 (left), and tangential projection of the vectors (right)

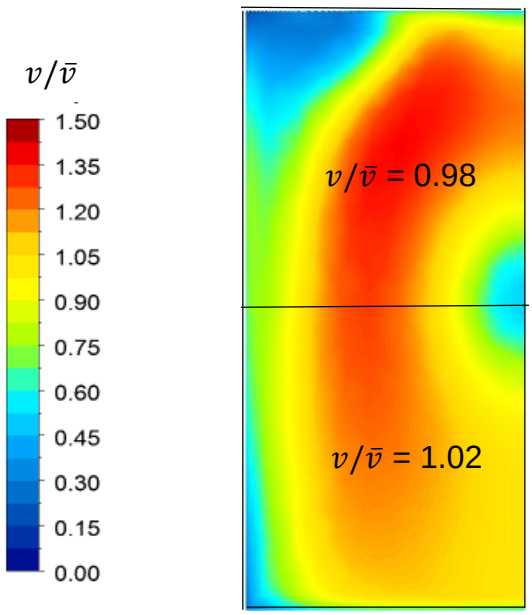

Figure 58: Velocities for two quadrants of intake 3 (the other two are considered to be symmetrical)

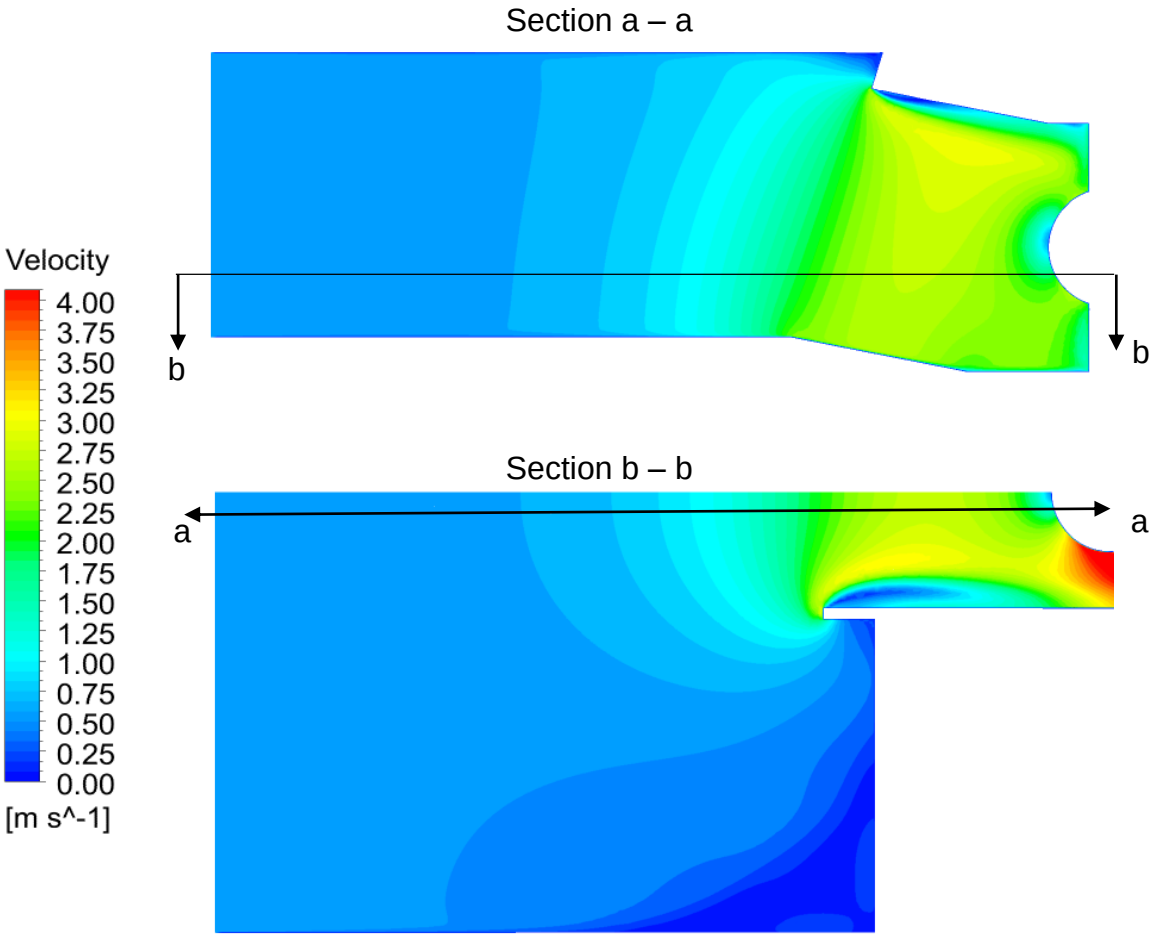

Figure 59: Vertical and horizontal section through intake 3 including the stilling chamber

5.4 Intake 4

Intake 4 has high velocities in the top but otherwise the flow distribution is fairly uniform. This intake did not indicate flow separation as intake 3, nor a steep gradient from top to bottom as intake 1. The overall velocity distribution was the most uniform in intake 4. Figure 60 shows the comparison between the numerical and measured velocity results. The numerical results (left) are gained with ANSYS CFX [7], while the measured results (right) are accessible through the hydraulic study model paper and modified with PYTHON. The velocities are represented with the velocity coefficient $v/\bar{v}$.

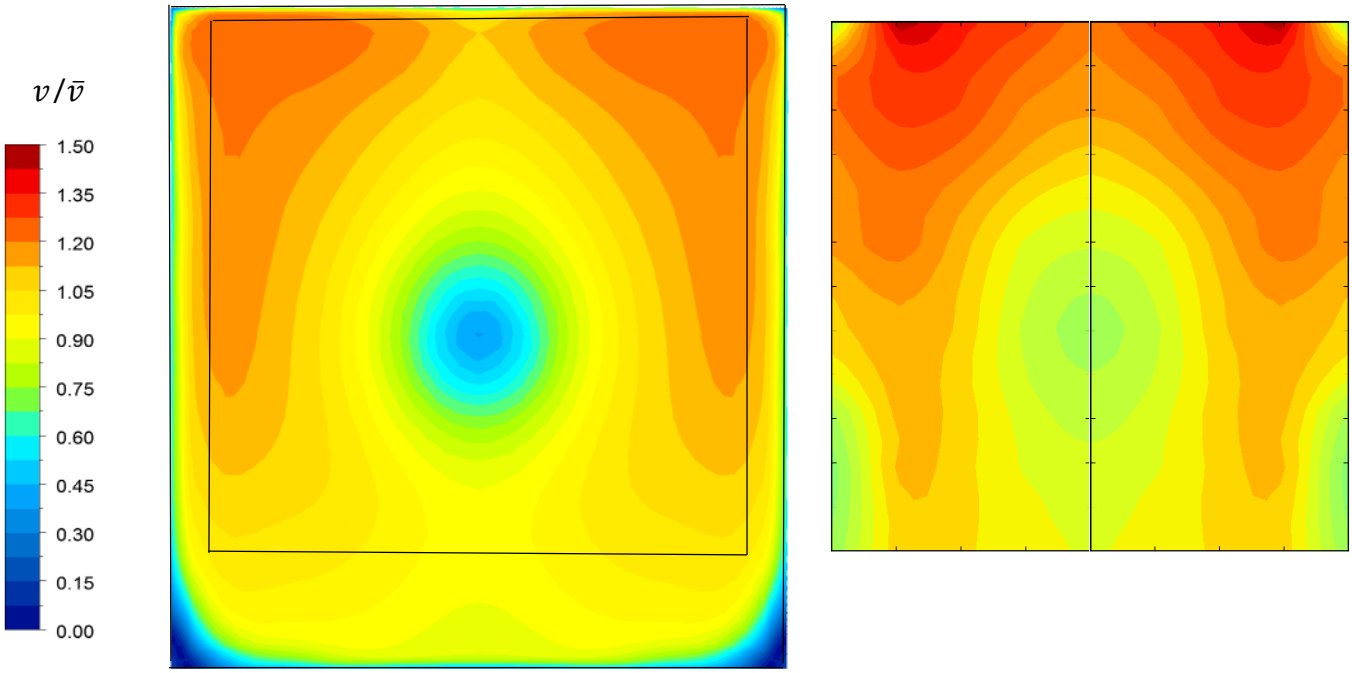

Figure 60: Velocity distribution of the numerical model (left) and physical model (right) for intake 4

Figure 61 show the velocity distribution over the second column (left side of the figure) for the numerical and physical model. The following figures show velocity vectors, velocity distribution over 2 quadrants of the intake and a vertical and horizontal section through the intake model including the stilling chamber.

In the vector distribution, it can be seen how the velocities decrees before the bulb and increase on the side of it. In the horizontal and vertical section of the bulb and stilling chamber, it is visible that intake 4 has almost no flow separation.

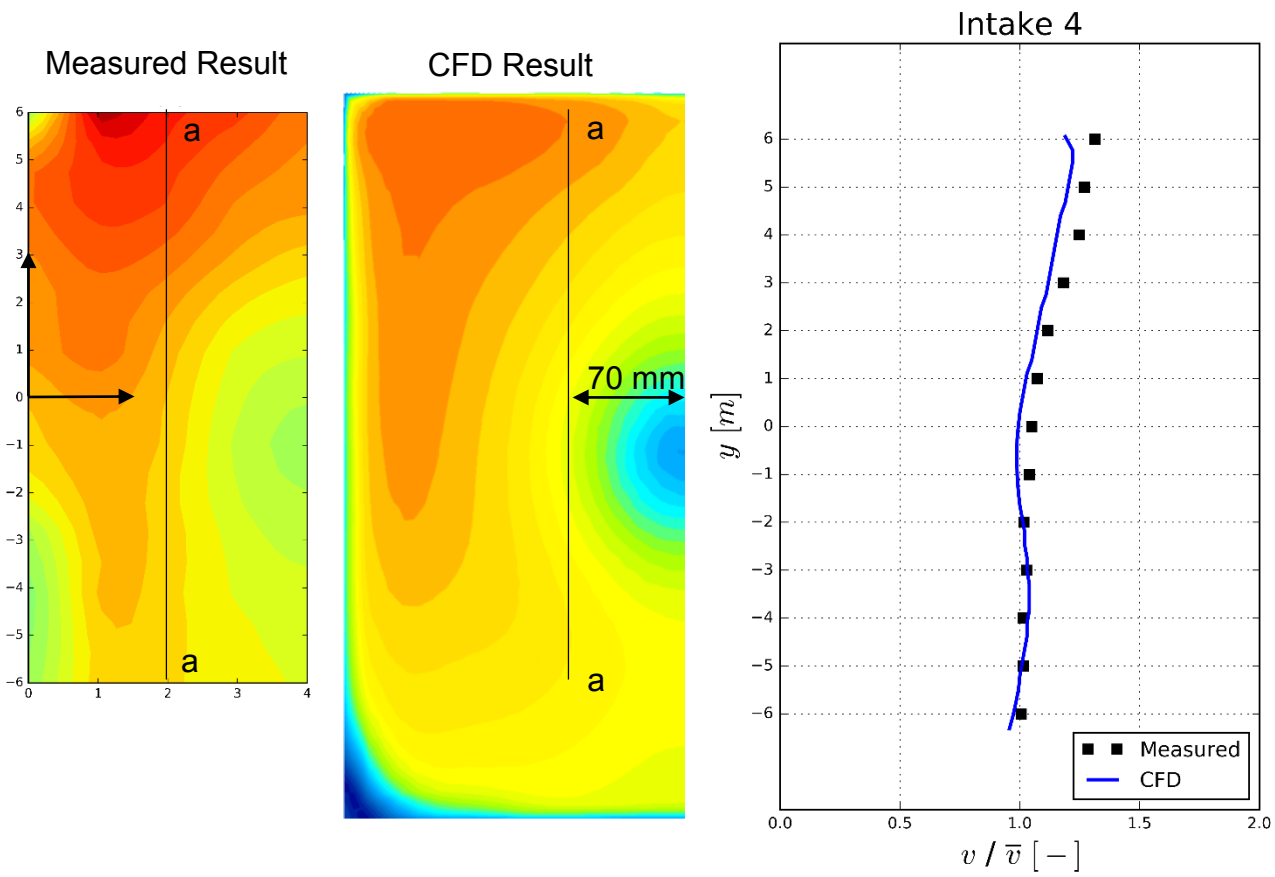

Figure 61: Velocity distribution in line a–a (column 2) for CFD and measured results

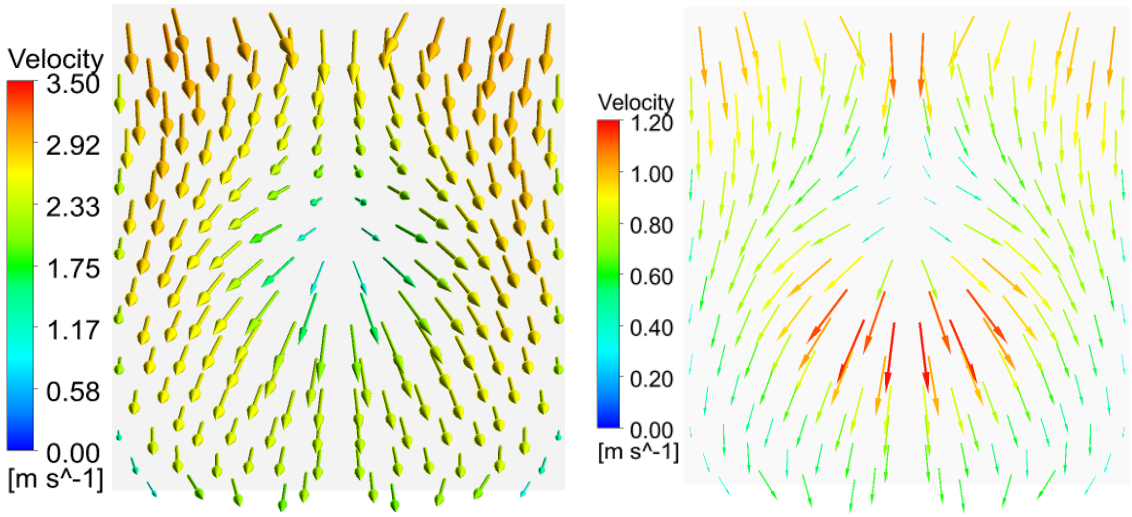

Figure 62: Velocity vector distribution for Intake 4 (left), and tangential projection of the vectors (right)

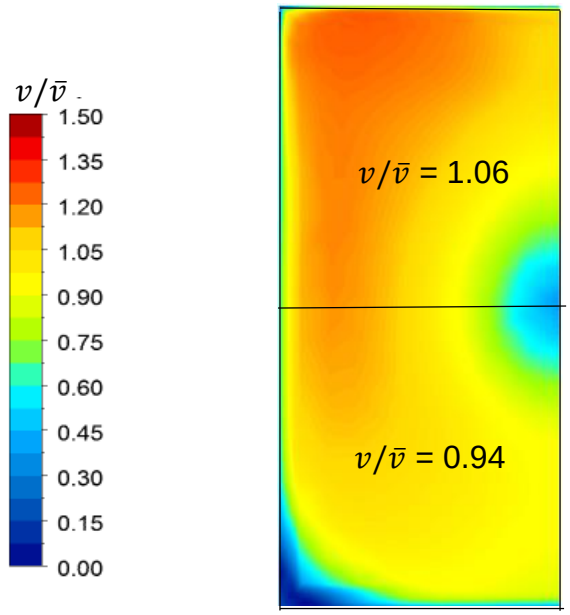

Figure 63: Velocities for two quadrants of intake 4 (the other two are considered to be symmetrical)

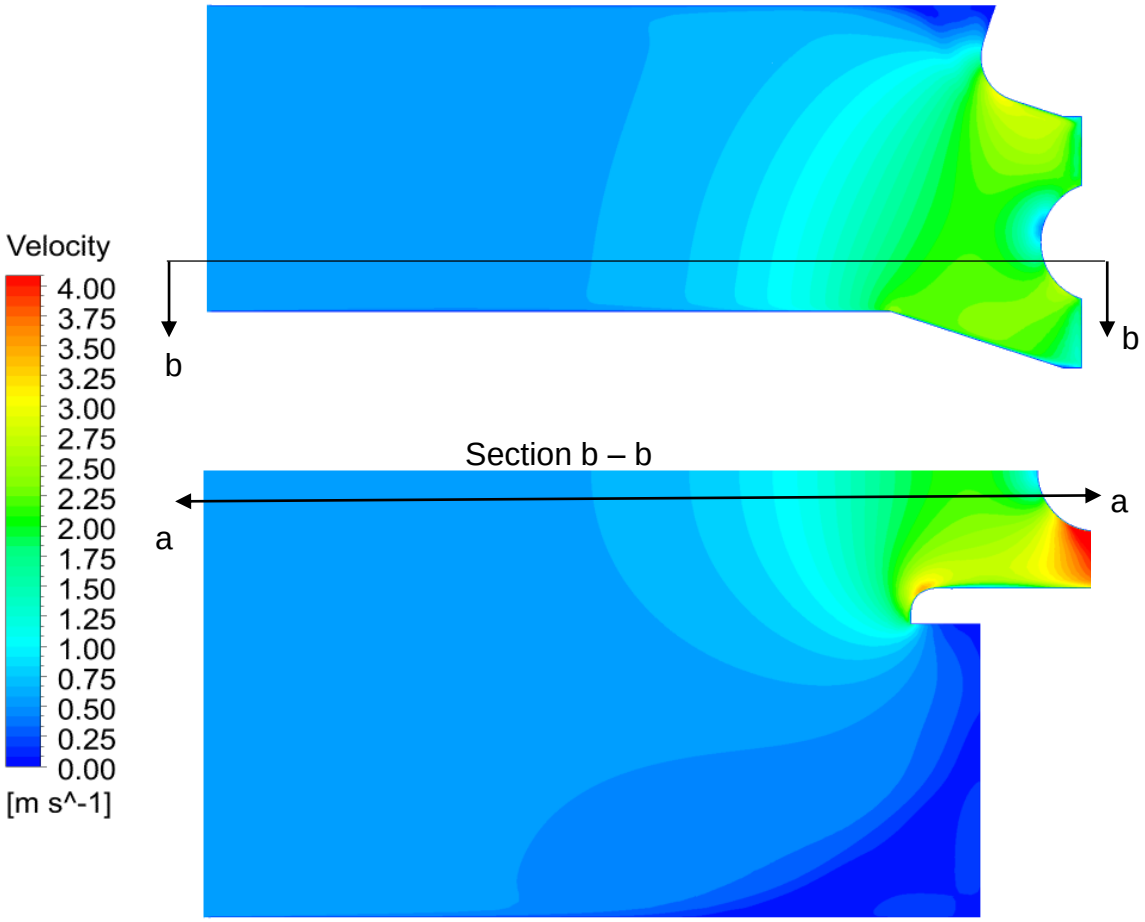

Figure 64: Vertical and horizontal section through intake 4 including the stilling chamber

5.5 Head Losses

It is of great interest to calculate head losses for each intake and to cross-validate them. Friction losses are not included in the loss calculation due to the surface roughness. The only losses calculated in this research are the local losses, which are dependent only on geometry changes in the model. Local losses appear by energy dissipation happening because flow irregularities caused by geometry change. The head losses for each intake model were determined by calculating the difference of total pressure on the inlet and outlet, and dividing this difference with $\rho \cdot g$. This calculation is performed in CFX-Post, the formula for calculation of head losses is inserted under Expressions:

(**areaAve**(*Total Pressure*)@**Inlet** - **areaAve**(*Total Pressure*)@**Outlet**)/(1000[*kg/m^3*]*9.81[*m/s^2*])

The total pressure, p_{tot}, is defined as the pressure that would exist at a point if the fluid was brought instantaneously to rest such that the dynamic energy of the flow converted to pressure without losses. [3]

For incompressible flows, the total pressure is given by Bernoulli's equation:

$$p_{tot} = p_{stat} + \frac{1}{2}\rho(U \cdot U) \tag{5.1}$$

which is the sum of the static and dynamic pressures.

It is also of interest to represent ζ values for each intake, which is a common indicator of the head losses. ζ value is given by equation:

$$\zeta = \frac{\Delta h}{\frac{v^2}{2g}} \tag{5.2}$$

where v is the average velocity at the outlet.

Head losses and ζ values for all intakes are shown in table 3.

Table 3: Head losses and ζ values for all intakes and compared to intake 1

Intake	Δh [m]	$\Delta h_i/\Delta h_1$	ζ_i/ζ_1
1	0.32	1	1
2	0.32	0.98	0.95
3	0.33	1.01	1.22
4	0.28	0.88	0.94

5.6 Velocity Comparison

Velocities for all four intakes are shown in five vertical lines (figure below). Distances of vertical lines a-a, b-b, c-c, d-d and e-e from intake centre are respectively: 0, 40, 80, 120 and 150 mm for all intakes. Velocity distributions for all intakes are represented to have the same centre (from the bulb), because the measurement plane height (figure 43) is not same for all intakes.

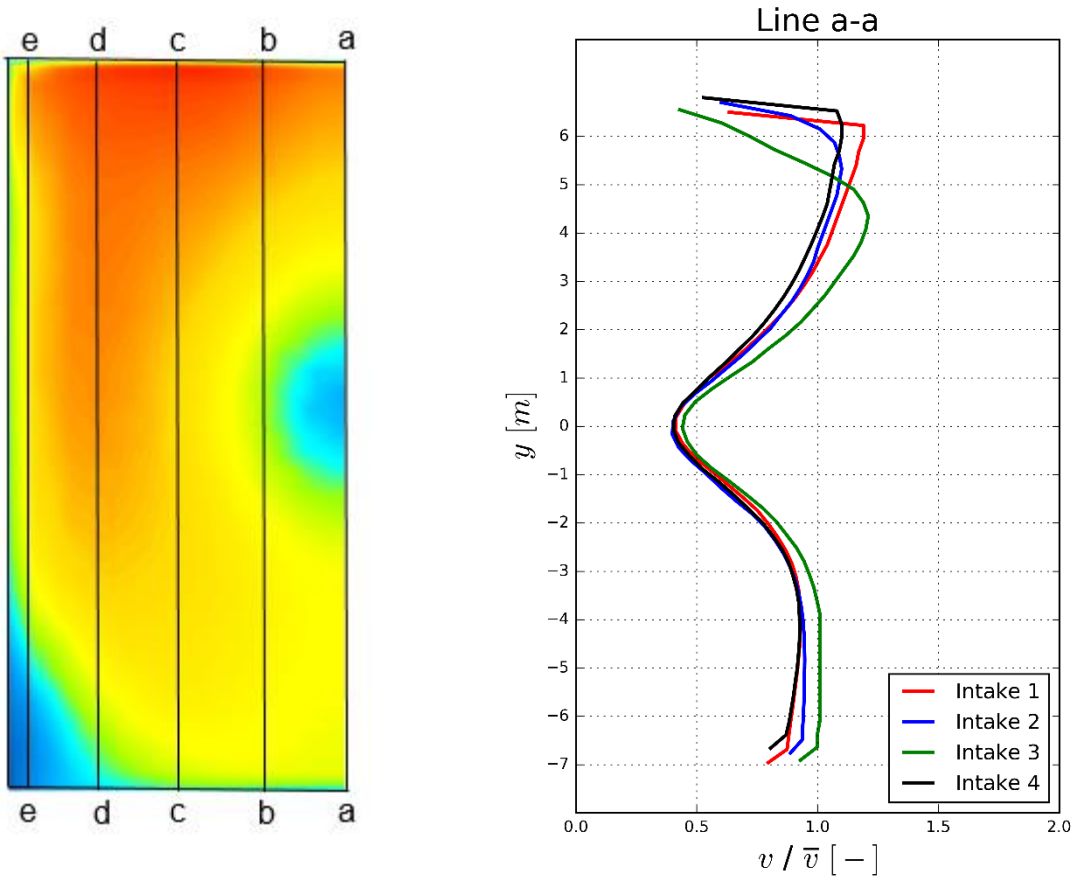

Figure 65: Measurement lines and plane for intake 1 (right) and velocity distribution on line a-a for all intakes

Images of velocity distributions show that intake 3 has lower velocities in the upper region (except for line b-b) than the other intakes. This is due to the square corners and lack of entrance curves of the third intake. However, it is visible in line b-b, c-c and a-a that intake 3 has the highest velocities in the middle and lover region of the measurement domain. Intake 1 and 4 have similar velocity distributions. They have lower velocities in the bottom region of line d-d and e-e, and higher velocities in the upper region of every line, due to the top curvature of both intakes, however intake 4 shows more uniform velocity distribution in comparison whit intake 1. Finally, intake 2 has the most uniform velocity distribution of all intakes, the distributions differ little from line to line.

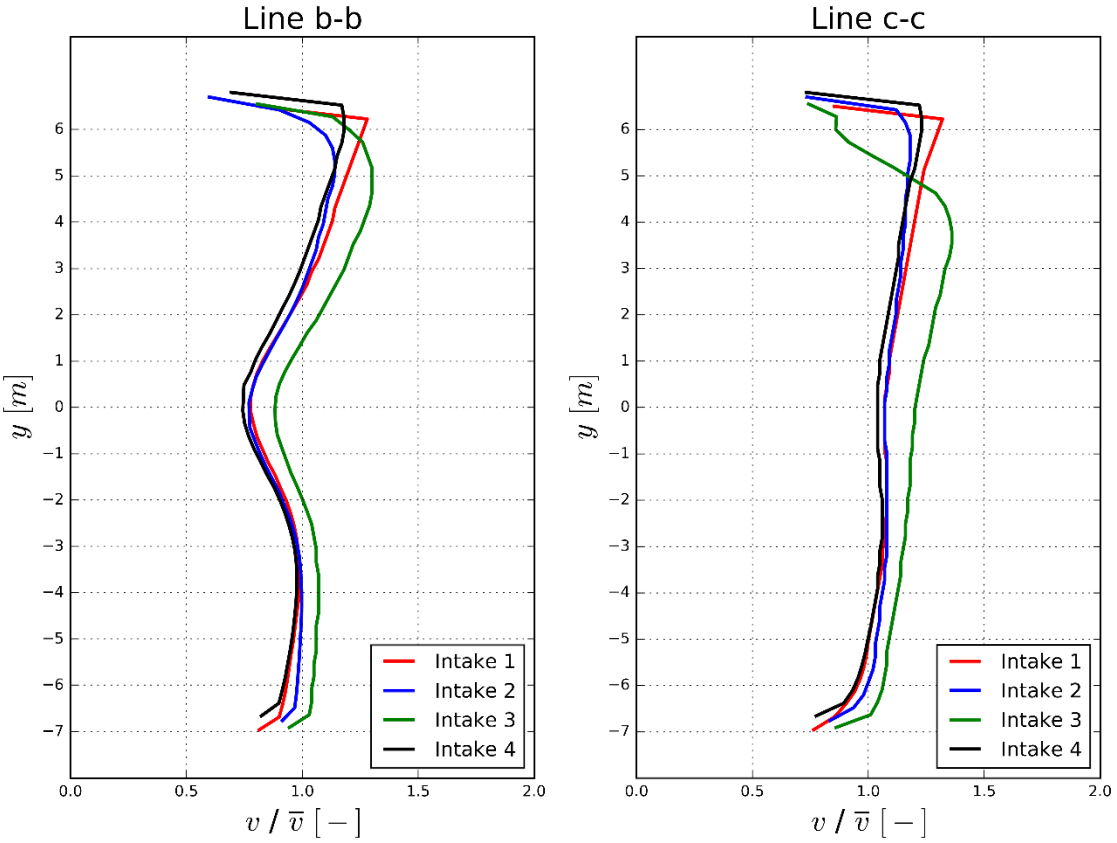

Figure 66: Velocity distribution on line b-b and c-c for all intakes

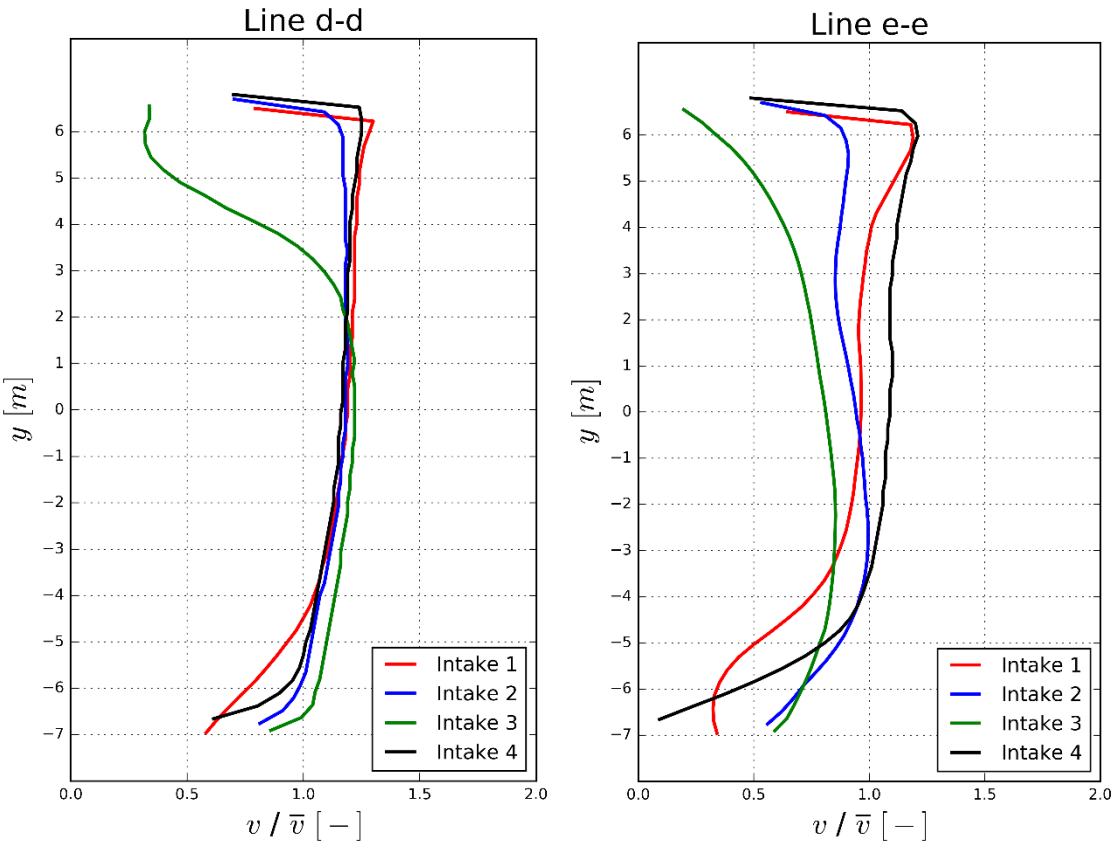

Figure 67: Velocity distribution on line d-d and e-e for all intakes

It is important to represent velocities for all four quadrants for each intake. With the assumption of symmetrical flow distribution, it is necessary to represent only the velocities in the upper and lower quadrants. Velocities for each quadrant are displayed as deviations from the mean velocities of the whole area, visible in table 4.

Table 4: Velocity deviation from mean velocity for all quadrants and intakes

Quadrant	Deviation of quadrant velocities from total mean velocity [%]			
	Intake 1	Intake 2	Intake 3	Intake 4
Upper quadrants	+9	+3	+2	+6
Lower quadrants	-9	-3	-2	-6

6. Conclusion

It has been shown that results obtained with the numerical results for all intakes are similar to the laboratory test results, despite uncertainties regarding the geometry. Differences of the numerical and measured results are insignificant, regardless to the several assumptions included in the geometry of the model and the finite volume method technique used to solve fluid flow equations in this research. RANS equations generate more smeared results compared to realistic turbulent behaviour, however, using more complex turbulent modelling, such as Large Eddy simulation would be significantly more time consuming. Other factors that influence numerical results are numerical errors, which are inevitable in CFD. Furthermore, a mesh sensitivity analysis has been carried out to obtain the results which are independent of the grid size. The objective of this thesis is to investigate application of CFD for preliminary design of the hydro-power intakes. Furthermore, current study showed that it is possible to save computing time by introducing simplification in the numerical model.

The introduction of the model simplification leads to saving in computing time and memory storage. The similarity of velocity distributions of full and simplified model is significant, however, there are some small differences visible. Slightly rotational flow in the velocity distribution of the full model is visible. This is caused by the wicket gates which guides the fluid flow into a rotational motion, thus, the velocities to have a slightly unsymmetrical distribution in the whole model, contrary to the simplified model, where symmetrical flow distribution is assumed. The simplified model results are not identical to the full model result, but they are significantly close to accept the simplification in further research and for other three intake models.

Dimensions of some geometry parameters from the original study were unclear. Tests with different geometry values were made to estimate the unknown parameters. Velocity distributions were compared for every test, and the geometry with results closest to the physical model results were chosen for further investigations.

Results show velocity distributions (figure 68) and head losses for each intake individually. Findings from comparison of the results:

- Intake 1 has a steep velocity gradient from top to bottom due to the bellmouth-type top curve.
- Intakes 2 and 4 have the most uniform velocity distributions.
- Intake 3 has the most erratic velocity distributions due to square corners.
- Finally, intake 4 has the lowest head losses and ζ values. In contrast, intake 3 shows the highest head loss. Furthermore, intakes 1 and 2 showed similar head loss values.

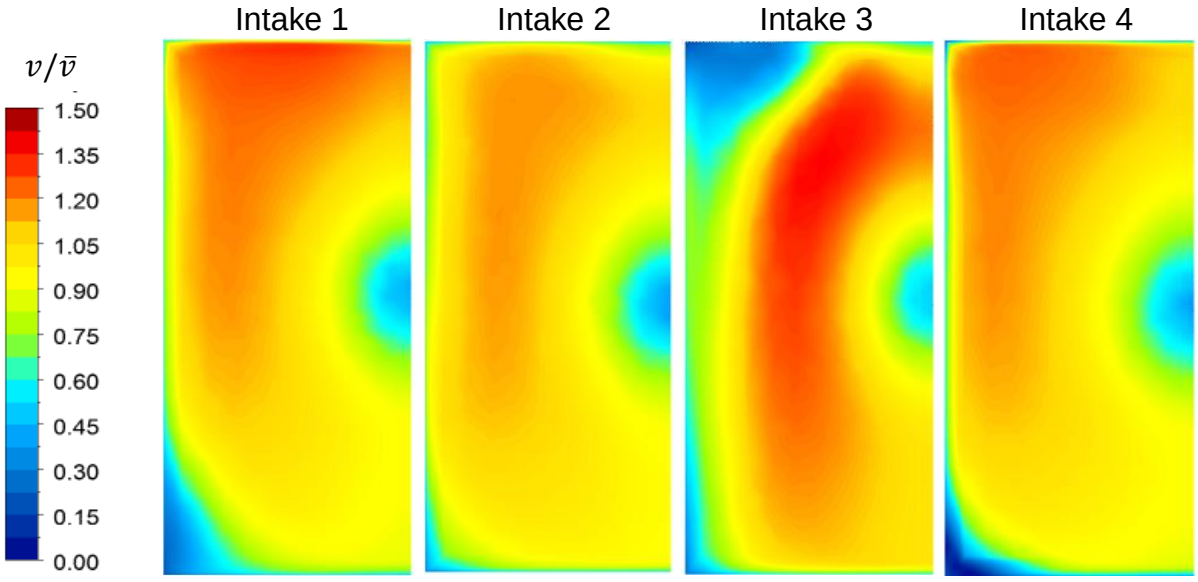

Figure 68: Recall of velocity distributions for all intakes

Through the application of CFD on modelling a series of laboratory tests, it is shown that it is possible to use numerical simulations to approximate complex fluid flow behaviour, which can lead to cost saving in design of approach flow channels and many other hydraulic engineering problems.

References

[1] Clifford A. Pugh, 1983: “Hydraulic Model Studies on Bulb Turbine Intakes”. Bureau of Reclamation, Engineering and Research Center, Denver, Colorado

[2] H. K. Versteeg and W.Malalasekera, 1995: “An Introduction to Computational Fluid Dynamics, The Finite Volume Method”. Longman Scientific & Technical, Burnt Mill, Harlow, England

[3] ANSYS® Academic Research, Release 16.2, Help System, CFX Theory Guide, ANSYS, Inc.

[4] Georgije Hajdin, 2009: “Mehanika Fluida, Dodatna Poglavlja”. Faculty of Civil Engineering, University of Beograd

[5] Barth, T.J., and Jesperson, D.C, 1989: “The Design and Application of Upwind Schemes on Unstructured Meshes”, AIAA Paper 89-0366.

[6] Clifford A. Pugh, 1981: “Intakes and Outtakes for Low-Head Hydropower”. Bureau of Reclamation, Engineering and Research Center, Denver, Colorado

[7] ANSYS® Academic Research, Release 16.2

[8] Autodesk AutoCAD Mechanical 2015, Autodesk®, Inc.

[9] VERBUND Hydropower GmbH: http://www.verbund.com/pp/en/run-of-river-power-plant/melk

Table of Figures

Table of Tables

Abbreviations

3D	Three Dimensional
CFD	Computational Fluid Dynamics
FVM	Finite Volume Method
FEM	Finite Element Method
FDM	Finite Difference Method
PDE	Partial Differential Equations
N-S	Navier-Stokes
CV	Control Volume
RANS	Reynolds Averaged Navier-Stokes equations
LES	Large Eddy Simulations
RSM	Reynolds Stress equation Model
ASM	Algebraic Stress equation Model
MG	Multigrid
ILU	Incomplete Lower Upper

Appendix A – FVM for Convection-Diffusion Problems

The methodology of the FVM will be shown on convection-diffusion transport of a general fluid flow variable ∅. Pure diffusion does not occur in problems contained in this thesis, but it is necessary to understand pure diffusion first in order to solve convection-diffusion problems. For further development of this problem, it is necessary to introduce the general transport equations in differential and integral forms.

If we introduce a general variable ∅, the conservative form of steady state incompressible fluid flow equations can be written in following form:

$$\mathrm{div}(\emptyset \mathrm{u}) = \mathrm{div}\left(\frac{G}{\rho}\ \mathrm{grad}\ \emptyset\right) + S_{\emptyset} \tag{A.1}$$

The equation (A.1) is known as the steady state transport equation for property ∅. It describes the various transport processes: convective term on the left hand side and the diffusive term (G = diffusion coefficient) and the source term on the right hand side. Integration of this equation over a three-dimensional control volume (CV), and applying Gauss divergence theorem gives:

$$\int_A n(\emptyset \mathrm{u})\mathrm{dA} = \int_A n\left(\frac{G}{\rho}\ \mathrm{grad}\ \emptyset\right)\mathrm{dA} + \int_{CV} S_{\emptyset}\ \mathrm{dV} \tag{A.2}$$

In words we have:

Net rate of decrease of ∅ due to convection across the boundaries	=	Rate of increse of ∅due to diffusion across the boundaries	+	Net rate of creation of ∅

The simplest transport process of all is pure diffusion in steady state. The governing equation of steady diffusion ca be derived from the general transport equation for property ∅ (A.1) by deleting the convective terms. This gives:

$$\mathrm{div}\left(\frac{G}{\rho}\ \mathrm{grad}\ \emptyset\right) + S_{\emptyset} = 0 \qquad \text{(A.3)}$$

With the control volume integration, which forms the key step of the FVM that distinguishes it from all other CFD techniques, the above equation can be written as:

$$\int_{CV} div\left(\frac{G}{\rho}\ \mathrm{grad}\ \emptyset\right)\mathrm{dV} + \int_{CV} S_{\emptyset}\ dV = \int_{A} n\left(\frac{G}{\rho}\ \mathrm{grad}\ \emptyset\right)\mathrm{dA}\ +$$

$$\int_{CV} S_{\emptyset}\ \mathrm{dV} = 0 \qquad \text{(A.4)}$$

One-dimensional steady state diffusion of a property ∅ is governed by:

$\frac{d}{dx}(G\ \frac{d\emptyset}{dx})$ + S = 0; where G is the diffusion coefficient and S is the source term. Boundary values of ∅ at points A and B are prescribed.

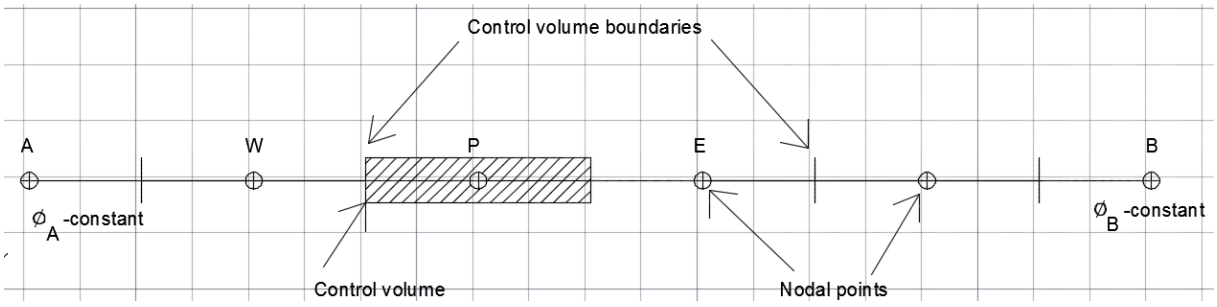

Figure: Solution domain for one dimensional steady state diffusion

(1) Grid generation

The first step in the FVM is to divide the domain into discrete control volumes. A number of nodal points will be placed between A and B. The boundaries (or faces) of control volumes are positioned mid-way between adjacent nodes, so each node is surrounded by a control volume or cell. Control volumes near the domain

edges are usually set in such a way that the physical boundaries coincide with the control volume boundaries. Figure below shows the control volume.

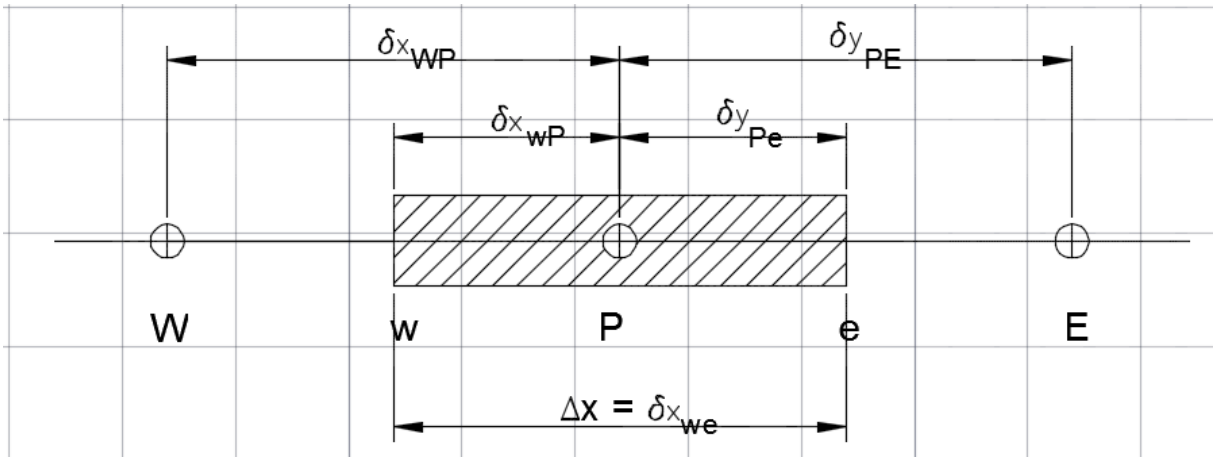

Figure Control volume for solving one dimensional steady state diffusion

(2) Discretization

The key step of the FVM is the integration of the governing equation(s) over a control volume which gives a discretized equation of the nodal point P. For the control volume defined above this gives:

$$\int_{\Delta V} \frac{d}{dx}\left(\mathrm{G}\,\frac{d\emptyset}{dx}\right)\mathrm{dV} + \int_{\Delta V} S\,dV = (\mathrm{GA}\,\frac{d\emptyset}{dx})_e - (\mathrm{GA}\,\frac{d\emptyset}{dx})_w + \bar{S}\Delta\mathrm{V} = 0 \qquad \text{(A.5)}$$

This upper equation states that diffusive flux of ∅ leaving the east face minus the diffusive flux of ∅ entering the west face is equal to the generation of ∅. The equation (A.5) represent a balance equation for ∅ over the control volume.

Linear approximation is the simplest way of calculating interface values and gradients of the discretized equations. In a uniform grid linearly interpolated values for G_e and G_w are given by:

$$G_w = \frac{(G_W + G_P)}{2} \quad ; \qquad G_e = \frac{(G_P + G_E)}{2} \qquad \text{(A.6)}$$

And the diffusive flux terms are evaluated as:

$$(GA\frac{d\emptyset}{dx})_e = \mathrm{G}_e \cdot A_e(\frac{\emptyset_E - \emptyset_P}{\delta x_{PE}}); (GA\frac{d\emptyset}{dx})_w = \mathrm{G}_w \cdot A_w(\frac{\emptyset_P - W}{\delta x_{WP}}) \quad \text{(A.7)}$$

In practical situations, the source term S may be a function of variables, in which case the FVM approximates the source term by means of a linear form:

$$\bar{S}_{\Delta V} = S_u + S_P \emptyset_P \quad \text{(A.8)}$$

By identifying the coefficients $\emptyset_W$ and $\emptyset_E$ as a_W and a_E and the coefficient $\emptyset_P$ as a_P, the steady diffusion equation can be written as:

$$a_P \emptyset_P = a_W \emptyset_W + a_E \emptyset_E + S_u \quad \text{(A.9)}$$

Where:

a_W	a_E	a_P
$\frac{G_w}{\delta x_{WP}} A_w$	$\frac{G_e}{\delta x_{PE}} A_e$	$a_W - a_E - S_P$

The two equations (A.8) and (A.9) represent the discretized form of the equation (A.3). This type of discretized equation is central to the FVM.

(3) Solution of equations

Discretized equations of the form (A.9) must be set up at each of the nodal points in order to solve a problem. Boundary conditions are considered by modifying the general discretized equation (A.9) for control volumes that are adjacent to the domain boundaries. The resulting system of linear algebraic equations is then solved to obtain the distribution of the property ∅ at al nodal points. The matrix solution of the discretized equations is described in the chapter 3.6.

The methodology used in deriving discretized equations in one dimensional case can be easy extended to two- or three-dimensional problems. For instance, steady state diffusion in a three dimensional situation is governed by:

$$\frac{\partial}{\partial x}\left(\mathrm{G}\ \frac{d\emptyset}{dx}\right) + \frac{\partial}{\partial y}\left(\mathrm{G}\ \frac{d\emptyset}{dy}\right) + \frac{\partial}{\partial z}\left(\mathrm{G}\ \frac{d\emptyset}{dz}\right) + S = 0 \quad \text{(A.10)}$$

Now a three-dimensional grid is used for subdivision of the domain. A typical control volume is shown in the figure below.

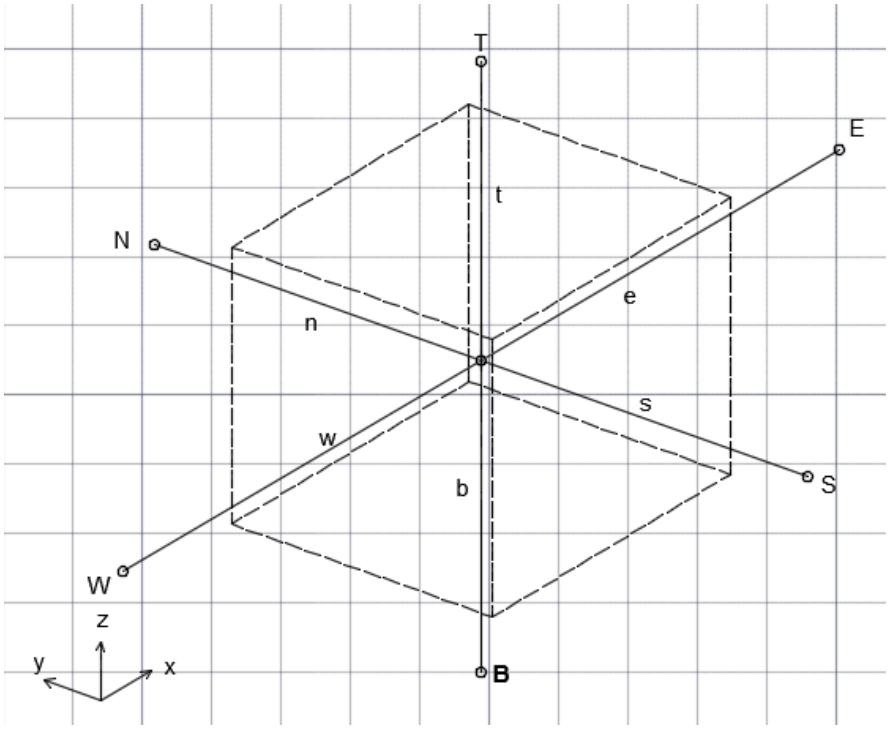

Figure: A cell in three dimensions and neighbouring nodes

The discretized equation in three dimensions for interior nodes have the form:

$$a_P \emptyset_P = a_W \emptyset_W + a_F \emptyset_F + a_S \emptyset_S + a_N \emptyset_N + a_B \emptyset_B + a_T \emptyset_T + S_u \quad \text{(A.11)}$$

where:

a_W	a_E	a_S	a_N	a_B	a_T	a_P
$\frac{G_w \cdot A_w}{\delta x_{WP}}$	$\frac{G_e \cdot A_e}{\delta x_{PE}}$	$\frac{G_s \cdot A_s}{\delta y_{SP}}$	$\frac{G_n \cdot A_n}{\delta y_{PN}}$	$\frac{G_b \cdot A_b}{\delta z_{BP}}$	$\frac{G_t \cdot A_t}{\delta z_{PT}}$	$a_W + a_E + a_S + a_N + a_B + a_T - S_P$

Boundary conditions can be introduced by cutting links with the appropriate faces(s) and modifying the source term.

Diffusion always occur alongside convection in nature so it is necessary to predict combined convection and diffusion. The steady convection-diffusion equation is the transport equation for a general property ∅ :

$$\mathrm{div}(\emptyset \mathrm{u}) = \mathrm{div}\left(\frac{G}{\rho}\ \mathrm{grad}\ \emptyset\right) + S_{\emptyset} = 0 \qquad \text{(A.1)}$$

This equation represent the flux balance in a control volume. The main problem in the discretization of the convective term is the determination of the value of transport property ∅ at control volume faces and its convective flux across these boundaries.

The integrated convection-diffusion equation for steady state are derived the same way as steady diffusion equation. One dimensional integrated convection-diffusion equation can be written as:

$$F_e \emptyset_e - F_w \emptyset_w = D_e (\emptyset_E - \emptyset_P) - D_w (\emptyset_P - \emptyset_W) \qquad \text{(A.12)}$$

And the continuity equation as:

$$F_e - F_w = 0 \qquad \text{(A.13)}$$

Where F and D are two variables which represent the convective mass flux per unit area and diffusion conductance at cell faces: $F = \rho u$ and $D = G/\partial x$. It is also assumed that the velocity field is “somehow known”, which takes care of the values of Fe and Fw. In order to solve equation (A.12) the transport property ∅ need to be calculated at the e and w faces.

Recommendations

One of the essential part of this research is the influence of the model simplification on the numerical results. It would be interesting to further investigate these simplifications on other intake structures examples as well.

Another finding of the numerical model tests is that intake 4, the shortest intake with the greatest opening curves shows least head losses. Another possible research topics includes optimisation of this intake geometry, possibly combining it with intake 1.

If any further numerical simulations are to be done using geometries obtained in this thesis, it would be of interest to dedicate more attention to the grid generation. The objective of this thesis was to compare numerical and physical results, therefore detail mesh generation, which is a huge topic itself, was not part of the research.